NUMERICAL STUDY OF PRESSURE-DRIVEN NITROGEN FLOW IN LONG MICROCHANNELS FOR APPLICATION TO ELECTRONIC COOLING

by

ZHANYU SUN

A Dissertation submitted to the

Graduate School—New Brunswick

Rutgers, The State University of New Jersey

in partial fulfillment of the requirements

for the degree of

Doctor of Philosophy

Graduate Program in Mechanical and Aerospace Engineering

Written under the direction of

Prof. Yogesh Jaluria

and approved by

Y Jaluria

Yuyun Lju

Jerry Shan

New Brunswick, New Jersey

January, 2009

ABSTRACT OF THE DISSERTATION

Numerical Study of Pressure-Driven Nitrogen Flow in Long Microchannels for Application to Electronic Cooling

by Zhanyu Sun

Dissertation Director: Prof. Yogesh Jaluria

Two-dimensional models have been developed to investigate pressure-driven laminar nitrogen slip flow in long rectangular microchannels with characteristic lengths ranging from 1.2μm to 50μm and length-to-height ratios up to 2500. The large length-to-height ratio is taken to measure pressure work and viscous dissipation. Rarefaction is incorporated by modifying the boundary conditions at fluid-solid interfaces. To resolve the intense numerical effort required by the large computational domain and the quasi-steady nature of the problem, a parallel SIMPLER-based solver is developed. The influences of variable properties, rarefaction and source terms in energy equation are investigated particularly for the cases with uniform wall heat flux boundary condition and are found to be far from negligible. The thermal and hydraulic characteristics under isothermal and uniform heat flux wall boundary conditions are extensively examined and discussed for pure convection cases. It is shown that the energy taken up by pressure work is dominant over the energy generation by viscous dissipation. Rarefaction is found to influence Nusselt number in two ways: rarefaction reduces Nusselt number through the heat transfer between the wall and bulk fluid, while promotes Nusselt number by affecting the source terms in energy equation. For microchannels of larger dimensions, it is found that rarefaction effects are still significant. The conjugate heat transfer associated with microchannel slip flows is also studied. It is found that axial conduction gives a great impact on the thermal field for substrates with finite thickness. Finally, unsteady convection is studied for a larger-dimension microchannel, where the characteristic response time is found to be greatly influenced by the energy taken up by pressure work.

Acknowledgements

My first appreciation must be sent to my advisor, Prof. Yogesh Jaluria, for his seasoned guidance and help in both my study and my life. I really have benefited a lot from his rich experience on numerical simulation. Many times, when I got lost within my research, it was him who pulled me out from the maze. He also cared my life a lot and offered as much help as he can. Prof. Jaluria is not only intelligently strong but also emotionally. It is worthwhile for me to spend my whole life in learning from him. In a word, Prof Jaluria is absolutely the best supervisor I have ever had. I would also like to thank other members of my graduate committee, Prof. Hao Lin, Prof. Tugrul Özel, and Prof. Jerry Shan for their valuable advice and careful evaluation of my dissertation.

I should send many thanks to the Mechanical and Aerospace Engineering Department for the four-year Teaching Assistantship, which essentially has supported both my study and my family. I am of a lot of gratitude to the Mphase(2) cluster of Rutgers University, and the technical support from the administrator, Dr. Alexei Kotelnikov.

I must thank all the professors that have taught me or gave me advices on my research. In particular, I am very grateful to Prof. Norman Zabusky. It is Prof. Zabusky who brought me from Singapore to Rutgers. I worked with him for more than a year till he retired. During the days with Prof. Zabusky, I learned a lot on the computational fluid dynamics. I had several valuable talks with Prof. Doyle Knight on parallel computing, which was proved to be crucial to build my codes.

Finally, I have to mention the peer students in the Mechanical and Aerospace Engineering department. In particular, I should thank Gaozhu Peng, Fusheng Xu as well as Chen Lin and Jing Yang couple, who helped me a lot during my first two years at Rutgers. I also cannot forget the valuable technical discussions with Doddi Sai.

Thank you all! Thank you!

Dedication

This dedication is dedicated to my parents and myself.

Table of Contents

Abstract ii

Acknowledgements iv

Dedication v

List of Tables x

List of Figures xi

List of Abbreviations xxii

1. Introduction 1

1.1. Background 1

1.2. Microscale Fluid Flows 2

1.2.1. Gas Flows 3

1.2.2. Liquid Flows 3

1.3. Gaseous Forced Convective Cooling in a Horizontal Microchannel 5

1.4. Objectives 7

2. Modeling Aspects of Two Dimensional Steady-State Pressure-Driven Nitrogen Flow in Long Microchannels 9

2.1. Introduction 9

2.2. Mathematical Model 11

2.3. Numerical Modeling Issues 14

2.3.1. Serial Numerical Procedure 14

2.3.2. Parallel Scheme 14

2.3.3. Implemental Issues 17

2.3.4. Code Validation 18

2.4. Physical Modeling Issues 23

2.4.1. Variable Properties 23

2.4.2. Source Terms in Energy Equation 25

2.4.3. Is the Traditional Continuum Model Good Enough for Microchannel Gaseous Slip Flows? 31

2.5. Summary 32

3. Two Dimensional Steady-State Pressure-Driven Nitrogen Flow in Long Microchannels Under Isothermal Wall Boundary Condition 36

3.1. Introduction 36

3.2. Numerical Model Description 37

3.3. Results and Comments 38

3.3.1. Wall Temperature 39

3.3.2. Inlet/Outlet Pressure Ratio 48

3.3.3. Comments 48

3.4. Conclusions 55

4. Two Dimensional Steady-State Pressure-Driven Nitrogen Flow in Long Microchannels Under Uniform Heat Flux Wall Boundary Condition . 63

4.1. Introduction 63

4.2. Numerical Model Description 65

4.3. Results and Comments 66

4.3.1. Wall Heat Flux 66

4.3.2. Rarefaction Effects 76

4.3.3. Inlet/Outlet Pressure Ratio 80

4.3.4. Comments 82

4.4. Conclusions 84

5. Two Dimensional Steady-State Pressure-Driven Nitrogen Flow in Larger-Dimension Microchannels Under Uniform Heat Flux Wall Boundary Condition 86

5.1. Introduction 86

5.2. Numerical Model Description 88

5.3. Channel #3 with Characteristic Dimension of 20 μm 88

5.3.1. Wall Heat Flux 89

5.3.2. Rarefaction Effects 94

5.3.3. Inlet/Outlet Pressure Ratio 97

5.4. Channel #4 with the Characteristic Dimension of 50 μm 99

5.4.1. Wall Heat Flux 99

5.4.2. Rarefaction Effects 107

5.4.3. Inlet/Outlet Pressure Ratio 113

5.5. Conclusions 113

6. Two Dimensional Steady-State Conjugate Heat Transfer for Pressure-Driven Nitrogen Flow in Long Microchannels Under Uniform Heat Flux Wall Boundary Condition 116

6.1. Introduction 116

6.2. Model Description and Numerical Procedure 118

6.3. Results and Discussion 119

6.3.1. Thermal Characteristics 120

6.3.2. The Substrate Thickness 123

6.3.3. Variable Properties of Substrate Materials 126

6.4. Conclusions 131

7. Two Dimensional Unsteady Convection for Pressure-Driven Nitrogen Flow in Long Microchannels Under Uniform Heat Flux Wall Boundary Condition 133

7.1. Introduction 133

7.2. Numerical Model Description 133

7.3. Results and Discussion 134

7.3.1. Wall Heat Flux Jump 134

7.3.2. Inlet Pressure Jump 143

7.3.3. Comments on Thermal Response Time 144

7.4. Conclusions 152

8. Conclusions and Future Work 153

8.1. Conclusions 153

8.2. Future Work 154

Vita 160

List of Tables

1.1. Classification of gas flows with Knudsen number. 4

2.1. Parameters of microchannel nitrogen flows. 22

2.2. Grid dependence test results for Channel #2. (a)Centerline temperature; (b)Centerline streamwise velocity. 25

5.1. Parameters of larger-dimension microchannel nitrogen flows. 87

6.1. Substrate material properties at 300K and the variable property models. 117

6.2. Grid dependence test results for a case using fused silica as substrate material and with $H_s/H = 1.0$, $P_{in}/P_{out} = 2.0$ and $\bar{q}_w = 2 \times 10^{-4}$. (a)Centerline temperature; (b)Centerline streamwise velocity. 120

7.1. Characteristic thermal response time for the point at $x/H = 30$ on microchannel centerline. 152

List of Figures

1.1. A typical schematic of a microchannel array mounted upon a CPU. . . . 2

2.1. The 2D schematic of a rectangular microchannel and the coordinates. . 12

2.2. Schematic of the joint of the two adjacent subdomains, where the shadow areas are the HALO (overlapping) regions, the arrows between the two subdomains denotes intersubdomain communication, the circles and arrows within the subdomains represent the main node and the velocities, respectively. 15

2.3. The schematic of the Level 1 communication of the parallel scheme. . . 16

2.4. The schematic of the two stages of the Level 2 communication of the parallel scheme. 16

2.5. Reproduction of part of Fig. 4.10 of Wang's [1] Ph.D dissertation. . . . 19

2.6. Pressure distribution of the current numerical study versus those of Pong et al.'s experimental investigation and Chen et al.'s [2] numerical investigation. PR denotes the pressure ratio $PR = P_{in}/P_{out}$. 20

2.7. The centerline u-velocity of the current numerical study versus that of Chen et al.'s [2] numerical investigation. 21

2.8. The u-velocity of the current numerical study versus that of Chen et al.'s [2] numerical investigation at three streamwise locations. 21

2.9. The v-velocity of the current numerical study versus that of Chen et al.'s [2] numerical investigation at three streamwise locations. 23

2.10. Comparison of variable property model with constant property model for a case with H2 type wall boundary condition $\bar{q}_w = 5 \times 10^{-5}$. (a) Nusslet number; (b) Bulk temperature; (c) Wall shear stress; (d) Volume flow rate. The solid lines denote the results from variable property model, while the dash lines denote those from constant property model. 26

2.11. Comparison of variable property model with constant property model for a case with H2 type wall boundary condition $\bar{q}_w = 2 \times 10^{-4}$. (a) Nusslet number; (b) Bulk temperature; (c) Wall shear stress; (d) Volume flow rate. The solid lines denote the results from variable property model, while the dash lines denote those from constant property model. 27

2.12. Comparison of bulk temperature profiles for four cases with the same H2 type wall boundary condition $\bar{q}_w = 5 \times 10^{-5}$, but modeled in four different ways: PW & VD - including both pressure work (PW) and viscous dissipation (VD); VD only - including VD only; PW only - including PW only; None - including neither. 29

2.13. Comparison of bulk temperature profiles for four cases with the same H2 type wall boundary condition $\bar{q}_w = 2 \times 10^{-4}$, but modeled in four different ways: PW & VD - including both pressure work (PW) and viscous dissipation (VD); VD only - including VD only; PW only - including PW only; None - including neither. 30

2.14. Comparison of the two cases with the same H2 type wall boundary condition $\bar{q}_w = 5 \times 10^{-5}$, but using two different models: Model A (solid lines) incorporates variable properties, rarefaction and the source terms in energy equation; Model B (dashed lines) uses constant properties at inlet temperature, and excludes rarefaction as well as the source terms in energy equation. (a) Nusslet number; (b) Bulk temperature; (c) Wall shear stress; (d) Volume flow rate. 33

2.15. Comparison of the two cases with the same H2 type wall boundary condition $\bar{q}_w = 2 \times 10^{-4}$, but using two different models: Model A (solid lines) incorporates variable properties, rarefaction and the source terms in energy equation; Model B (dashed lines) uses constant properties at inlet temperature, and excludes rarefaction as well as the source terms in energy equation. (a) Nusslet number; (b) Bulk temperature; (c) Wall shear stress; (d) Volume flow rate. 34

3.1. Centerline temperature profile in thermal entrance region for the cases with different T_w/T_0's at 1.2, 1.4, 1.6, and 1.8, respectively. 39

3.2. Local Nusselt number in thermal entrance region for the cases with different wall temperatures and $Kn > 0$. 41

3.3. Local Nusselt number in thermal entrance region for the cases with different wall temperatures and $Kn = 0$. 42

3.4. Knudsen number for the cases with different wall temperatures. 43

3.5. Local Nusselt number in thermally developed region for the cases with different wall temperatures. 44

3.6. Local pressure work over viscous dissipation ratio for the cases with different wall temperatures. 45

3.7. Centerline pressure distribution for the cases with different wall temperatures. 46

3.8. Comparison of velocity profiles at three different streamwise locations between the cases with T_w/T_0 at 1.2 and 1.4, respectively. (a) U-velocity; (b) V-velocity. 49

3.9. Wall shear stress for the cases with different wall temperatures. (a) Wall shear stress; (b) U-velocity gradient in y-direction. 50

3.10. Slip velocity for the cases with different wall temperatures. 51

3.11. Centerline flow conditions for the cases with different wall temperatures. (a) U-velocity; (b) Reynolds number. 52

3.12. Flow rates for the cases with different wall temperatures. (a) Volume flow rate; (b) Mass flow rate. 53

3.13. Local Nusselt number in thermal entrance region for the cases with different inlet/outlet pressure ratios. 54

3.14. Knudsen number for the cases with different inlet/outlet pressure ratios. 55

3.15. Local Nusselt number in thermally developed region for the cases with different inlet/outlet pressure ratios. 56

3.16. Local pressure work over viscous dissipation ratio for the cases with different inlet/outlet pressure ratios. 57

3.17. Centerline pressure distribution for the cases with different inlet/outlet pressure ratios. 58

3.18. Wall shear stress for the cases with different inlet/outlet pressure ratios. 59

3.19. Slip velocity for the cases with different inlet/outlet pressure ratios. . . 59

3.20. Centerline U-velocity for the cases with different inlet/outlet pressure ratios. 60

3.21. Flow rates for the cases with different inlet/outlet pressure ratios. (a) Volume flow rate; (b) Mass flow rate. 61

4.1. Velocity profile at the channel cross-sections of the case with $\bar{q}_w = 5 \times 10^{-5}$ and $PR = P_{out}/P_{in} = 2.0$. (a) U-velocity profile at three streamwise locations; (b) V-velocity profile at three streamwise locations. 67

4.2. Temperature profile at the channel cross-section $x/H = 400$ of the case with $\bar{q}_w = 5 \times 10^{-5}$ and $PR = P_{out}/P_{in} = 2.0$. 68

4.3. Centerline pressure distribution for the cases with $PR = P_{out}/P_{in} = 2.0$ and $\bar{q}_w$ ($q_{w,norm}$ in figure) ranging from 5×10^{-5} to 2.5×10^{-4}. 69

4.4. Bulk temperature distribution for the cases with $PR = P_{out}/P_{in} = 2.0$ and $\bar{q}_w$ ($q_{w,norm}$ in figure) ranging from 5×10^{-5} to 2.5×10^{-4}. 70

4.5. Centerline flow condition for the cases with $PR = P_{out}/P_{in} = 2.0$ and $\bar{q}_w$ ($q_{w,norm}$ in figure) ranging from 5×10^{-5} to 2.5×10^{-4}. (a) U-velocity; (b) Reynolds number. 71

4.6. Knudsen number and slip velocity for the cases with $PR = P_{out}/P_{in} = 2.0$ and $\bar{q}_w$ ($q_{w,norm}$ in figure) ranging from 5×10^{-5} to 2.5×10^{-4}. (a) Knudsen number; (b) Slip velocity. 73

4.7. Wall shear stress for the cases with $PR = P_{out}/P_{in} = 2.0$ and $\bar{q}_w$ ($q_{w,norm}$ in figure) ranging from 5×10^{-5} to 2.5×10^{-4}. (a) Wall shear stress; (b) Velocity gradient at the wall. 74

4.8. Local pressure work over viscous dissipation ratio for the cases with $PR = P_{out}/P_{in} = 2.0$ and $\bar{q}_w$ ($q_{w,norm}$ in figure) ranging from 5×10^{-5} to 2.5×10^{-4}. 75

4.9. The influence of rarefaction on flow rates for the cases with $PR = P_{out}/P_{in} = 2.0$ and $\bar{q}_w$ ($q_{w,norm}$ in figure) ranging from 5×10^{-5} to 2.5×10^{-4}. (a) Volume flow rate; (b) Mass flow rate. 77

4.10. The influence of rarefaction on local Nusselt number for the cases with $PR = P_{out}/P_{in} = 2.0$ and $\bar{q}_w$ ($q_{w,norm}$ in figure) ranging from 5×10^{-5} to 2.5×10^{-4}. 78

4.11. The influence of inlet/outlet pressure ratio on the bulk temperature. . . 81

4.12. The influence of inlet/outlet pressure ratio on the ratio of pressure work over viscous dissipation. 82

4.13. The influence of inlet/outlet pressure ratio on (a) Nusselt number; (b) The difference between wall and bulk temperature; 83

4.14. The influence of inlet/outlet pressure ratio on mass flow rate. 84

5.1. Velocity profile at the channel cross-sections of the case with $\bar{q}_w = 1 \times 10^{-3}$ and $PR = P_{out}/P_{in} = 1.03$. (a) U-velocity profile at three streamwise locations; (b) V-velocity profile at three streamwise locations. 90

5.2. Temperature profile at the channel cross-section $x/H = 50$ of the case with $\bar{q}_w = 1 \times 10^{-3}$ and $PR = P_{out}/P_{in} = 1.03$. 91

5.3. Centerline pressure distribution for the cases with $PR = P_{out}/P_{in} = 1.03$ and $\bar{q}_w$ ($q_{w,norm}$ in figure) ranging from 1×10^{-3} to 3×10^{-3}. 91

5.4. Bulk temperature distribution for the cases with $PR = P_{out}/P_{in} = 1.03$ and $\bar{q}_w$ ($q_{w,norm}$ in figure) ranging from 1×10^{-3} to 3×10^{-3}. 92

5.5. Centerline flow conditions for the cases with $PR = P_{out}/P_{in} = 1.03$ and $\bar{q}_w$ ($q_{w,norm}$ in figure) ranging from 1×10^{-3} to 3×10^{-3}. (a) U-velocity; (b) Reynolds number. 93

5.6. Knudsen number and slip velocity for the cases with $PR = P_{out}/P_{in} = 1.03$ and $\bar{q}_w$ ($q_{w,norm}$ in figure) ranging from 1×10^{-3} to 3×10^{-3}. (a) Knudsen number; (b) Slip velocity. 95

5.7. Wall shear stress for the cases with $PR = P_{out}/P_{in} = 1.03$ and $\bar{q}_w$ ($q_{w,norm}$ in figure) ranging from 1×10^{-3} to 3×10^{-3}. (a) Wall shear stress; (b) Velocity gradient at wall. 96

5.8. Local pressure work over viscous dissipation ratio for the cases with $PR = P_{out}/P_{in} = 1.03$ and $\bar{q}_w$ ($q_{w,norm}$ in figure) ranging from 1×10^{-3} to 3×10^{-3}. 97

5.9. The influence of rarefaction on flow rates for the cases with $PR = P_{out}/P_{in} = 1.03$ and $\bar{q}_w$ ($q_{w,norm}$ in figure) ranging from 1×10^{-3} to 3×10^{-3}. (a) Volume flow rate; (b) Mass flow rate. 98

5.10. The influence of rarefaction on local Nusselt number for the cases with $PR = P_{out}/P_{in} = 1.03$ and $\bar{q}_w$ ($q_{w,norm}$ in figure) ranging from 1×10^{-3} to 3×10^{-3}. 99

5.11. The influence of inlet/outlet pressure ratio on bulk temperature. 100

5.12. The influence of inlet/outlet pressure ratio on the ratio of pressure work over viscous dissipation. 100

5.13. The influence of inlet/outlet pressure ratio on Nusselt number. 101

5.14. The influence of inlet/outlet pressure ratio on mass flow rate. 101

5.15. Velocity profile at the channel cross-sections of the case with $\bar{q}_w = 3 \times 10^{-3}$ and $PR = P_{out}/P_{in} = 1.001$. (a) U-velocity profile at three streamwise locations; (b) V-velocity profile at three streamwise locations. 103

5.16. Temperature profile at the channel cross-section $x/H = 20$ of the case with $\bar{q}_w = 3 \times 10^{-3}$ and $PR = P_{out}/P_{in} = 1.001$. 104

5.17. Centerline pressure distribution for the cases with $PR = P_{out}/P_{in} = 1.001$ and $\bar{q}_w$ ($q_{w,norm}$ in figure) ranging from 3×10^{-3} to 9×10^{-3}. . . . 104

5.18. Bulk temperature distribution for the cases with $PR = P_{out}/P_{in} = 1.001$ and $\bar{q}_w$ ($q_{w,norm}$ in figure) ranging from 3×10^{-3} to 9×10^{-3}. 105

5.19. Centerline flow conditions for the cases with $PR = P_{out}/P_{in} = 1.001$ and $\bar{q}_w$ ($q_{w,norm}$ in figure) ranging from 3×10^{-3} to 9×10^{-3}. (a) U-velocity; (b) Reynolds number. 106

5.20. Knudsen number and slip velocity for the cases with $PR = P_{out}/P_{in} = 1.001$ and $\bar{q}_w$ ($q_{w,norm}$ in figure) ranging from 3×10^{-3} to 9×10^{-3}. (a) Knudsen number; (b) Slip velocity. 108

5.21. Wall shear stress for the cases with $PR = P_{out}/P_{in} = 1.001$ and $\bar{q}_w$ ($q_{w,norm}$ in figure) ranging from 3×10^{-3} to 9×10^{-3}. (a) Wall shear stress; (b) Velocity gradient at wall. 109

5.22. Local pressure work over viscous dissipation ratio for the cases with $PR = P_{out}/P_{in} = 1.001$ and $\bar{q}_w$ ($q_{w,norm}$ in figure) ranging from 3×10^{-3} to 9×10^{-3}. 110

5.23. The influence of rarefaction on flow rates for the cases with $PR = P_{out}/P_{in} = 1.001$ and $\bar{q}_w$ ($q_{w,norm}$ in figure) ranging from 3×10^{-3} to 9×10^{-3}. (a) Volume flow rate; (b) Mass flow rate. 111

5.24. The influence of rarefaction on local Nusselt number for the cases with $PR = P_{out}/P_{in} = 1.001$ and $\bar{q}_w$ ($q_{w,norm}$ in figure) ranging from 3×10^{-3} to 9×10^{-3}. 112

5.25. The influence of inlet/outlet pressure ratio on bulk temperature. 113

5.26. The influence of inlet/outlet pressure ratio on the ratio of pressure work over viscous dissipation. 114

5.27. The influence of inlet/outlet pressure ratio on Nusselt number. 114

5.28. The influence of inlet/outlet pressure ratio on mass flow rate. 115

6.1. The schematic of the 2D computational domain for the current conjugate heat transfer problem, where the shaded areas are channel walls and the blank area is the channel. 119

6.2. Temperature profile at the channel cross-section $x/H = 250$ of the case using fused silica as substrate material with $\bar{q}_w = 1 \times 10^{-4}$, $H_s/H = 1.0$ and $PR = P_{out}/P_{in} = 2.0$. 121

6.3. Bulk temperature profiles for the cases with $\bar{q}_w = 2 \times 10^{-4}$, $H_s/H = 1.0$ and $PR = P_{out}/P_{in} = 2.0$. 122

6.4. The maximum temperatures for the cases with $P_{in}/P_{out} = 2.0$, $\bar{q}_w$ ranging from 1×10^{-4} to 3×10^{-4} and $H_s/H = 1.0$. 122

6.5. Local Nusselt number for the cases with $\bar{q}_w = 2 \times 10^{-4}$, $H_s/H = 1.0$ and $PR = P_{out}/P_{in} = 2.0$. 123

6.6. Local Nusselt number for the cases with $\bar{q}_w$ ranging from 1×10^{-4} to 3×10^{-4}, $H_s/H = 1.0$ and $PR = P_{out}/P_{in} = 2.0$. The substrate material is (a) Fused silica; (b) Pyroceram; (c) Silicon Nitride; (d) Commercial Bronze. 124

6.7. Bulk temperature profiles along the microchannel for the cases with P_{in}/P_{out} ranging from 1.5 to 2.5, $\bar{q}_w = 2 \times 10^{-4}$ and $H_s/H = 1.0$. The substrate material is (a) Fused silica; (b) Pyroceram; (c) Silicon Nitride; (d) Commercial Bronze. 125

6.8. The maximum temperatures for the cases with P_{in}/P_{out} ranging from 1.5 to 2.5, $\bar{q}_w = 2 \times 10^{-4}$ and $H_s/H = 1.0$. 126

6.9. Local Nusselt number along the microchannel for the cases with P_{in}/P_{out} ranging from 1.5 to 2.5, $\bar{q}_w = 2 \times 10^{-4}$ and $H_s/H = 1.0$. The substrate material is (a) Fused silica; (b) Pyroceram; (c) Silicon Nitride; (d) Commercial Bronze. 127

6.10. Bulk temperature profiles along the microchannel for the cases with $P_{in}/P_{out} = 2.0$ and $\bar{q}_w = 2 \times 10^{-4}$ but different H_s/H's. The substrate material is (a) Fused silica; (b) Pyroceram; (c) Silicon Nitride; (d) Commercial Bronze. 128

6.11. The maximum temperatures for the cases with $P_{in}/P_{out} = 2.0$ and $\bar{q}_w = 2 \times 10^{-4}$ but different H_s/H's. 129

6.12. Nusselt number profiles along the microchannel for the cases with $P_{in}/P_{out} = 2.0$ and $\bar{q}_w = 2 \times 10^{-4}$ but different H_s/H's. The substrate material is (a) Fused silica; (b) Pyroceram; (c) Silicon Nitride; (d) Commercial Bronze. 130

6.13. Comparison of the maximum temperatures between variable and constant property models for the cases with $\bar{q}_w$ ($q_{w,norm}$ in figure) ranging from 1×10^{-4} to 3×10^{-4}, $H_s/H = 1.0$ and $PR = P_{out}/P_{in} = 2.0$, where VP denotes variable property model and CP denotes constant property model. (a) Fused silica; (b) Pyroceram. 132

7.1. The evolution of bulk temperature profile with time for the unsteady convection due to step change in wall heat flux. (a) Wall heat flux step-changes from low to high; (b) Wall heat flux step-changes from high to low. 136

7.2. The evolution of centerline velocity profile with time for the unsteady convection due to step change in wall heat flux. (a) Wall heat flux step-changes from low to high; (b) Wall heat flux step-changes from high to low. 137

7.3. The evolution of centerline pressure profile with time for the unsteady convection due to step change in wall heat flux. (a) Wall heat flux step-changes from low to high; (b) Wall heat flux step-changes from high to low. 138

7.4. The evolution of local Nusselt number profile with time for the unsteady convection due to step change in wall heat flux. (a) Wall heat flux step-changes from low to high; (b) Wall heat flux step-changes from high to low. 139

7.5. The evolution of temperature at some points on channel centerline with time for the unsteady convection due to step change in wall heat flux. (a) Wall heat flux step-changes from low to high; (b) Wall heat flux step-changes from high to low. 140
7.6. The evolution of streamwise velocity at some points on channel centerline with time for the unsteady convection due to step change in wall heat flux. (a) Wall heat flux step-changes from low to high; (b) Wall heat flux step-changes from high to low. 141
7.7. The evolution of pressure at some points on channel centerline with time for the unsteady convection due to step change in wall heat flux. (a) Wall heat flux step-changes from low to high; (b) Wall heat flux step-changes from high to low. 142
7.8. The evolution of bulk temperature profile with time for the unsteady convection due to step change in inlet pressure. (a) Inlet pressure step-changes from low to high; (b) Inlet pressure step-changes from high to low. 145
7.9. The evolution of centerline velocity profile with time for the unsteady convection due to step change in inlet pressure. (a) Inlet pressure step-changes from low to high; (b) Inlet pressure step-changes from high to low. 146
7.10. The evolution of centerline pressure profile with time for the unsteady convection due to step change in inlet pressure. (a) Inlet pressure step-changes from low to high; (b) Inlet pressure step-changes from high to low. 147
7.11. The evolution of local Nusselt number profile with time for the unsteady convection due to step change in inlet pressure. (a) Inlet pressure step-changes from low to high; (b) Inlet pressure step-changes from high to low. 148

7.12. The evolution of temperature at some points on channel centerline with time for the unsteady convection due to step change in inlet pressure. (a) Inlet pressure step-changes from low to high; (b) Inlet pressure step-changes from high to low. 149

7.13. The evolution of streamwise velocity at some points on channel centerline with time for the unsteady convection due to step change in inlet pressure. (a) Inlet pressure step-changes from low to high; (b) Inlet pressure step-changes from high to low. 150

7.14. The evolution of pressure at some points on channel centerline with time for the unsteady convection due to step change in inlet pressure. (a) Inlet pressure step-changes from low to high; (b) Inlet pressure step-changes from high to low. 151

List of Abbreviations

a	sound speed in gas, $\sqrt{\gamma RT}$
c_p	specific heat
H	channel height
H_s	substrate thickness
k	thermal conductivity
Kn	Knudsen number, λ/H
L	channel length
n	the outward normal of the channel wall
Nu	Nusselt number, $\frac{q_w H}{k(T_w - T_{bulk})}$
P	pressure
Po	Poiseuille number
Pr	Prandtl number
PR	inlet/outlet pressure ratio, P_{in}/P_{out}
PW	pressure work
q	heat flux
$\bar{q}$	nondimensionalized heat flux, $\bar{q} = \frac{qH}{T_0 k_0}$
R	specific gas constant
Re	Reynolds number, $\frac{\rho u H}{\mu}$
t	time
T	temperature

u, v	velocity in x- and y-direction,respectively
VD	viscous dissipation
W	channel width
x, y	coordinates

Greek Letters

γ	specific heat ratio
λ	mean free path of gas molecules
μ	dynamic viscosity
ρ	density
σ_T	thermal accommodation coefficient at the wall
σ_v	tangential momentum accommodation coefficient at the wall
β	thermal expansion coefficient
τ	nondimensionalized time unit, $\tau = H/a_0$

Subscripts

0	inlet condition
c	characteristic
$center$	centerline of the channel
g	gas
in	inlet
$norm$	normalized
out	outlet
s	substrate

w	wall

Superscripts

n	the n^{th} time/iteration step

Chapter 1

Introduction

1.1 Background

The thermal management of electronic systems has been studied for many years. To ensure the integrated circuit (IC) to work under designed temperature range, some appropriate cooling solutions must be employed. Inefficient heat removal may result in the vibration of electronic components as well as the accompanying noise, and finally lead to the failure of electronic systems. The factors that could affect the failure rate of electronic systems include the peak temperature, the spatial and temporal temperature gradient, etc. There are three levels in the electronic packaging hierarchy: chip level, board level and cabinet level. For chip level, the conduction from the chips to the package surface is dominant and thus the interest lies on the reduction of thermal resistance in between. The board level primarily deals with the arrangement of chips, where convection is the main mode of heat removal. Finally, cabinet level is mainly on the arrangement of boards. A good summary of the available cooling methods can be found in Wang's PhD thesis [1].

In the past few decades, Moore's Law has been proved to be an accurate prediction of improvements in semiconductor processes. With each process generation, manufacturers are able to pack more transistors into the same area and produce chips of greater and greater complexity. Chip speeds have increased to giga-hertz clock rates and entire systems have been reduced to a few highly integrated chips. The cost of the increased speed and integration is a dramatic increase in total heat and in heat density generated by millions of transistors packed into a very small space. In most chips, much of the heat is produced in a very small section of the die, resulting in concentration of heat into very small hot spots. Cooling these hot spots and removing total heat from the

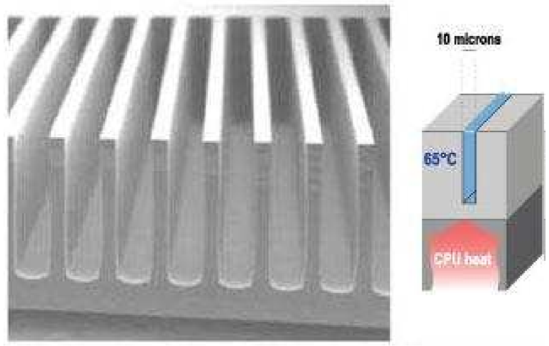

Figure 1.1: A typical schematic of a microchannel array mounted upon a CPU.

system present tremendous challenges to the system designer. Microchannels, which are fine channels etched into a silicon wafer and have approximately the width of a human hair, are built with a very high aspect ratio to increase their total surface area. As the fluid flows through the microchannels, their large surface area enables them to cool the hot spots with the heat flux as high as 1000 watts per square centimeter for liquid cooling, as shown by Tuckerman and Pease [3]. Fig. 1.1 shows a typical schematic of a microchannel array mounted upon a CPU.

1.2 Microscale Fluid Flows

As the rapid development of manufacturing technology, the creation of extremely small devices, such as the MEMS (microelectromechanical systems), becomes possible. Despite the thriving application of these small devices, the thermal and fluid phenomena involved have not been fully understood by the people working on the design and optimization. As the characteristic dimension shrinks, the fluid flows cannot always be accurately predicted by the Navier-Stokes equations with no-slip boundary condition at a fluid-solid interface. Many questions have been raised when experimental results found in microdevices could not be explained through traditional flow modeling. Due to the disparity in the intermolecular distance, the microscale gas and liquid flows behave in completely different manner and thus have to be studied separately.

1.2.1 Gas Flows

The continuum model leads to very accurate predictions, when the local properties such as density and velocity can be defined as averages over elements large enough compared to the molecular dimension of the fluid but small enough compared to the characteristic dimension of the phenomena. Another requirement for the validity of the continuum model is that the flow is not far from thermodynamic equilibrium. For gases, when the mean free path of gas molecules is much smaller than the characteristic flow dimension, the continuum model stands valid. As this condition is violated, the equilibrium conditions will no longer exist, and the linear relation between the stress and the rate of strain as well as the no-slip wall boundary condition will be invalid. Similar invalidity happens to the linear relation between the heat flux and the temperature gradient as well as the continuous temperature wall boundary condition. In his review paper, Gad-el-Hak [4] summarized the difference between the gas flows at different scales. Basically, the degree of the deviation of the gas flow from the continuum theory is identified by the Knudsen number, $Kn = \lambda/H$, where λ is the mean free path of gas molecules given by $\lambda = \mu\sqrt{\pi}/\sqrt{2\rho^2 RT}$ and H is the characteristic flow dimension. In the formula to calculate the mean free path, μ, ρ, R and T denote dynamic viscosity, density, specific gas constant and temperature, respectively. The classification of gas flows with Knudsen number is presented in Table 1.1. Specifically, for microscale slip flows, the continuum model is modified by the discontinuous tangential velocity and temperature boundary conditions at the gas-solid interface. The two modifications on the boundary conditions are based on the molecular kinetic theory for dilute gases and developed by Maxwell [5] and Smoluchowski [6], respectively.

1.2.2 Liquid Flows

Microscale fluid mechanics for liquid flows is more complicated in comparison with the gaseous cases. From the continuum point of view, liquids and gases are both fluids obeying the same momentum transport equations. When the characteristic dimension decreases, rarefaction effects become significant for gas flows. However, for microscale

Table 1.1: Classification of gas flows with Knudsen number.

Flow Type	Kn Range	Mathematical Model	Characteristic Dimension
Continum Flow	< 0.001	Navier-Stokes equation with continuous velocity and temperature distribution, i.e. no discontinuity exists at gas-solid interfaces.	$> 200\mu m$
Slip flow	$0.001 - 0.1$	Navier-Stokes equation with discontinuous velocity and temperature boundary conditions at gas-solid interfaces.	$0.5\mu m - 200\mu m$
Transition flow	$0.1 - 3$	Boltzmann equation; Statistical methods; Burnett equation with slip boundary conditions at gas-solid interfaces.	$0.01\mu m - 2\mu m$
Free Molecular flow	> 3	Direct-simulation Monte Carlo (DSMC); Particulate method of Boltzmann equation	$< 0.06\mu m$

liquid flows, the molecules are much more closely packed at normal pressures and temperatures, and the attractive or cohesive potential between liquid molecules as well as between liquid and solid ones plays a dominant role if the characteristic length of the flow is sufficiently small. Accordingly, liquids do not have a well advanced molecular-based theory. The concept of mean free path is of much less use for liquids and the conditions under which a liquid flow fails to be in quasi-equilibrium state are not well defined. Therefore, in the cases when the traditional continuum model fails to provide accurate predictions or postdictions, the expensive molecular dynamics simulation seems to be the only reliable tool available to rationally characterize the microscale liquid flows. Unfortunately, such simulations are not yet feasible for realistic flow extent or number of molecules. This is why the microfluid mechanics for liquids is much less developed than that for gases.

1.3 Gaseous Forced Convective Cooling in a Horizontal Microchannel

As mentioned above, microchannels are normally used together with heat sinks and fins, which could greatly reduce the energy dissipation rate per unit area and hence make gas cooling feasible. This dissertation will limit to gaseous slip flows and mainly study pressure-driven forced convection in a horizontal rectangular microchannel. Rectangular or trapezoidal microchannels are widely used in electronic packages and many MEMS devices. Other geometries, such as the circular and triangular microducts, are not very popular mainly because of their fabrication complexity. For cooling purpose, turbulent flows are obviously more preferable than laminar flows. However, almost all the microchannel gas flows found in practice are within laminar regime. This is primarily due to the demanding pumping power caused by the small duct dimension. Due to its low thermal conductivity, low density and low specific heat, compared to liquid cooling, gas cooling is generally thought to be less effective. As a result, when great heat removal is required, gas cooling may cause a number of problems. In spite of its disadvantages, laminar gas cooling, most commonly air cooling, is still widely employed in industry because of its easy availability, low cost, design simplicity, etc. This is why air cooling is so popular in our daily electronic systems, such as the desktop/laptop

PCs, TVs, game players and so on. In comparison with air cooling, nitrogen cooling owns the edge due to the absence of oxygen, which may lead to oxidization of the duct walls. In addition, air is composed of about 80% nitrogen and 20% other gases. Therefore, nitrogen is of great interest and will be studied in this dissertation. For most pressure-driven gas flows in a horizontal microchannel, the buoyancy is negligible. For example, for a microchannel of 1.5mm long and $3\mu m$ high, if the inlet and the outlet pressures are fixed at 2×10^5Pa and 1×10^5Pa, respectively, the ratio of axial pressure gradient over gravitational force, $\frac{dp/dx}{\rho g}$, will be in the order of $10^7 : 1$. Here dp/dx is the streamwise pressure gradient, ρ denotes fluid density, and g represents the gravitational acceleration. Another more commonly used indicator for the buoyancy force, the Grashof number, $Gr = \frac{g\beta\Delta T H^3}{\nu^2}$, will be at most in the order of 10^{-6}. Here β and ν denote the thermal expansion coefficient and kinematic viscosity, respectively; H and ΔT are the spacing and the temperature difference between the two plates.

For the pressure-driven gaseous convection in a microchannel, pressure drops down the duct to overcome friction at the gas-solid interfaces. Therefore, if the gas is heated or kept at constant temperature, gas density will decrease along the channel and thus the gas must be treated as compressible. The density drop and the conservation of mass require the flow to accelerate down the uniform duct. The gas acceleration in turn affects the pressure gradient, resulting in a nonlinear pressure profile along the channel. Accompanying the change of density, if the gas is heated or kept at constant temperature, the Knudsen number will increase along the microchannel. Hence, when the outlet pressure is very low or the gas is greatly heated, the flow close to the outlet may go beyond the slip flow regime and become transitional flow. One of the big differences between macro- and microchannels is the length-to-height ratio. For macrochannels, the length-to-height ratio is normally well below 100; for microchannels, this ratio could be as large as a few thousand. The large length-to-height ratio could make pressure work and viscous dissipation significant for microchannel flows. Another obvious difference between macro- and microchannel flows is the boundary conditions at the walls. As presented in Table 1.1, for slip flows, due to rarefaction, the continuum model is modified with the discontinuous wall boundary conditions, including the velocity slip, the thermal creep and the temperature jump. Because of these new mechanisms, a lot of deviations from the continuum theory are experimentally observed in microchannel gas flows [7, 8, 9, 10, 11]. In these experimental studies, the Poiseuille number (Po) and Nussult number (Nu) were measured to demonstrate the deviation of the fluid and thermal fields from the conventional continum theory, respectively. Many analytic studies [12, 13, 14, 15, 16, 17, 18, 19] can be found in the literature to explain these experimental findings. Analytic studies, however, are restricted by some strong assumptions, including the fully-developed flow field, negligible compressibility, constant property and so on. Numerical studies, on the other hand, do not have such limitations and thus are capable of reproducing experimental results. For example, Chen et al. [2] reproduced the experimental result of Pong et al [9] and found good agreement. Based on the author's literature review, the published numerical works are either purely on the fluid field or restricted to short microchannels with length-to-height ratios below 50. No comprehensive numerical studies have been reported on the forced convection in gaseous microchannel slip flows. Due to the small microchannel height and the fabrication requirement, the ratio of the substrate thickness over the microchannel height is no longer negligible as for most macrochannels. Therefore, conjugate heat transfer is of great interest. For conjugate cases, a number of issues need to be carefully examined, including the role of the axial conduction in the substrates, the influence of the substrate thickness over channel height ratio and the substrate material properties. Also the microscale unsteady flow is still the topic that has not been systematically studied and therefore will be investigated in this dissertation.

1.4 Objectives

This dissertation concentrates on the microchannel gaseous slip flows. As pointed out in section 1.3, comprehensive numerical investigations on the long microchannel gaseous pressure-driven convection have not been done. The impacts of rarefaction, variable properties and source terms in the energy equations (pressure work and viscous dissipation), have not been weighted yet. These physical modeling issues will be addressed in Chapter 2, where the numerical modeling issues are also studied. In Chapter 3 and

Chapter 4, the characteristics of the nitrogen flows in long microchannels with isothermal and constant heat flux wall boundary conditions are investigated, respectively. Chapter 5 focuses on the characteristics of the nitrogen flows in larger-dimension microchannels with constant heat flux wall boundary condition. Microscale conjugate heat transfer is investigated in Chapter 6. Finally, some unsteady convections are studied in Chapter 7.

Chapter 2

Modeling Aspects of Two Dimensional Steady-State Pressure-Driven Nitrogen Flow in Long Microchannels

2.1 Introduction

Since the early 1990s, several researchers have conducted studies on the thermal and hydraulic characteristics of microchannel gaseous slip flow. The discrepancy between micro- and macro-channel flows was reported by several groups of experimentalists [7, 8, 9, 10, 11]. In these studies, the Poiseuille number (Po) and Nussult number (Nu) were measured to describe the flow and convective heat transfer, respectively. Both Choi et al. [7] and Pfahler et al. [8] found a reduced Po for the fully developed laminar nitrogen flow in a microduct with a characteristic length less than $10\mu m$, compared to the theoretical continuum values. Choi et al. [7] also studied the heat transfer in the turbulent regime and found a higher Nu than that predicted by the continuum theory. Pong et al. [9] reported a nonlinear streamwise pressure distribution of nitrogen flow in a microchannel with the characteristic height of $1.2\mu m$. In addition to the similar findings shown in [7, 8, 9], Harley et al. [10] used the slip boundary condition to model their experiment. Yu et al. [11] extended the investigation by Choi et al. [7]. Except for the lower Po, they agreed with Choi et al. [7] on the higher Nu, compared to the value predicted by the traditional correlation.

Analytical solutions of the fully-developed slip-flow heat transfer in microtubes were given by Sparrow et al. [12] in as early as 1962. However, due to the ease of fabricating rectangular microchannels, a large number of analytical and numerical investigations on the slip-flow heat transfer within rectangular microchannels were presented in the recent years to explain the experimental deviation from the continuum theory. Arkilic et al. [13] studied the pressure-driven helium flow in a long microchannel both analytically and experimentally. It was found that, by taking the velocity slip and compressibility effects into account, the 2D Navier-Stokes equations could fairly accurately predict the mass-flow rate. Instead of using the velocity slip and temperature jump to model the laminar microscale fully-developed flow, Li et al. [14] proposed the 'wall-adjacent layer', where the change of gas thermal conductivity results in significant influence on the heat transfer and is able to make accurate qualitative predictions. The laminar, fully-developed, slip-flow forced convection in rectangular microchannels, with isothermal and isoflux wall boundary conditions, were investigated analytically by Yu and Ameel [15, 16]. The authors discussed the effects of velocity slip and temperature jump on Nu, and showed that, compared to the no-slip flow condition, the heat transfer could be either reduced or enhanced. Tunc and Bayazitoglu [17] conducted an analytical study on the convection heat transfer in a rectangular microchannel, where the flow is assumed to be fully-developed both thermally and hydrodynamically. In a recent paper, Chen carried out an analytical study on the developing temperature field in laminar forced convection in a microchannel with isothermal wall boundary condition, where viscous dissipation was considered in addition to rarefaction, while the flow field was still assumed to be full-developed as in the previous studies [14, 15, 16, 17]. Jeong and Jeong [19] extended chen's [18] work by including the axial conduction into their analysis.

The analytical studies really improved our understanding of the hydraulic and thermal phenomena in microchannel gas flows. However, the limitation of the analytical approach makes it impossible to reproduce some experiments, especially in the cases with the developing flow field, and thus makes it important to use the numerical methods. Beskok et al. [20] presented their numerical simulations, where rarefaction, compressibility, viscous dissipation as well as thermal creep effects were considered. They discussed the competing effects of compressibility and rarefaction on the nonlinear pressure distribution of the internal gas flow within long microchannels, which interpreted the findings of Pong et al. [9]. Guo and Wu [21] numerically studied the compressibility effect on the gas flow and heat transfer in a microtube, where rarefaction effects were not included. They concluded that fully-developed pressure-driven gas flow does not arise due to the compressibility. It was also shown by Guo and Wu [21] that, because of the large dependence of thermal field on fluid field, for microchannel gas flows with non-negligible Mach number, the fully-developed thermal field does not arise. To reproduce the experimental results by Pong et al. [9], Chen et al. [2] conducted 2D numerical simulations, where the rectangular microchannel flow was modeled as compressible with rarefaction and viscous dissipation. Good agreement was achieved. Similar to Chen et al. [2], Roy et al. [22] also reproduced the experiments by Pong et al. [9] using 2D simulations, and their results were in good agreement with those by Chen et al. [2]. In a recent publication, Raju and Roy [23] further extended their study to the supersonic microchannel flows and compared their results with the published direct-simulation Monte Carlo results.

This chapter concentrates on the modeling aspects of the microchannel gas flow. The organization is as follows: in section 2.2, the mathematical model is described; section 2.3 addresses on some relevant numerical modeling issues with code validation; in section 2.4, the physical modeling issues are investigated; finally, a brief summary is given in section 2.5.

2.2 Mathematical Model

For rectangular microchannels found in practice, the aspect ratio, W/H, is normally very high. In such cases, 2D model can very well predict the mass flow rate [24] and hence is used in this study. In accordance with the coordinate system shown in Fig. 2.1, the 2D governing equations for the compressible gas flows in a rectangular microchannel is given below.

Continuity:

$$\frac{\partial \rho}{\partial t} + \frac{\partial \rho u}{\partial x} + \frac{\partial \rho v}{\partial y} = 0 \tag{2.1}$$

Momentum:

$$\begin{aligned}\frac{\partial \rho u}{\partial t} + \frac{\partial \rho u u}{\partial x} + \frac{\partial \rho v u}{\partial y} &= \left[\frac{\partial}{\partial x}\left(\mu \frac{\partial u}{\partial x}\right) + \frac{\partial}{\partial y}\left(\mu \frac{\partial u}{\partial y}\right)\right] - \frac{\partial P}{\partial x} \\ &+ \left[\frac{\partial}{\partial x}\left(\mu \frac{\partial u}{\partial x}\right) + \frac{\partial}{\partial y}\left(\mu \frac{\partial v}{\partial x}\right)\right] - \frac{2}{3}\frac{\partial}{\partial x}\left[\mu\left(\frac{\partial u}{\partial x} + \frac{\partial v}{\partial y}\right)\right]\end{aligned} \tag{2.2}$$

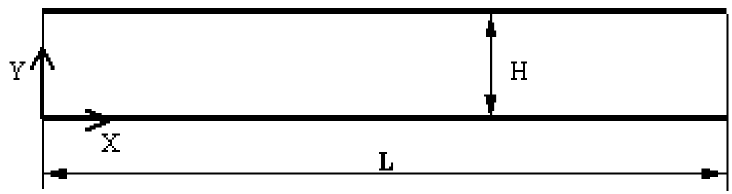

Figure 2.1: The 2D schematic of a rectangular microchannel and the coordinates.

$$\begin{aligned}\frac{\partial \rho v}{\partial t}+\frac{\partial \rho u v}{\partial x}+\frac{\partial \rho v v}{\partial y} &= \left[\frac{\partial}{\partial x}\left(\mu\frac{\partial v}{\partial x}\right)+\frac{\partial}{\partial y}\left(\mu\frac{\partial v}{\partial y}\right)\right]-\frac{\partial P}{\partial y}\\ &+\left[\frac{\partial}{\partial x}\left(\mu\frac{\partial u}{\partial y}\right)+\frac{\partial}{\partial y}\left(\mu\frac{\partial v}{\partial y}\right)\right]-\frac{2}{3}\frac{\partial}{\partial y}\left[\mu\left(\frac{\partial u}{\partial x}+\frac{\partial v}{\partial y}\right)\right]\end{aligned} \tag{2.3}$$

<u>Energy:</u>

$$\begin{aligned}c_p\left[\frac{\partial \rho T}{\partial t}+\frac{\partial \rho u T}{\partial x}+\frac{\partial \rho v T}{\partial y}\right] &= \left[\frac{\partial}{\partial x}\left(k\frac{\partial T}{\partial x}\right)+\frac{\partial}{\partial y}\left(k\frac{\partial T}{\partial y}\right)\right]+\beta T\left[\frac{\partial P}{\partial t}+u\frac{\partial P}{\partial x}+v\frac{\partial P}{\partial y}\right]\\ &+\mu\left\{2\left[\left(\frac{\partial u}{\partial x}\right)^2+\left(\frac{\partial v}{\partial y}\right)^2\right]+\left(\frac{\partial u}{\partial y}+\frac{\partial v}{\partial x}\right)^2-\frac{2}{3}\left(\frac{\partial u}{\partial x}+\frac{\partial v}{\partial y}\right)^2\right\}\end{aligned} \tag{2.4}$$

The working gas, specifically nitrogen in this dissertation, is treated as an ideal gas, for which the state equation is $P = \rho RT$ and the thermal expansion coefficient $\beta = 1/T$. In the variable-property model, the state equation is used to calculate density. Other transport properties of nitrogen are determined using the power law correlations given by Fotiadis et al. [25]. Therefore, the formulas for the variable properties are

$$\rho = \rho_0(T_0/T)(P/P_0) \tag{2.5}$$

$$k = k_0(T/T_0)^{0.77} \tag{2.6}$$

$$\mu = \mu_0(T/T_0)^{0.68} \tag{2.7}$$

$$c_p = c_{p,0}(T/T_0)^{0.078} \tag{2.8}$$

At the inlet, the pressure is fixed at P_{in} and the flow is assumed to be fully developed at constant temperature T_0. At the outlet, the pressure is fixed at $1\times10^5 Pa$. Therefore, the mathematical form of the boundary conditions at the inlet and outlet turns out to be:

At $x = 0$,

$$\frac{\partial u}{\partial x} = 0, v = 0, T = T_0, P = P_{in} \tag{2.9}$$

At $x = L$,

$$P = P_{out} = 1 \times 10^5 Pa \tag{2.10}$$

The outlet velocity and temperature are obtained by the extrapolation along the same y coordinate. The wall boundary conditions will vary with different cases. Due to rarefaction, discontinuous boundary conditions are applied at the wall. For the uniform wall heat flux cases, the wall boundary conditions are:

At $y = 0$ and $y = H$,

$$\begin{aligned} u = \frac{2-\sigma_v}{\sigma_v}\lambda\left(\frac{\partial u}{\partial n}\right)_w + \frac{3}{4}\frac{\mu}{\rho T}\left(\frac{\partial T}{\partial x}\right)_w, v = 0, \\ q = q_w \end{aligned} \tag{2.11}$$

while for the isothermal walls, the wall boundary conditions are:

At $y = 0$ and $y = H$,

$$\begin{aligned} u = \frac{2-\sigma_v}{\sigma_v}\lambda\left(\frac{\partial u}{\partial n}\right)_w + \frac{3}{4}\frac{\mu}{\rho T}\left(\frac{\partial T}{\partial x}\right)_w, v = 0, \\ T_g - T_w = \frac{2-\sigma_T}{\sigma_T}\left(\frac{2\gamma}{1+\gamma}\right)\frac{\lambda}{\mathrm{Pr}}\left(\frac{\partial T}{\partial n}\right)_w \end{aligned} \tag{2.12}$$

The coefficients σ_v and σ_T, which depend on the gas properties and surface qualities, represent the fractions of the gas molecule's tangential momentum and energy loss through the interactions with the solid wall, respectively. For example, it is straightforward that $\sigma_v = 0$ and $\sigma_v = 1$ correspond to the cases of the specular and diffuse reflections, respectively. For most engineering cases, the surfaces are so rough that the conditions are very close to diffuse reflection, i.e., $\sigma_v \approx 1$. Similar argument can be made on σ_T. Therefore, to simulate the engineering condition, the values of σ_v and σ_T are both set to unity.

2.3 Numerical Modeling Issues

2.3.1 Serial Numerical Procedure

The governing equations given in section 2.2 are strongly coupled. Therefore, the continuity, momentum and energy equations have to be solved simultaneously. The finite volume method (FVM), with an approach similar to the SIMPLER algorithm, is employed to solve the governing equations. The diffusion terms are discretized by the central difference scheme, and the forward difference discretization is applied to the time derivative terms. Using the method of Thakur and Shyy [26], the second order upwind scheme (SOU) for a uniform grid system is derived. All coefficients of the first order upwind scheme (FOU), given by Patankar [27], are still applicable in SOU, except that an additional term is combined into the source term. Since the SOU needs two neighbor nodes in the upwind direction, the FOU is used for the nodes adjacent to the boundaries. The alternating direction implicit (ADI) method is employed to solve the momentum and the energy equation. In each sweeping direction, the resulting linear algebraic system is solved using the Tridiagonal Matrix Algorithm (TDMA). The pressure equation and the pressure correction equation are solved using the Successive Over Relaxation method (SOR).

2.3.2 Parallel Scheme

Because of the intense computation required by the large computational domain and the quasi-steady thermal field associated with the gas flow in long micro-channels, the above serial codes must be paralleled. Similar to the parallel scheme described by Baltas and Spalding [28], the domain decomposition method (DDM) is employed. Compared to other alternatives, the DDM has several advantages. First, the DDM can greatly lower down the single-CPU computational time. Generally, the more CPUs, the shorter the single-CPU computational time is. Secondly, the original serial algorithm is still usable in each subdomain. Thirdly, the communications between the subdomains are not very frequent. For the long microchannels to be studied, the length-to-height ratio $L : H$ is in the order of $10^3 : 1$. Therefore, the computational domain is decomposed

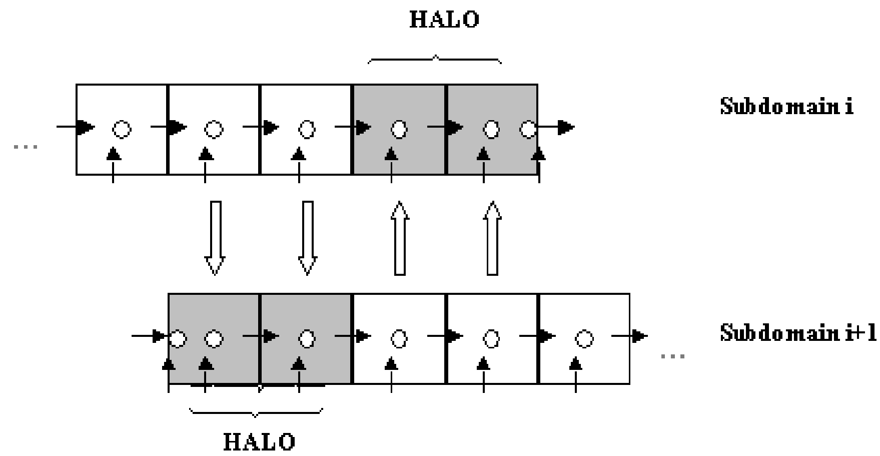

Figure 2.2: Schematic of the joint of the two adjacent subdomains, where the shadow areas are the HALO (overlapping) regions, the arrows between the two subdomains denotes intersubdomain communication, the circles and arrows within the subdomains represent the main node and the velocities, respectively.

in the streamwise direction only. The cells in the global domain are evenly distributed to the subdomains streamwisely. For the communications between the subdomains, at the internal ends of each subdomain, a number of HALO cells (overlapping cells) are attached. The minimum number of HALO cells required is problem dependent. In general, as verified by our numerical experiments, more HALO cells lead to better numerical stability and faster convergence. Fig. 2.2 is the schematic of the joint of two adjacent subdomains for 2D conditions with two HALO cells.

With the MPI (Message Passing Interface), the processes under use are named from ZERO to NP-1, where NP is the number of processes involved. Process ZERO acts as a server to distribute input to and collect output from the subdomains. The remaining NP-1 processes, process 1 to process NP-1, undertake the computations of subdomains #1 to NP-1, respectively. Fig. 2.3 shows the schematic of the architecture of the processes and the communication between process ZERO (P_0) and other processes (P_1 to P_{NP-1}). This kind of communication is named Level 1 communication (double arrows in Fig. 2.3). Level 1 communication occurs at the beginning and the end of the job and has constant message length. The Level 2 communication is that between adjacent subdomains as described in Fig. 2.4. After each time step, the HALO regions

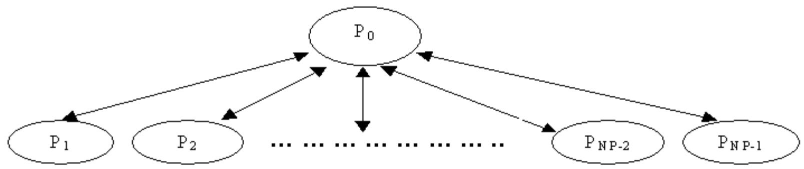

Figure 2.3: The schematic of the Level 1 communication of the parallel scheme.

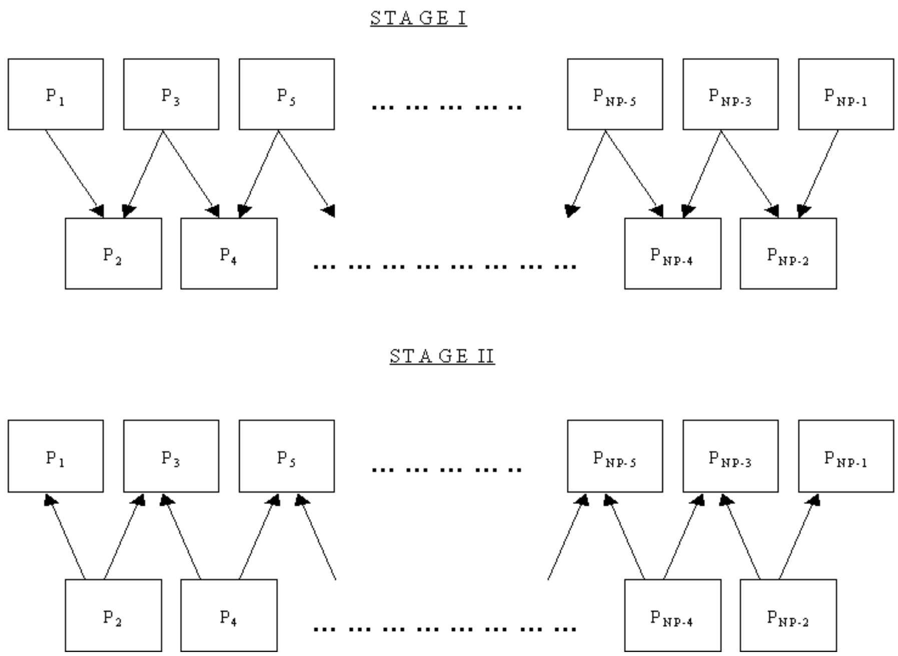

Figure 2.4: The schematic of the two stages of the Level 2 communication of the parallel scheme.

are updated by the adjacent subdomains' overlapping internal cells, as depicted in Fig. 2.2. There are two stages in the HALO region update process. At the first stage, all the odd-numbered processes first send fresh boundary data to their even-numbered neighbors, which only receive at this moment. Then at the second stage, the odd- and even-numbered processes switch their roles. This parallel communication scheme and the constant message length, guarantee that the time cost of each Level 2 communication is almost a constant and independent of the number of processes involved in the computation.

2.3.3 Implemental Issues

During the implementation of this parallel scheme, the only concern lies on the artificial break points required by the DDM. It is clear that the application of DDM will block the communication between the subdomains and thus reduce the convergence speed or even make the convergence impossible. This is why HALO regions are always used together with the DDM. In our parallel solver, the information is exchanged between the subdomains through the HALO regions after each time step. Numerically, it is not allowed to infinitely increase the number of the HALO cells because the communication between the subdomains is very expensive. From our preliminary study, we found that twelve HALO cells are generally good enough for convergence purpose. The use of more than twelve HALO cells has negligible impact on the convergence speed.

Apart from the convergence speed, the singularity that is introduced by the artificial cuts of the computational domain is another big problem. Based on our numerical experiments, the increase of the HALO region size cannot remove the singularity at the cuts at all. In addition, the boundary condition imposed on the cuts almost has no connection with the singularity. The only possible way to remove the singularity is to feed the outputs from the parallel solver to the serial solver. Therefore, the serial and the parallel solvers must be used together. In fact, the singularities at the cuts are very well confined within a very small region around the cuts. Without these localized singularities, the output from the parallel solver is essentially a very good initial condition towards the steady state solution. For example, our preliminary test case did show that if we feed the output obtained by running the parallel solver for thirty thousand time steps to the serial solver, the serial solver only takes no more than two hundred time steps to reach the desired convergence criteria. On the other hand, for the same case, to get the same convergence solely by the serial solver, it takes more than twenty thousand time steps.

To get the steady state solution, the time marching procedure is employed. For the parallel solver, the convergence criteria are of the form,

$$\varepsilon = \max \left\{ \begin{array}{ll} \text{if } \xi^n \neq 0 & \frac{|\xi^{n+1} - \xi^n|}{|\xi^n|} \\ \text{if } \xi^n = 0 & |\xi^{n+1}| \end{array} \right\} \tag{2.13}$$

where ξ applies to the variable u, T as well as the variables in the HALO regions and the superscripts denote the time step. For the serial solver, the convergence criteria only apply to u and T. In summary, the parallel solver must be used together with the serial solver to eliminate the singularity caused by the domain decomposition. That is, first the parallel solver is used and runs until some convergence criteria is reached, then the output from the parallel solver are input to the serial solver, which then runs until ε falls below a very small value. Due to the singularity mentioned above, the convergence criteria for the parallel run are usually much lower than those for the following serial run.

2.3.4 Code Validation

The serial version of the SIMPLER-based codes has been employed to study the macrochannel cooling problems by Wang [1]. The reproduction of part of Fig. 4.10 in Wang's thesis is shown in Fig. 2.5. To further validate the codes, which are paralleled now and include the microscale effects (the discontinuous wall boundary conditions, viscous dissipation, pressure work, etc.), the experimental results by Pong et al. [9] are reproduced. Besides the experimental results by Pong et al. [9], our numerical results are also benchmarked with the numerical results by Chen et al. [2]. The parameters of the microchannel, which was one of the two used in the experiment of Pong et al. [9], are listed in Table 2.1 under Channel #1. In these validating runs, the temperature of the isothermal wall is equal to the inlet temperature at 314K. After the grid dependence experiment, we got similar results as those by Chen et al. [2], i.e., a 6000×23 grid should be used for this simulation. The convergence criteria for the final serial run are set to be $\varepsilon < 1 \times 10^{-8}$ for u and T. Fig. 2.6 presents the comparison of the pressure distribution of the current numerical study with those of Pong et al.'s [9] experimental investigation and Chen et al.'s [2] numerical investigation. In Fig. 2.6, it is found that our results agreed with Chen et al.'s [2] results very well with the difference below 0.1%,

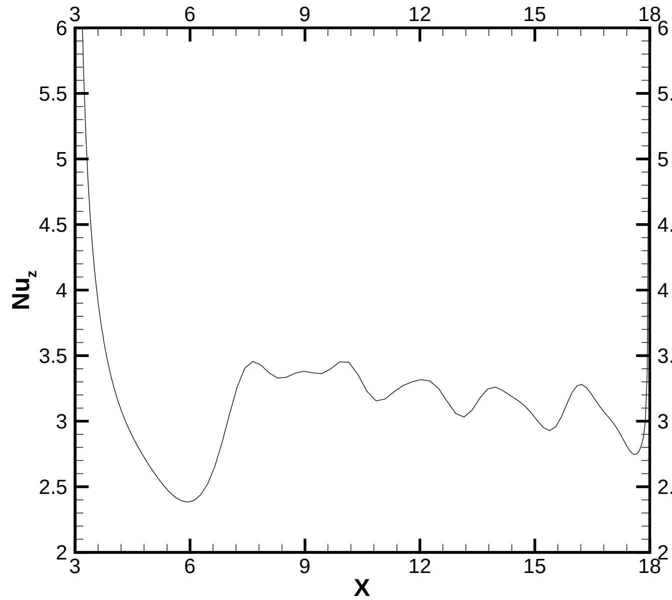

Figure 2.5: Reproduction of part of Fig. 4.10 of Wang's [1] Ph.D dissertation.

and the degree of agreement with the experimental data are comparable to that with Chen et al.'s [2] results. Fig. 2.7 shows the normalized centerline u-velocity of the current numerical study versus that of Chen et al.'s [2] numerical investigation. Again, the agreement is very good and the difference is within 0.1%. Fig. 2.8 and Fig. 2.9 present the normalized u- and v-velocity of the current numerical study versus that of Chen et al.'s [2] numerical investigation, respectively. The comparison is made at three streamwise locations (upstream, midstream and downstream). It is clear that u-velocity agrees very well at all three streamwise locations. However, v-velocity shows good agreement only at the downstream. This is probably because of the different convergence criteria employed by Chen et al. [2]. With an analysis of the continuity equation based on the magnitudes shown in Fig. 2.8 and Fig. 2.9, we can find that the fluctuation of u-velocity within merely 0.001% will cause a fluctuation of v-velocity up to the order of 10% or more. Therefore, v-velocity is very sensitive to the change of u-velocity and may change a lot even under a very minor difference between different numerical procedures.

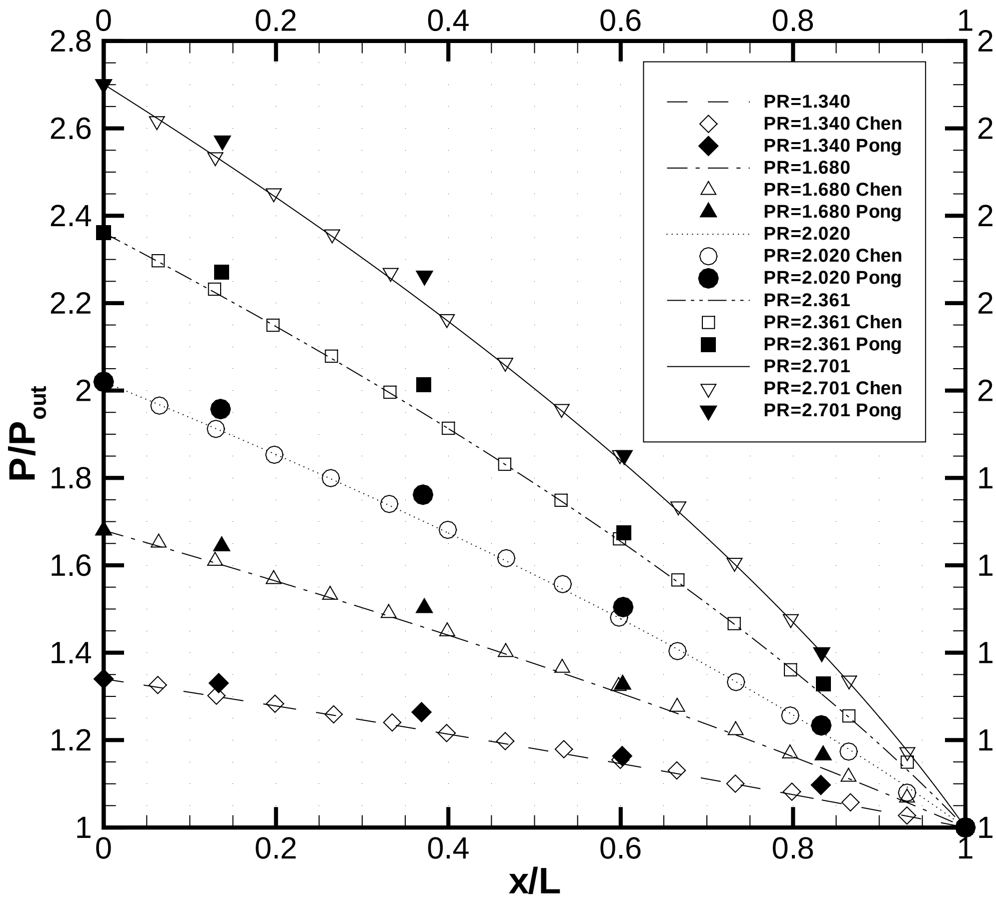

Figure 2.6: Pressure distribution of the current numerical study versus those of Pong et al.'s experimental investigation and Chen et al.'s [2] numerical investigation. PR denotes the pressure ratio $PR = P_{in}/P_{out}$.

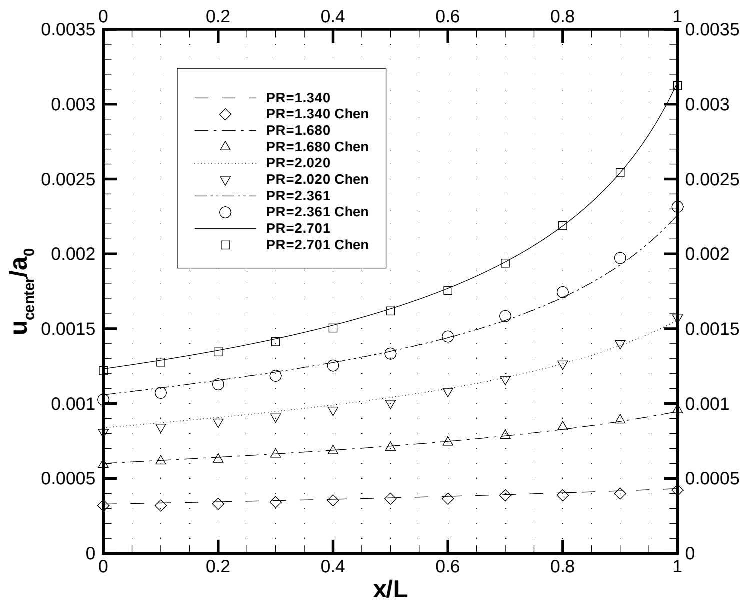

Figure 2.7: The centerline u-velocity of the current numerical study versus that of Chen et al.'s [2] numerical investigation.

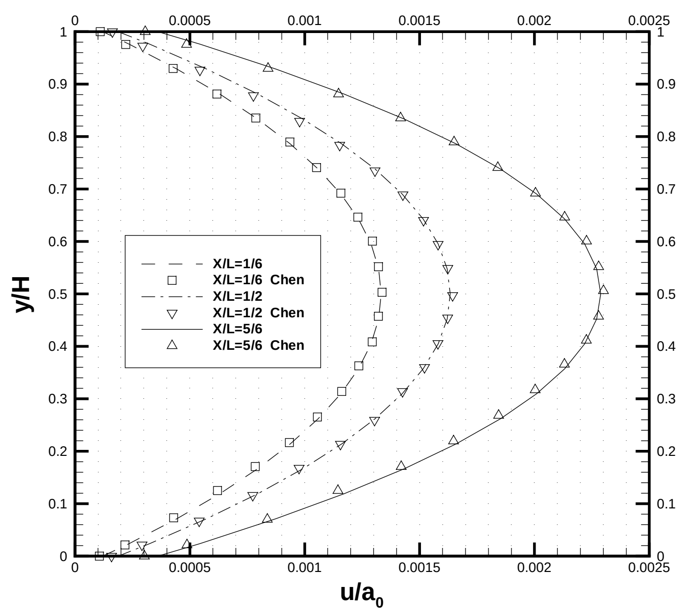

Figure 2.8: The u-velocity of the current numerical study versus that of Chen et al.'s [2] numerical investigation at three streamwise locations.

Table 2.1: Parameters of microchannel nitrogen flows.

Parameter	Channel#1	Channel#2
Length L	3000μm	1500μm
Height H	1.2μm	3μm
Pressure Ratio $PR = P_{in}/P_{out}$	1.34, 1.68, 2.02, 2.361, 2.701	1.5, 2.0, 2.5, 3.0, 3.5
Inlet Temperature T_0	314K	300K
Density of Nitrogen at Inlet temperature and $1 \times 10^5 Pa$ ρ_0	1.0783 kg/m^3	1.1233 kg/m^3
Outlet Pressure P_{out}	$1 \times 10^5 Pa$	$1 \times 10^5 Pa$
Inlet Dynamic Viscosity μ_0	1.843 $\times 10^{-5}$ N $\cdot$ s/m^2	1.782 $\times 10^{-5}$ N $\cdot$ s/m^2
Inlet Thermal Conductivity k_0	2.68 $\times 10^{-2}$ W/(K·m)	2.59 $\times 10^{-2}$ W/(K·m)
Inlet Sound Speed a_0	361.21m/s	353.07m/s
Inlet Specific Heat c_p	1041 J/(kg·K)	1041 J/(kg·K)
Specific Gas Constant R	296.8 J/(kg·K)	296.8 J/(kg·K)
Specific Heat Ratio γ	1.4	1.4

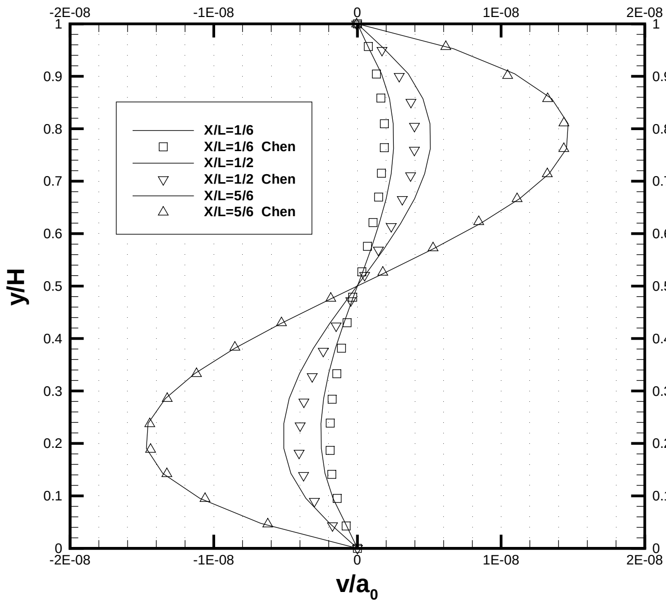

Figure 2.9: The v-velocity of the current numerical study versus that of Chen et al.'s [2] numerical investigation at three streamwise locations.

2.4 Physical Modeling Issues

2.4.1 Variable Properties

During the physical modeling, the first main concern is on the variable properties. As is well known, gas properties vary with temperature. For example, when temperature rises from 300K to 350K, the dynamic viscosity of nitrogen increases by 12%. The question is: Compared to variable property model, will constant property model make a big difference? Liu et al. [29] and Mahulikar et al. [30] conducted independent studies on the variable property effects for incompressible microchannel flows. Both groups found the distorted velocity and thermal field due to the viscosity and thermal conductivity changes. Also for the incompressible flows, Tso and Mahulikar [31, 32, 33] tried to use the variable property effects to interpret the unexplained experimental findings of Wang and Peng's [34] as well as Peng and Peterson's [35, 36]. On the other hand, for the microchannel compressible gas flows, the variable property effects are not investigated much. For the cases with the isothermal walls as well as the fixed inlet and outlet pressures, the mass flow rate will decrease with the wall temperature due to the increased viscosity. If the thermal entrance length is sufficiently short compared to the whole channel length, constant property model using the gas properties at wall temperature should be a very good approximation. For the cases with uniform heat flux (H2) wall boundary condition, the magnitude of variable property effects is not that easy to tell and thus will be investigated below.

The effects of variable properties for different outlet/inlet bulk temperature ratios are measured for the Channel #2 (Table 2.1), where the inlet/outlet pressure ratio is fixed at 2.0. The grid size is set to 2300×29 ($X \times Y$) based on the grid dependence test results in Table 2.2 for the case with $\bar{q}_w = \frac{q_w H}{T_0 k_0} = 2 \times 10^{-4}$. The same channel and inlet/outlet pressure ratio will be used for all cases involved in section 2.4 on the physical modeling issues. For all cases involved in section 2.4, the convergence criteria for the final serial run is $\varepsilon < 1 \times 10^{-12}$. First, a case with small outlet/inlet bulk temperature ratio is studied through Fig. 2.10 (a)-(d), which compare the results between variable property model and constant property model under the same uniform wall heat flux boundary condition $\bar{q}_w = 5 \times 10^{-5}$. The outlet/inlet bulk temperature ratio for the case in Fig. 2.10 is around 1.08 as shown in Fig. 2.10 (c). The constant property model uses the properties at the inlet temperature. Fig. 2.10 (a)-(d) shows that the difference between the results of constant property model and variable property model is within 3%. The difference on mass flow rate, which is not shown in Fig. 2.10, is also within 3%. Therefore, the effect of variable property is negligible for small outlet/inlet bulk temperature ratio cases. A case with large outlet/inlet bulk temperature ratio is studied through Fig. 2.11 (a)-(d), which compare the results between variable property model and constant property model under the same uniform wall heat flux boundary condition $\bar{q}_w = 2 \times 10^{-4}$. The outlet/inlet bulk temperature ratio for the case in Fig. 2.11 is around 1.4 as depicted by Fig. 2.11 (c). As in the small outlet/inlet bulk temperature ratio case, the constant property model uses the properties at the inlet temperature. Fig. 2.11 (a) shows that constant property model can very well predict the local Nusselt number along the microchannel. The maximum difference on the local Nusselt number between the two models is below 3%. Fig. 2.11 (b) shows that constant

Table 2.2: Grid dependence test results for Channel #2. (a)Centerline temperature; (b)Centerline streamwise velocity.

(a) T_{center}/T_0

Grid	$x = 300\mu m$	$x = 600\mu m$	$x = 900\mu m$	$x = 1200\mu m$
750×11	1.08162834	1.16287437	1.24344603	1.32257181
1100×15	1.08338110	1.16609956	1.24776242	1.32738766
1500×19	1.08388886	1.16693878	1.24868975	1.32802466
2300×29	1.08396035	1.16682244	1.24803444	1.32630770
3000×37	1.08389450	1.16660243	1.24753322	1.32532099

(b) $u_{center}/a_0 \times 100$

Grid	$x = 300\mu m$	$x = 600\mu m$	$x = 900\mu m$	$x = 1200\mu m$
750×11	0.84529697	0.98539234	1.17433592	1.45808546
1100×15	0.83699282	0.97603252	1.16338625	1.44486089
1500×19	0.83425868	0.97282813	1.15942272	1.43967512
2300×29	0.83286107	0.97091163	1.15661000	1.43527115
3000×37	0.83265412	0.97053341	1.15592931	1.43401807

property model underestimates the bulk temperature rise along the channel by up to 10%. Fig. 2.11 (c) presents the shear stress at the wall. It is found that constant property model overestimates the wall shear in the region close to the inlet, while gives underestimation near the outlet. To identify the overall influence of the wall shear, the mass flow rates predicted by the two models are compared. It is found that the constant property model overestimates the mass flow rate by 14%. The volume flow rate along the microchannel is shown in Fig. 2.11 (d), from which it is found that constant property model gives higher volume flow rate. In conclusion, for large outlet/inlet bulk temperature ratios, constant property model will not make much difference on the Nusselt number, however, could cause more than 10% deviation on other characteristic quantities.

2.4.2 Source Terms in Energy Equation

Since the length-to-height ratios of most macrochannels are very small compared to those of most microchannels, pressure work and viscous dissipation are normally ignored in the modeling of macrochannel gas flows. For microchannel gas flows, viscous dissipation has been shown to be nonnegligible [18, 19]. Compressibility effects have also been explored by some groups [20, 21], but more on fluid field rather than thermal

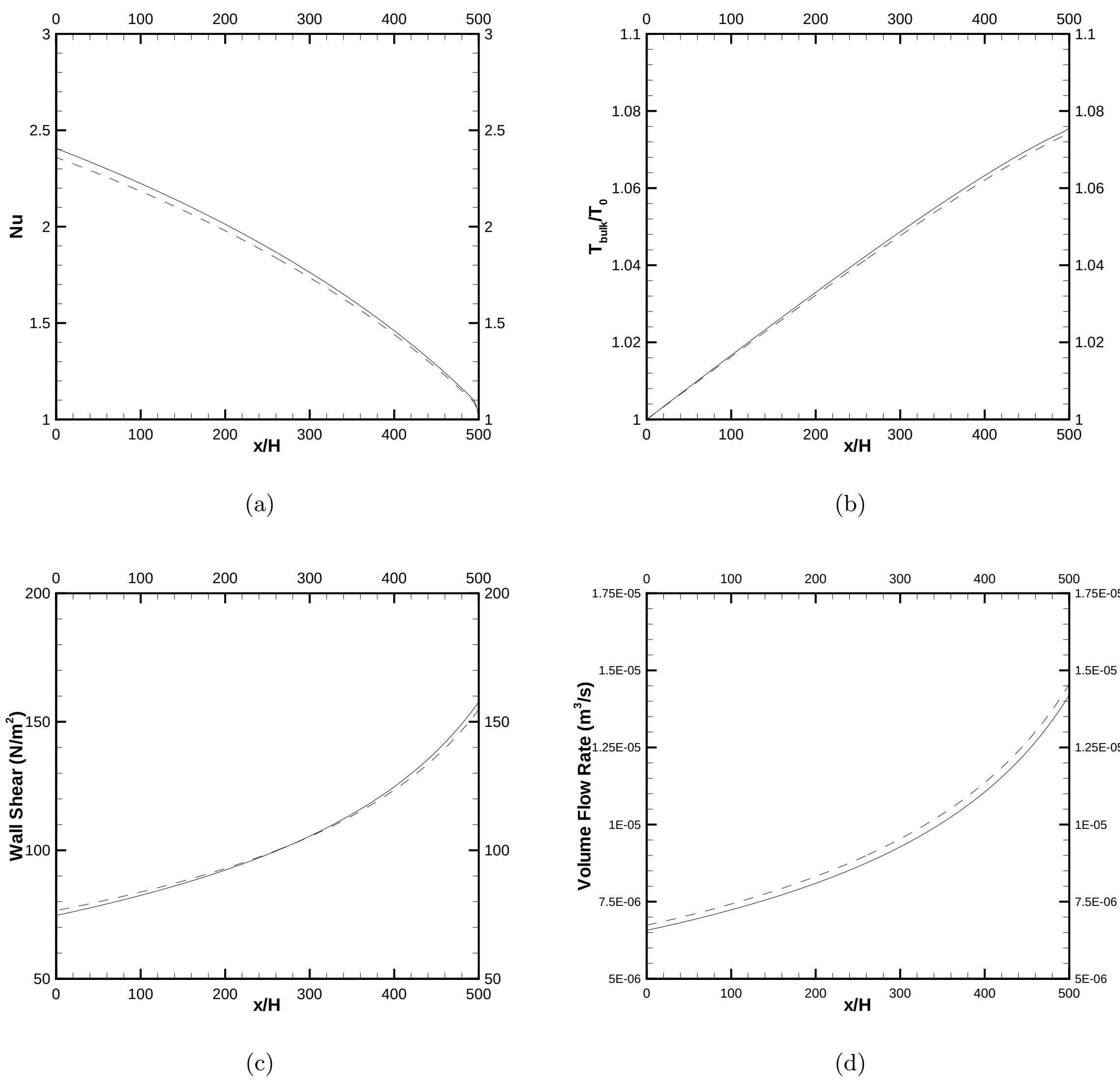

Figure 2.10: Comparison of variable property model with constant property model for a case with H2 type wall boundary condition $\bar{q}_w = 5 \times 10^{-5}$. (a) Nusselt number; (b) Bulk temperature; (c) Wall shear stress; (d) Volume flow rate. The solid lines denote the results from variable property model, while the dash lines denote those from constant property model.

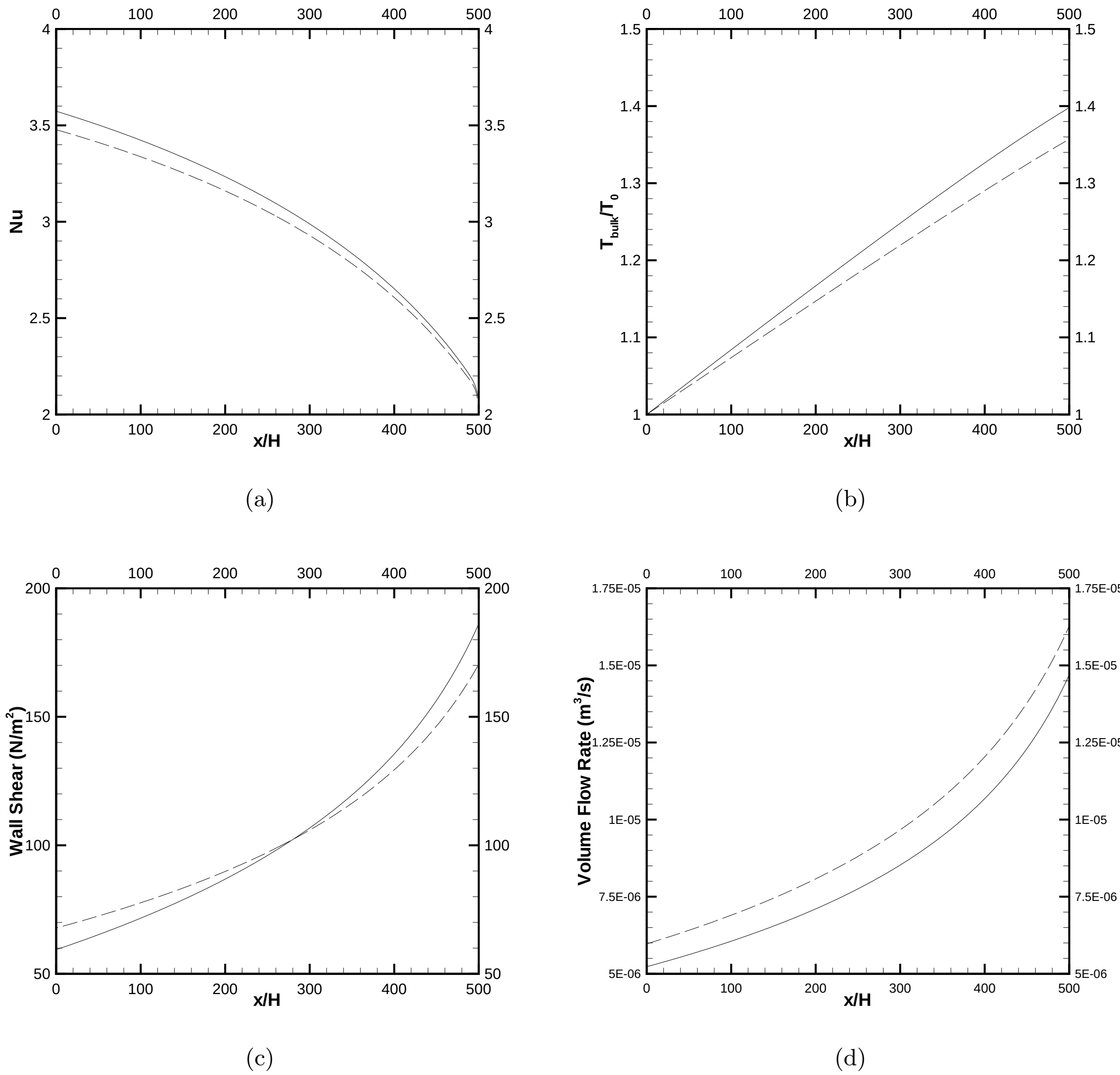

Figure 2.11: Comparison of variable property model with constant property model for a case with H2 type wall boundary condition $\bar{q}_w = 2 \times 10^{-4}$. (a) Nusslet number; (b) Bulk temperature; (c) Wall shear stress; (d) Volume flow rate. The solid lines denote the results from variable property model, while the dash lines denote those from constant property model.

field. In their paper on size effect, Guo and Li [37] gave a brief but very insightful discussion on the source terms in energy equation. In fact, for the compressible flows in our real life, the energy loss due to thermal expansion is a very prominent effect, which is, for example, the working mechanism of many engines. For the cases with isothermal wall boundary condition and short entrance length, although pressure work and viscous dissipation will determine the amount of energy that needs to be either removed from or fed to the flow, the bulk temperature will remain almost constant for the majority part of the channel length and hence the source terms will not make sensible impact on fluid field. In contrast, for the cases with uniform heat flux (H2) wall boundary conditions, even if constant property model is used, because of the source terms, the bulk temperature profile along the channel is still possible to be pulled away from linear distribution. Therefore, in next paragraph, the source terms in energy equation will be carefully examined for the H2 type wall boundary condition.

Similar to the approach employed in the investigation of variable property effects, the low and high heat flux cases are studied separately. First, for a low heat flux case with $\bar{q}_w = 5 \times 10^{-5}$, four different models are investigated. The first model includes both pressure work (PW) and viscous dissipation (VD); the second one includes PW only; the third one includes VD only; and the fourth one includes neither PW nor VD. Since the source terms in energy equation will directly influence thermal field only, bulk temperature (Fig. 2.12) is the only parameter used to compare the four models. From Fig. 2.12, it is found that either VD or PW, if solely considered, is very important and could cause very large error if missed in modeling. On the other hand, their combined effects are relatively small, where the error on bulk temperature rise is about 10%. For a large heat flux case with $\bar{q}_w = 2 \times 10^{-4}$, the same four models as those employed in low heat flux case are used to investigate the effect of the energy equation source terms. As shown in Fig. 2.13, similar to the findings in Fig. 2.12, the sole neglect of either VD or PW could cause huge error, while the error caused by the neglect of both is relatively small - only about 5% error on bulk temperature rise. Therefore, the combined influence of PW and VD is more significant for small heat flux cases.

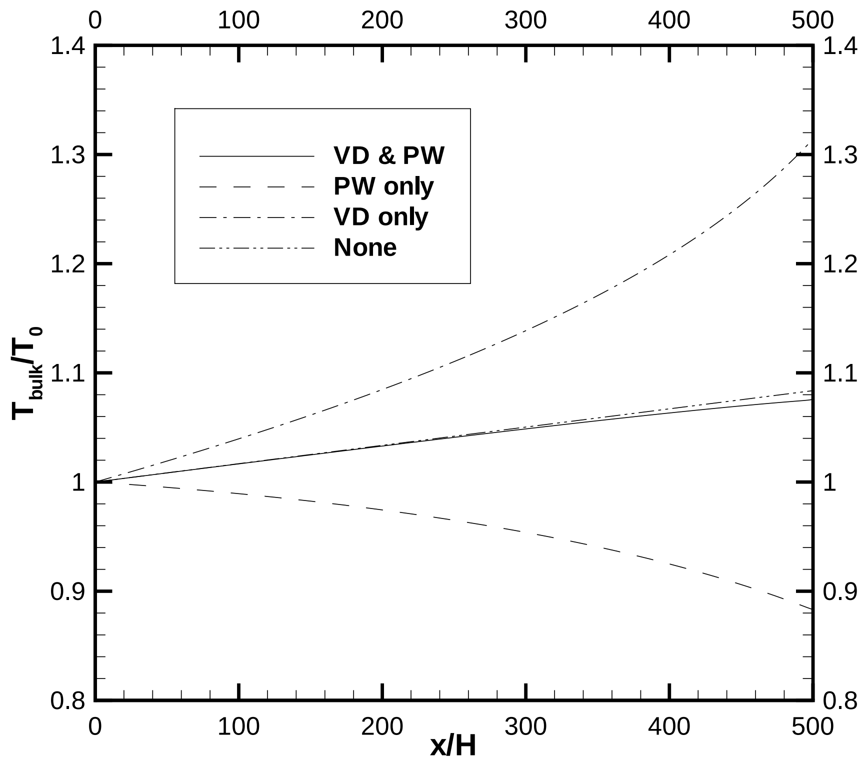

Figure 2.12: Comparison of bulk temperature profiles for four cases with the same H2 type wall boundary condition $\bar{q}_w = 5 \times 10^{-5}$, but modeled in four different ways: PW & VD - including both pressure work (PW) and viscous dissipation (VD); VD only - including VD only; PW only - including PW only; None - including neither.

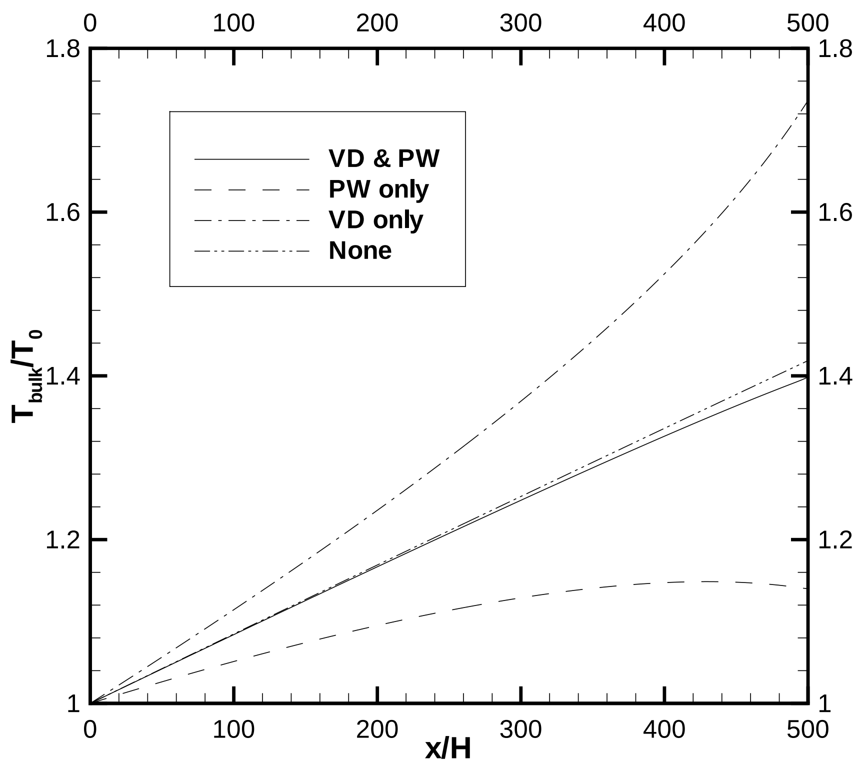

Figure 2.13: Comparison of bulk temperature profiles for four cases with the same H2 type wall boundary condition $\bar{q}_w = 2 \times 10^{-4}$, but modeled in four different ways: PW & VD - including both pressure work (PW) and viscous dissipation (VD); VD only - including VD only; PW only - including PW only; None - including neither.

2.4.3 Is the Traditional Continuum Model Good Enough for Microchannel Gaseous Slip Flows?

Apart from variable properties and the source terms in energy equation, based on my literature review, rarefaction has been very well considered by almost every numerical or analytical study on microchannel gas flows. Velocity slip and temperature jump wall boundary conditions are thought to be capable of interpreting the difference between micro- and macroscale gas flows. Therefore, to model microchannel gas flows, rarefaction, the source terms in energy equation and variable properties should all be included. Then the author comes up with another question: How much will be the deviation, if microchannel gas flows are modeled in the same way as for most macrochannel gas flows? First, for microchannel gas flows with isothermal wall boundary condition, apparently the traditional continuum model will underestimate mass flow rate and thus fail to describe the fluid field accurately. To answer the same question for microchannel gas flows under constant heat flux (H2) boundary condition, again the low and high heat flux cases are studied separately. First, for a low heat flux case with $\bar{q}_w = 5 \times 10^{-5}$, two models are compared: Model A (the model proposed for microchannel gas flows) incorporates variable properties, rarefaction and the source terms in energy equation; Model B (the traditional continuum model for most macrochannel gas flows) uses constant properties at inlet temperature, and excludes rarefaction as well as the source terms in energy equation. Fig. 2.14 (a) shows the comparison on the Nusselt number. It is found that Model B gives a constant Nusselt number around 4.27, while under Model A, the Nusselt number decreases along the channel. From Fig. 2.14 (b), it is found that Model B overestimates the bulk temperature rise up to more than 20%. Fig. 2.14 (c) shows that the difference on local wall shear stress along the channel between Model A and Model B is merely up to 3%. The difference on mass flow rate between the two models that is not shown here is within 7%. Fig. 2.14 (d) shows that volume flow rate is underestimated by up to 6% under Model B. Therefore, for this low heat flux case, the difference between the two models on fluid field is below 10%, while that on thermal field could be beyond 20%. Fig. 2.15 (a)-(d) compare Model A with Model

B for a large heat flux case with $\bar{q}_w = 2 \times 10^{-4}$. Fig. 2.15 (a) shows very similar findings to those shown in Fig. 2.14 (a). So for both low and high heat flux cases, there exists a qualitative difference between the Nusselt numbers predicted by the two models. Fig. 2.15 (b) shows that Model B overestimates bulk temperature rise by up to 5%. Fig. 2.15 (c) compares the local wall shear stress, where it is found that the difference between the two Models is within 6%. The difference on mass flow rate between the two models that is not shown here is within 1%. It is found in Fig. 2.15 (d) that the difference on local volume flow rate between the two models is within 3%. Therefore, for this large heat flux case, the difference between the two models is smaller compared to the above small heat flux case except for the Nusselt number. Based on the results in Fig. 2.14 and Fig. 2.15, it can be concluded that, for microchannel gas flows, the traditional continuum model (Model B) can lead to both qualitative and quantitative differences compared to the model proposed for microchannel gas flows (Model A).

2.5 Summary

In this chapter, some modeling issues are investigated for microchannel gas flows. Numerically, to resolve the intense computation required by the large computational domain and quasi-steady nature of the problems, a parallel SIMPLER-based solver is used together with the serial version. Some implemental issues related to the parallel solver is discussed and solved. Physically, the influence of variable properties and the source terms in energy equation are measured. It is found that variable property model needs to be used for large outlet/inlet bulk temperature ratio cases, while for low outlet/inlet bulk temperature ratio cases, the influence of variable properties is negligible. For the source terms in energy equation, either pressure work or viscous dissipation, if solely neglected, could cause huge error. However, if pressure work and viscous dissipation are both neglected, the resulted error is relatively small. Finally, the traditional continuum model (using constant properties at inlet temperature, neglecting pressure work and viscous dissipation as well as rarefaction) is compared with the proposed model for microchannel gas flows (using variable properties, including both pressure work and

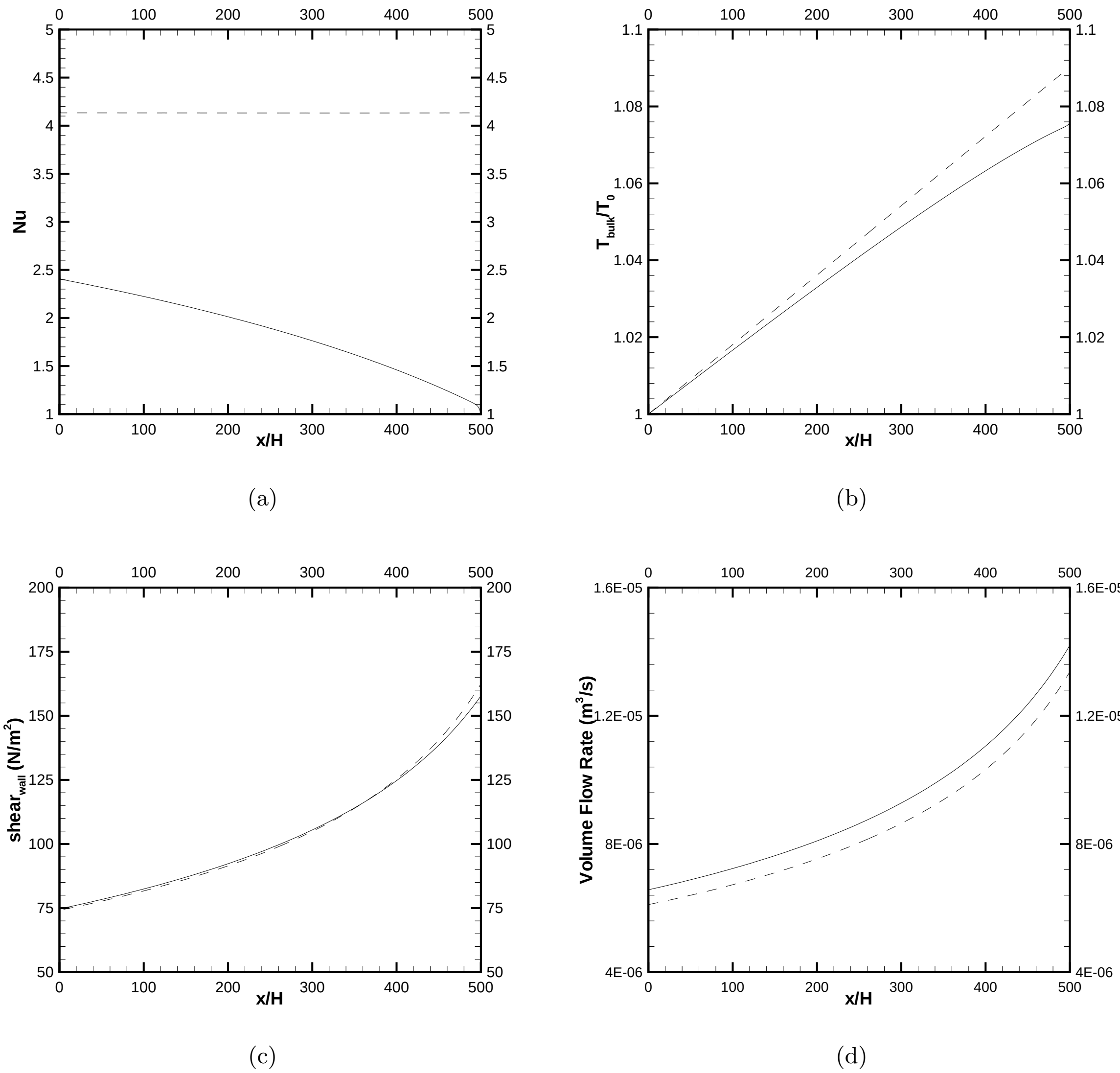

Figure 2.14: Comparison of the two cases with the same H2 type wall boundary condition $\bar{q}_w = 5 \times 10^{-5}$, but using two different models: Model A (solid lines) incorporates variable properties, rarefaction and the source terms in energy equation; Model B (dashed lines) uses constant properties at inlet temperature, and excludes rarefaction as well as the source terms in energy equation. (a) Nusslet number; (b) Bulk temperature; (c) Wall shear stress; (d) Volume flow rate.

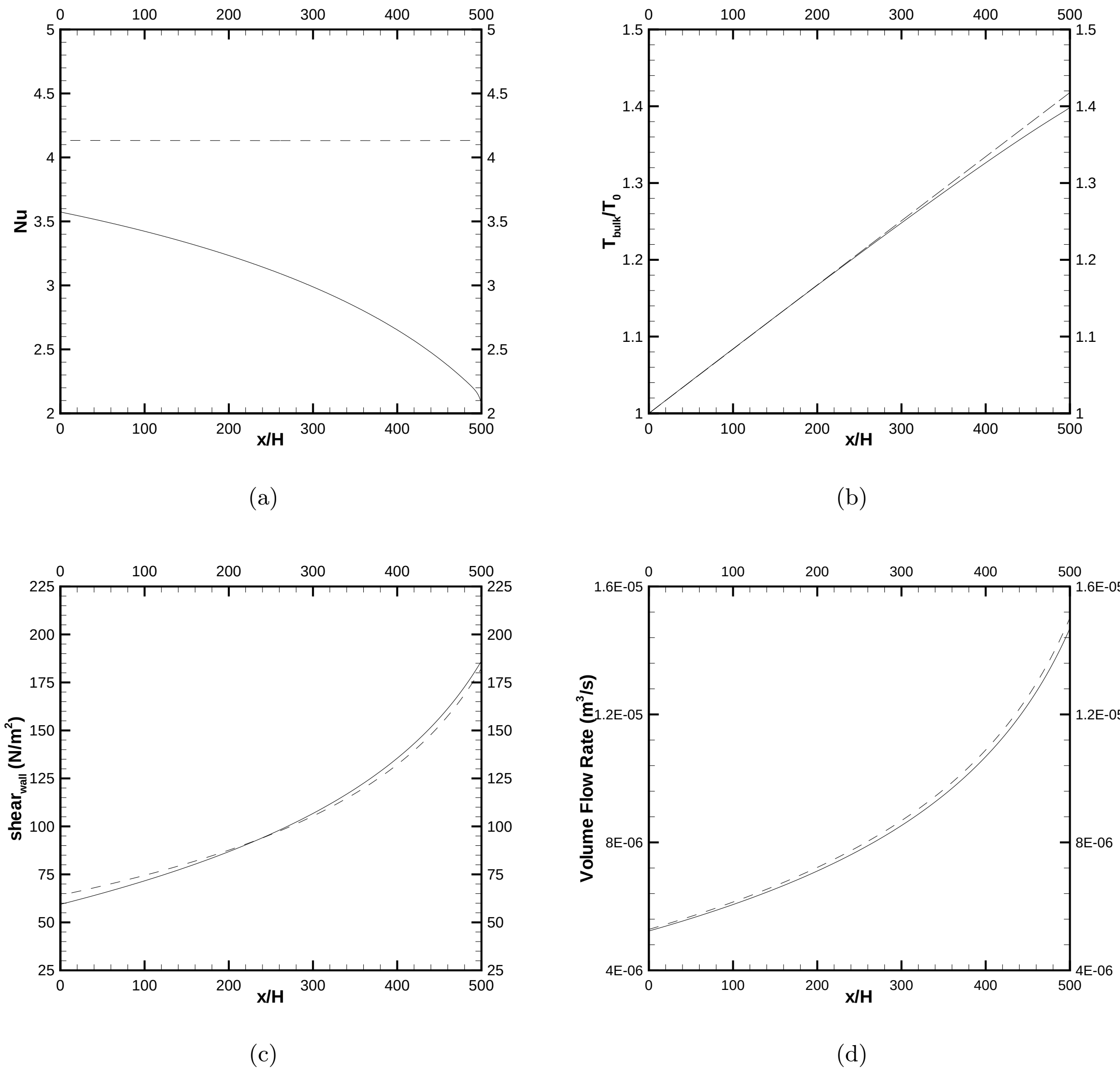

Figure 2.15: Comparison of the two cases with the same H2 type wall boundary condition $\bar{q}_w = 2 \times 10^{-4}$, but using two different models: Model A (solid lines) incorporates variable properties, rarefaction and the source terms in energy equation; Model B (dashed lines) uses constant properties at inlet temperature, and excludes rarefaction as well as the source terms in energy equation. (a) Nusslet number; (b) Bulk temperature; (c) Wall shear stress; (d) Volume flow rate.

viscous dissipation as well as rarefaction). It is concluded that, the traditional continuum model can lead to both qualitative and quantitative differences compared to the model proposed for microchannel gas flows.

Chapter 3

Two Dimensional Steady-State Pressure-Driven Nitrogen Flow in Long Microchannels Under Isothermal Wall Boundary Condition

3.1 Introduction

In the early 1990s, several groups of experimentalists reported the discrepancy between microchannel flows and the continuum theory [7, 8, 9, 10]. To understand microscale gaseous convection, many analytical and numerical studies are conducted. Arkilic et al. [13] studied pressure-driven helium flow in a long microchannel both analytically and experimentally. It was found that by taking velocity slip and compressibility into account, 2D Navier-Stokes equations could fairly accurately predict mass flow rate. Instead of using velocity slip and temperature jump to model the laminar microscale fully developed flow, Li et al. [14] proposed the 'wall-adjacent layer', where the change of gas thermal conductivity results in significant influence on heat transfer and is able to make accurate qualitative predictions. The laminar fully developed slip-flow forced convection in rectangular microchannels with isothermal wall boundary condition was investigated analytically by Yu and Ameel [15]. They discussed the effects of velocity slip and temperature jump on Nusselt number and showed that, compared to no-slip flow condition, heat transfer could be either reduced or enhanced. In a recent paper, Chen [18] carried out an analytical study on the developing thermal field in laminar forced convection in a microchannel with isothermal wall boundary condition, where viscous dissipation was considered in addition to rarefaction, while fluid field was still assumed to be full-developed. Jeong and Jeong [19] extended Chen's [18] work by including axial conduction into their analysis. To solve the developing fluid field, many numerical studies have been completed. Beskok et al. [20] presented their numerical simulations, where rarefaction, compressibility, viscous dissipation as well as thermal creep were considered. They discussed the competing effects of compressibility and rarefaction on the nonlinear pressure distribution of the gas flow in long microchannels, which interpreted the findings of Pong et al. [9]. Guo and Wu [21] numerically studied compressibility effects on gas flow and heat transfer in a microtube, where rarefaction were not considered. They concluded that fully developed pressure-driven gas flow does not exist due to compressibility. It was also shown by Guo and Wu [21] that, because of the large dependence of thermal field on fluid field, for microchannel gas flows with non-negligible Mach number, fully developed thermal field does not arise. To reproduce the experimental results by Pong et al. [9], Chen et al. [2] conducted 2D numerical simulations, where the flow was modeled as compressible with rarefaction and viscous dissipation. Raju and Roy [23] studied supersonic microchannel flows and compared their results with published direct-simulation Monte Carlo results.

Based on my literature review, to my best knowledge, most published numerical studies on microchannel gas flows are 2D jobs and use constant gas properties. So far, no comprehensive numerical studies have been completed on the developing fluid and thermal fields of pressure-driven gas flow in long microchannels with length-to-height ratio in the order of $10^3 : 1$. The study on flow in long microchannels is motivated by the fact that, very short microchannels are rarely used in practice. As an extension of Chapter 2, this chapter concentrates on isothermal wall boundary condition. The organization is as follows: section 3.2 briefs the numerical model; section 3.3 presents the numerical results and the discussion; finally, conclusions are given in section 3.4.

3.2 Numerical Model Description

The readers can refer to Chapter 2 for mathematical model and numerical procedure. In this chapter, nitrogen gas flows with isothermal wall boundary conditions are investigated. Variable properties, rarefaction effects (velocity slip, thermal creep and temperature jump), compressibility and viscous dissipation are all included. The employed computational method is based on the SIMPLER algorithm and has both a serial and a parallel version. The parallel solver is built with the domain decomposition method (DDM). As we did before, the parallel solver is first employed and runs until some convergence criteria are reached. Then to eliminate the singularity caused by the DDM, the results from the parallel solver are fed to the serial solver, which then runs until the desired convergence is achieved. To get the steady state solution, time marching method is used. The convergence criteria for the parallel solver are of the form

$$\varepsilon = \max \left\{ \begin{array}{ll} \text{if } \xi^n \neq 0 & \frac{|\xi^{n+1}-\xi^n|}{|\xi^n|} \\ \text{if } \xi^n = 0 & |\xi^{n+1}| \end{array} \right\} \tag{3.1}$$

where ξ applies to streamwise velocity u, temperature T as well as the variables in the overlapping regions of the subdomains and the superscripts denote the time step. The convergence criteria for the serial solver take the same form as for the parallel solver, while ξ only applies to streamwise velocity u and temperature T. The computation for all the cases involved in this chapter stopped running when ε falls below 1×10^{-8} for the final serial run. In this chapter, the channel to be studied is the Channel #1, which is given in Fig. 2.1 and Table 2.1 in Chapter 2. The grid size remains the same as that employed in Chapter 2 for Channel #1, i.e., 6000×23 (X×Y).

3.3 Results and Comments

In this section, the results of the 2D simulations of microchannel pressure-driven nitrogen flow with isothermal wall boundary condition are presented and analyzed. The Channel #1 described by Fig. 2.1 and Table 2.1 in Chapter 2 is employed. The inlet temperature, T_w, is fixed at 314K. In section 3.3.1, the effects of different wall temperatures are studied through four cases, in which the wall temperature over inlet temperature ratio, T_w/T_0, is set to 1.2, 1.4, 1.6, and 1.8, respectively. For these four cases, the inlet/outlet pressure ratio, $PR = P_{out}/P_{in}$, is fixed at 2.701, and the outlet pressure is fixed at $1 \times 10^5 Pa$. The rarefaction effects are also studied in section 3.3.1. Then in section 3.3.2, the influence of the inlet/outlet pressure ratio is investigated, where the inlet/outlet pressure ratio is tuned from 1.340 to 2.701 and the T_w is fixed at 1.2. Finally, some comments are made in section 3.3.3.

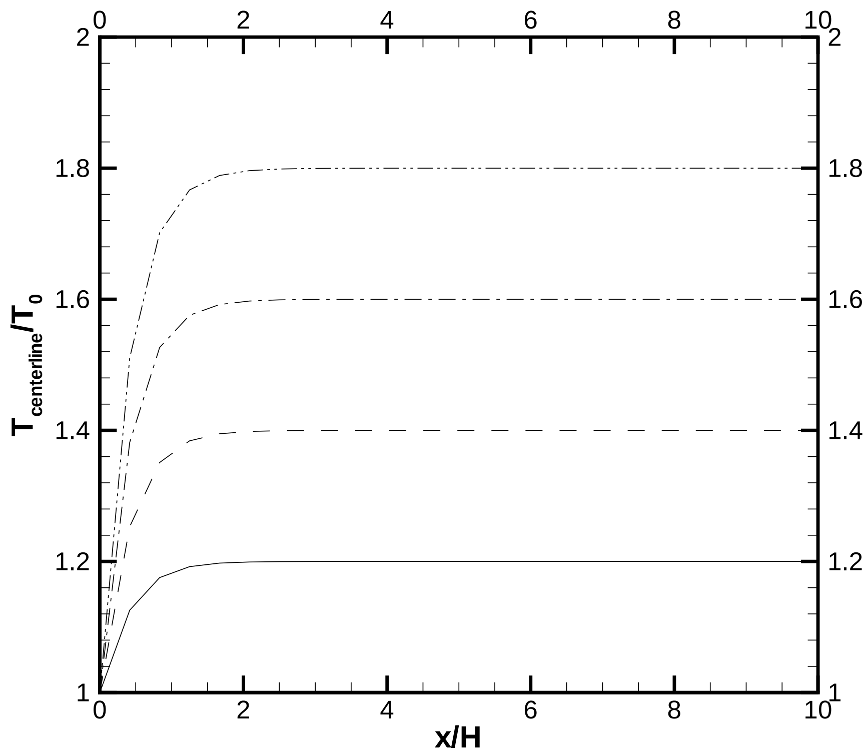

Figure 3.1: Centerline temperature profile in thermal entrance region for the cases with different T_w/T_0's at 1.2, 1.4, 1.6, and 1.8, respectively.

3.3.1 Wall Temperature

Fig. 3.1 gives the streamwise centerline temperature profile for the cases with different T_w's, where only the entrance region is shown. It is found that the entrance length required for the development of thermal field is merely up to a few channel heights. In the thermally developed region, the temperature profile on a cross section that is not shown here is found to be almost flat with the centerline temperature slightly lower than the wall temperature. Therefore, after the short thermal entrance region, the microchannel nitrogen flow with isothermal wall boundary condition becomes almost a pure fluid field problem.

Fig. 3.2 shows local Nusselt number (Nu) along the channel in the thermal entrance region, where

$$Nu = \frac{q_w H}{k(T_w - T_{bulk})} \tag{3.2}$$

From Fig. 3.2, it is found that, in thermal entrance region, Nu first drops to somewhere between 3.0 and 4.0, then drops again to somewhere below unity. The first drop of Nu is due to the development of thermal field. Before the second drop of the Nu, wall heat flux is dominant over energy generation or loss (the combined effect of viscous dissipation and pressure work) within the flow. After thermal field is developed, pressure work (PW) and viscous dissipation (VD) turn out to be the main mechanism and thus combine to play the major role on Nu. So the second drop of Nu basically characterizes the switch of the dominance on Nu from wall heat flux to energy generation or loss within the flow. The decrease of Nu before the second drop as T_w can be explained by the adverse influence of rarefaction on Nu in engineering conditions as shown by Yu and Ameel [15] as well as Jeong and Jeong [19]. That is, velocity slip promotes mass and hence energy transport at wall, while temperature jump increases thermal resistance at wall. For nitrogen, it has been shown [15, 19]that, temperature jump is dominant over velocity slip in the competition on Nu and hence larger Kn leads to lower Nu. As shown later in Fig. 3.4, Kn increases as T_w at a given streamwise position, which results in the decrease of Nu as T_w before the second drop of Nu. In Fig. 3.3, to study rarefaction effects, Kn is set to zero for the four cases in Fig. 3.2. It is found that without rarefaction, Nu still drops twice in entrance region: first drops to a constant around 4.10, then drops again to another constant around minus 0.68. The mechanism for the two drops is the same as that for the cases with rarefaction. The coincidence on the two constants (4.10 and minus 0.68) for the cases with different T_w's is due to the removal of rarefaction.

Fig. 3.5 shows Nu after its second drop. For the cases with $Kn = 0$, after its second drop, Nu remains constant at minus 0.68. For the cases with nonzero Kn, Nu increases after its second drop till the outlet of the channel and increases as T_w. To understand the behavior of Nu after its second drop, the ratio of PW over VD is plotted in Fig. 3.6, where only the cases with nonzero Kn's are visible. It is found that the magnitude of PW/VD ratio increases as T_w and along the channel. For the cases with $Kn = 0$, PW/VD ratio that is not shown here is found to be constant at minus unity. As pointed out above and based on Fig. 3.6, after the second drop of Nu, the energy loss within

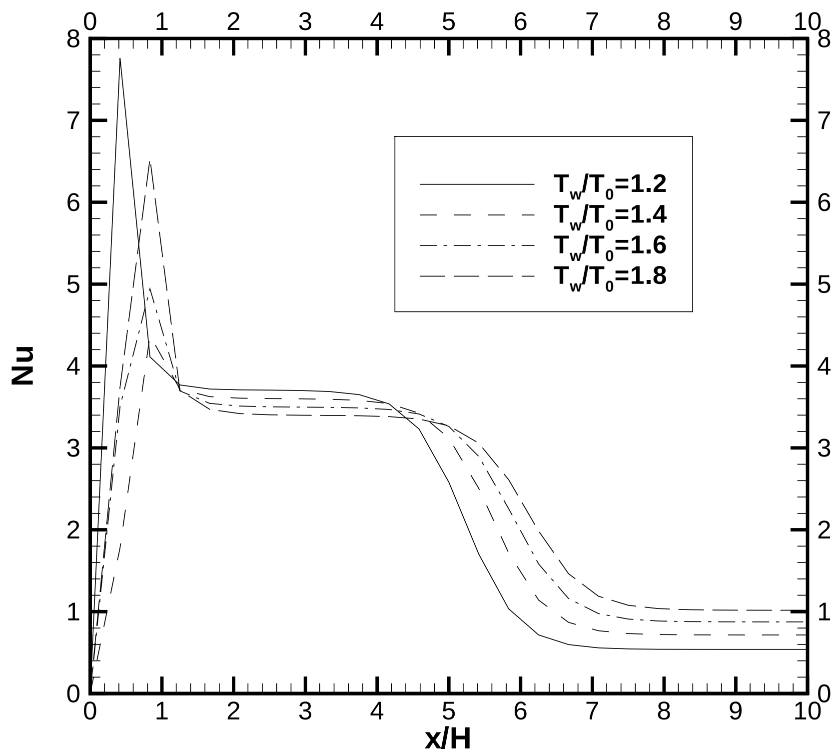

Figure 3.2: Local Nusselt number in thermal entrance region for the cases with different wall temperatures and $Kn > 0$.

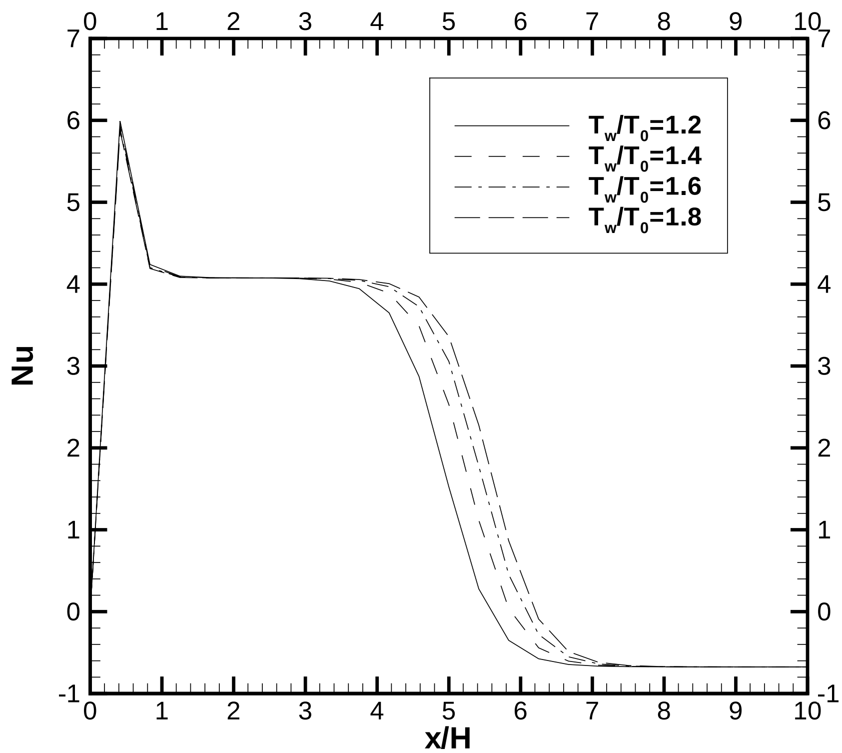

Figure 3.3: Local Nusselt number in thermal entrance region for the cases with different wall temperatures and $Kn = 0$.

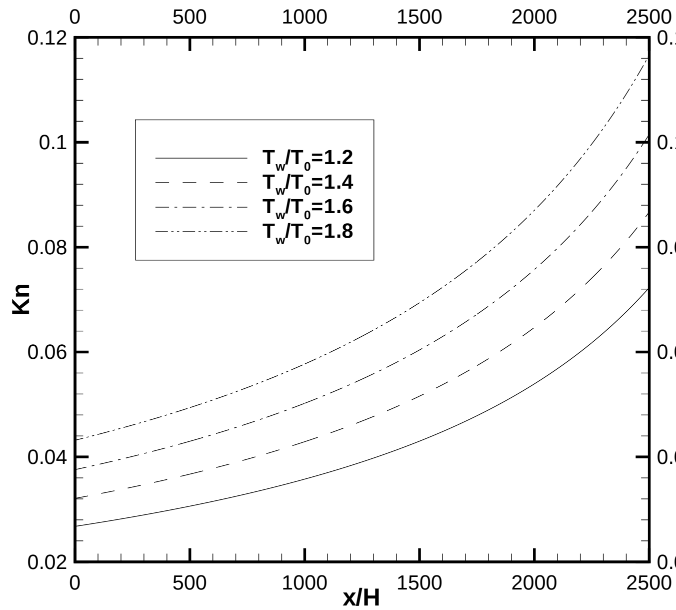

Figure 3.4: Knudsen number for the cases with different wall temperatures.

the flow is dominant on Nu. Rarefaction, which is characterized by Kn, decreases VD close to the wall and increases the velocity near centerline due to the reduced friction at wall. If the increased velocity as rarefaction near centerline is combined with the almost unchanged pressure distribution (Fig. 3.7), PW near centerline will increase as rarefaction. According to Fig. 3.4, Kn increases as T_w, which directly results in the increase of PW/VD ratio magnitude as T_w in Fig. 3.6. Therefore, higher T_w's lead to higher Nu's as shown in Fig. 3.5. Similarly, the trend of Nu along the channel can be explained by the fact that the magnitude of PW/VD ratio increases along the channel as shown in Fig. 3.6. For the cases with Kn=0, based on the fact that PW/VD is constant at minus unity, VD and PW cancel out, which makes the constant Nu possible. The negative Nu's for the cases without rarefaction is primarily caused by the VD close to the wall. Apart from Nu, the magnitude of PW/VD ratio (> 1) can also interpret the temperature profile at a cross section: the lower centerline temperature is caused by the energy loss near the centerline and the energy generation near the channel wall.

Fig. 3.8(a) compares u-velocity profiles of the two cases with different T_w's at three streamwise locations. It is found that u-velocity decreases as T_w, and this trend is

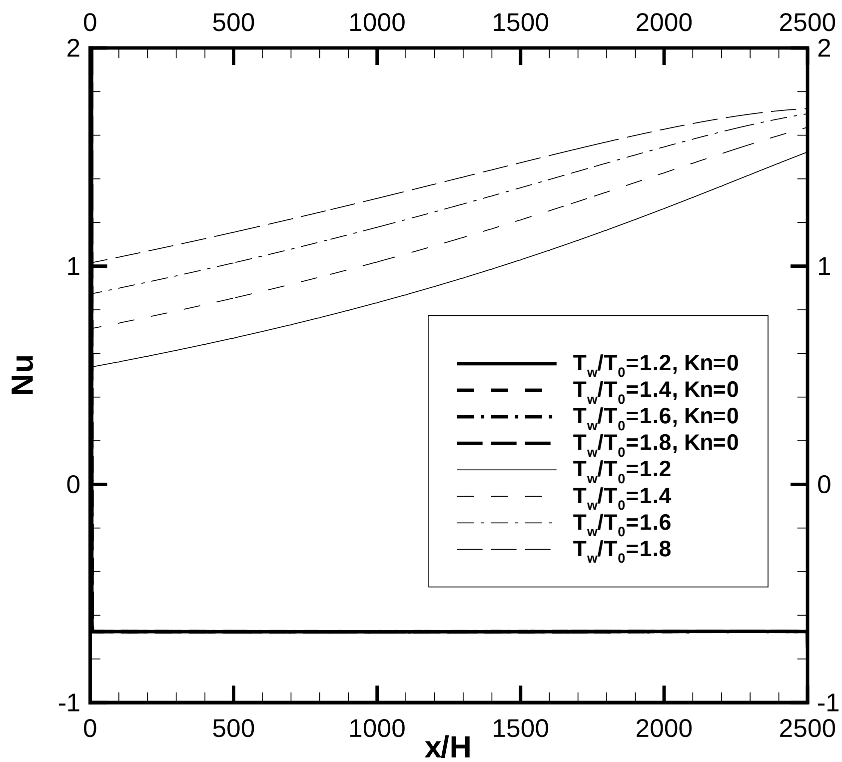

Figure 3.5: Local Nusselt number in thermally developed region for the cases with different wall temperatures.

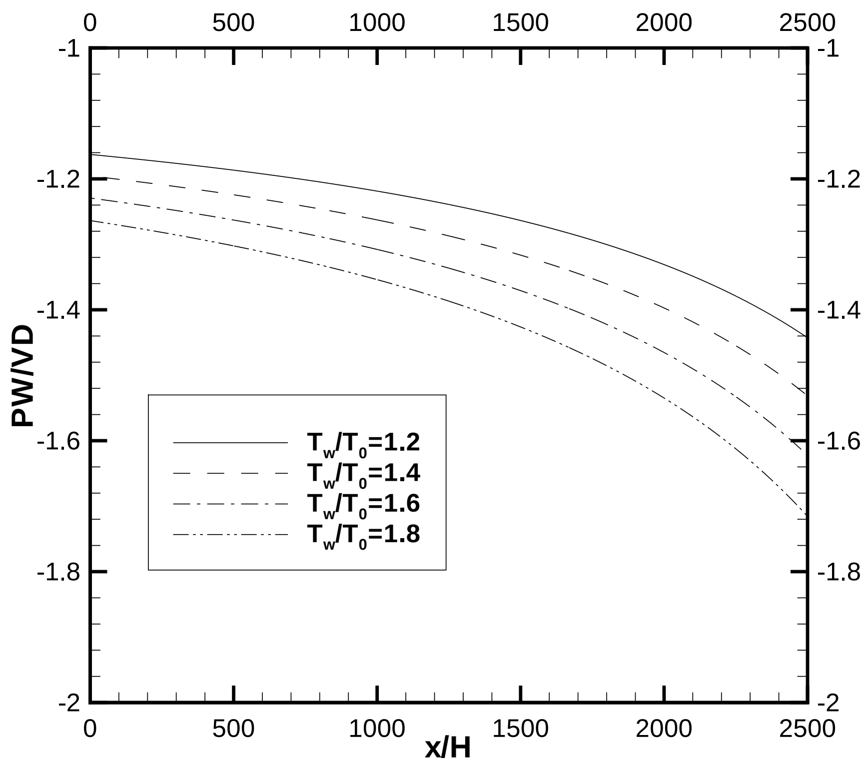

Figure 3.6: Local pressure work over viscous dissipation ratio for the cases with different wall temperatures.

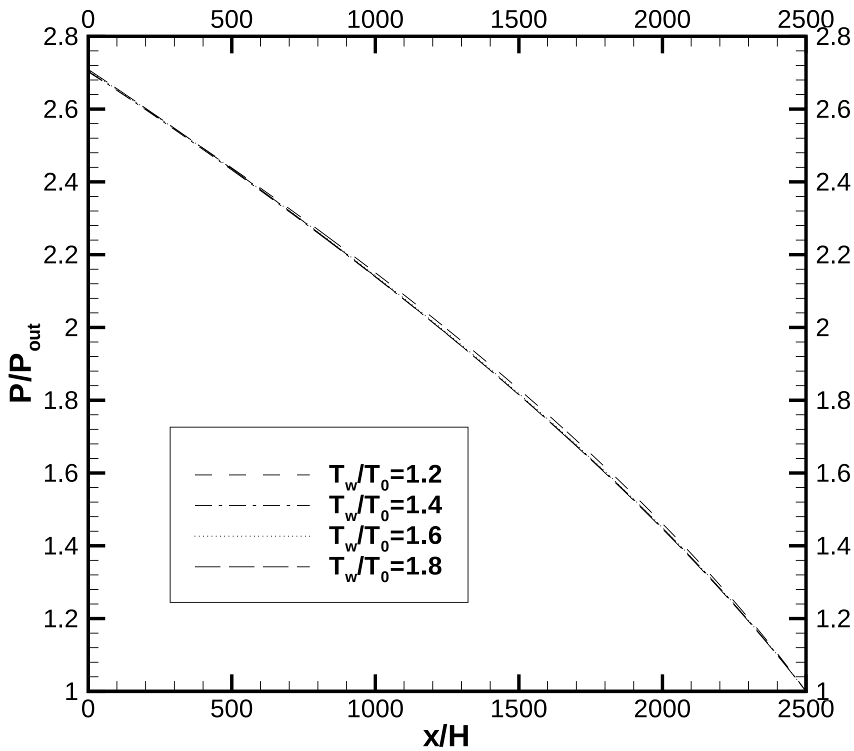

Figure 3.7: Centerline pressure distribution for the cases with different wall temperatures.

true for all four T_w's studied. Fig. 3.8(b) compares v-velocity profiles at the same streamwise locations. Contrary to the trend found in Fig. 3.8(a), v-velocity increases as T_w goes up, and this trend is true for all four T_w's studied. Fig. 3.8(a) and (b) clearly demonstrate the fact that fluid field is not at all fully developed even for very long microchannels. The wall conditions are summarized in Fig. 3.9 and 3.10. Fig. 3.9(a) shows that wall shear stress increases as T_w and along the channel. It is clear that viscosity keeps constant along the channel, so $(du/dy)_{wall}$ must increase along the channel as shown in Fig. 3.9(b). Fig. 3.9(b) also shows that $(du/dy)_{wall}$ decreases as T_w. Therefore, the increase of wall shear stress along the channel results from the competition between $(du/dy)_{wall}$ and viscosity, which increases as T_w. Knudsen number and slip velocity are shown in Fig. 3.4 and Fig. 3.10, respectively. The increasing trend of Kn and slip along the channel clearly shows that larger Kn and slip may not lead to smaller wall shear stress. Centerline velocity and local centerline Reynolds number,

$$Re_{center} = \frac{\rho_{center} u_{center} H}{\mu_{center}} \tag{3.3}$$

are shown in Fig. 3.11(a) and (b), respectively. The variation of centerline u-velocity agrees with the results by Chen et al. [2]. That is, centerline u-velocity increases as the flow goes downstream for a fixed T_w. It is also shown by Fig. 3.11(a) that centerline velocity decreases as T_w at a fixed streamwise location because of the change of viscosity with T_w. Re_{center}, on the other hand, decreases as the flow goes downstream for a fixed T_w and increases as T_w at a fixed streamwise location. The opposite trend of Re_{center} along the channel compared to u_{center} is caused by the variation of gas properties. At a fixed T_w, density decreases as pressure decreases along the channel and hence reduces Re_{center} even with increased u_{center}. At a fixed streamwise location, with almost unchanged pressure distribution (Fig. 3.7), density decreases as T_w and dynamic viscosity increases as T_w, both of which cause reduced Re_{center} along with reduced u_{center}. Finally, volume and mass flow rates are presented in Fig. 3.12. Fig. 3.12(a) shows that, similar to the u_{center}, volume flow rate decreases as T_w. Fig. 3.12(b) shows that, under the same inlet and outlet pressures, mass flow rate decreases with T_w. Fig. 3.12(b) also presents the mass flow rates of the corresponding cases with $Kn = 0$.

As expected, slip boundary condition results in higher mass flow rate.

3.3.2 Inlet/Outlet Pressure Ratio

In this section, five cases with different inlet/outlet pressure ratios (PR) ranging from 1.340 to 2.701 but the same $T_w/T_0 = 1.2$ are compared. Fig. 3.13 shows Nu in thermal entrance region. Similar to the findings in Fig. 3.2, Nu experiences two drops. Here in Fig.3.13, before its first drop, Nu increases as PR, which can be interpreted by Kn showed in Fig. 3.14 using the same theory as that used to explain Fig. 3.13. That is, higher PR leads to lower Kn, which results in higher Nu when the wall heat flux dominates on Nu. Nu after its second drop is shown in Fig. 3.15. It is found that Nu increases along the channel and decreases as PR. Similar to the explanation of Fig. 3.5, the behavior of Nu can be explained by energy loss within the flow. Using Fig. 3.16, PW/VD is larger for low PR cases and thus leads to higher Nu. Fig. 3.17 shows centerline pressure profile along the channel. It is found that the nonlinearity of centerline pressure profile increases as PR. Knudsen number is shown in Fig. 3.14; Fig. 3.18 and Fig. 3.19 present wall shear stress and slip velocity, respectively; Fig. 3.20 shows centerline u-velocity. Slip velocity, wall shear stress and centerline u-velocity increase as PR and along the channel, while Kn increases along the channel but decreases with PR. Volume and mass flow rates are shown in Fig. 3.21(a) and (b), respectively, where the increase as PR is very obvious.

3.3.3 Comments

Nusselt number (Nu) under isothermal wall boundary condition has been studied by several groups [15, 18, 19]. In the work by Yu and Ameel [15], the flow is assumed to be fully developed, and pressure work (PW) as well as viscous dissipation (VD) are neglected. Yu and Ameel showed that for engineering applications where air is the working gas and wall surface is rough, rarefaction leads to lower Nu compared to continuum model. Their key idea lies on the competition between temperature jump and velocity slip on Nu, the combined effect of which could make Nu either increase or decrease depending on the working gas as well as the wall surface properties. In Chen's

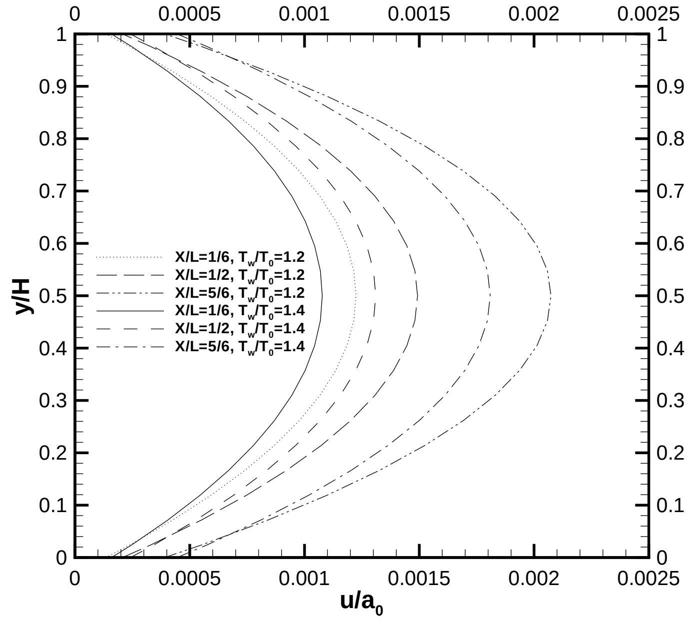

(a)

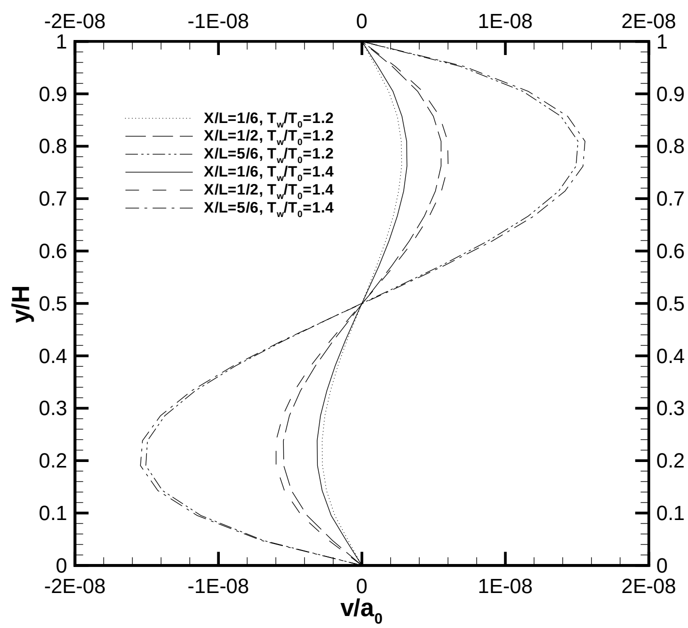

(b)

Figure 3.8: Comparison of velocity profiles at three different streamwise locations between the cases with T_w/T_0 at 1.2 and 1.4, respectively. (a) U-velocity; (b) V-velocity.

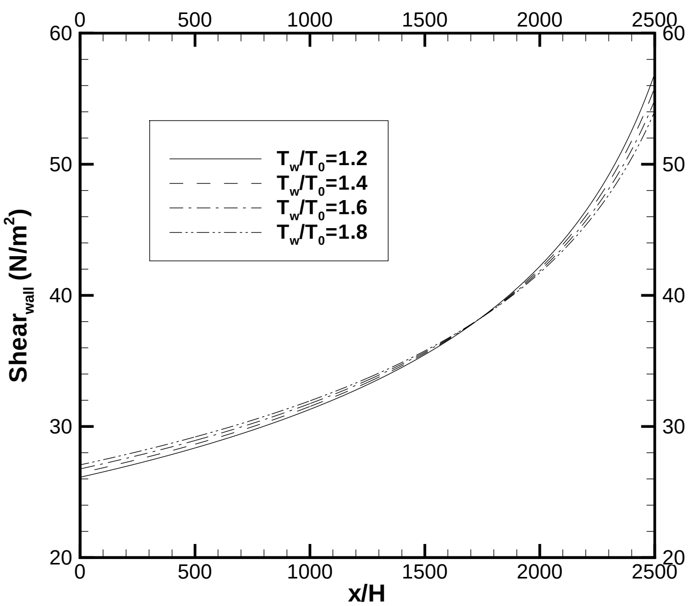

(a)

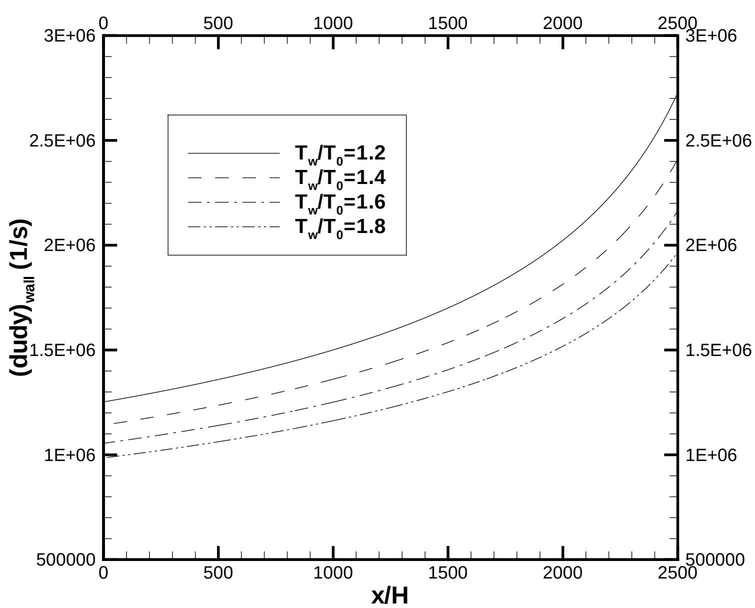

(b)

Figure 3.9: Wall shear stress for the cases with different wall temperatures. (a) Wall shear stress; (b) U-velocity gradient in y-direction.

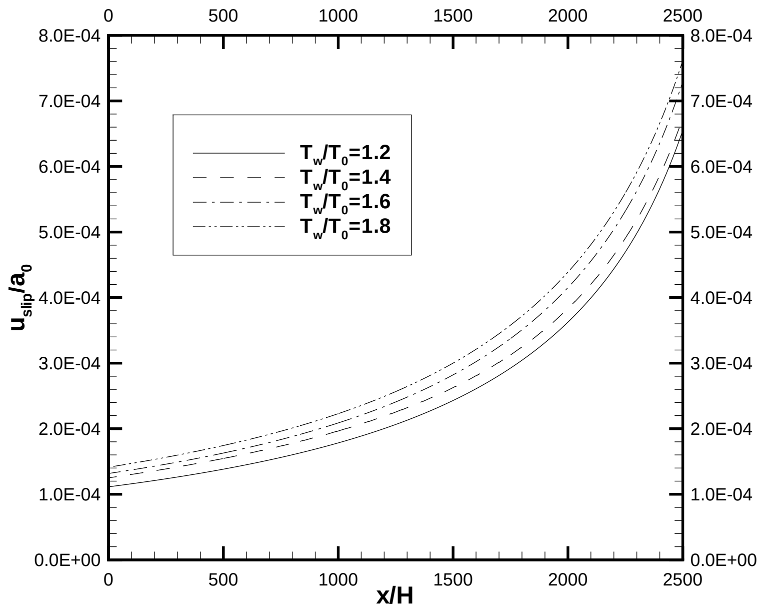

Figure 3.10: Slip velocity for the cases with different wall temperatures.

work [18], VD is considered. Chen [18] showed that VD leads to higher Nu. Instead of the two drops of Nu found in Fig. 3.2, when only VD is considered, Chen [18] showed that Nu first drops to some constant and then increases to another constant. This discrepancy is due to the absence of PW in Chen's model [18]. Jeong and Jeong's study [19] agreed with Chen's work [18] on the role of VD on Nu. As found in Fig. 3.5 and 3.6, when wall heat flux loses its dominance on local Nu, local Nu becomes a function of PW/VD, which is per se a function of Kn as demonstrated by Fig. 3.6 and Fig. 3.9(b). As shown in Fig. 3.8(a) and (b), v-velocity is negligible compared to u-velocity. Also the cross-section pressure gradient is small compared to the streamwise pressure gradient. So most of PW is done near centerline of the channel. On the other hand, VD mainly occurs near the wall. When rarefaction becomes larger, slip velocity leads to the decrease of VD near the wall. Since the inlet and outlet pressures are fixed and pressure gradient is mainly controlled by compressibility, pressure distribution is not changed much. At the same time, rarefaction results in higher velocity near centerline and thus makes PW increase. Therefore, as depicted by Fig. 3.6 and Fig. 3.4, the magnitude of PW/VD increases as Kn. The increasing dominance of PW over VD

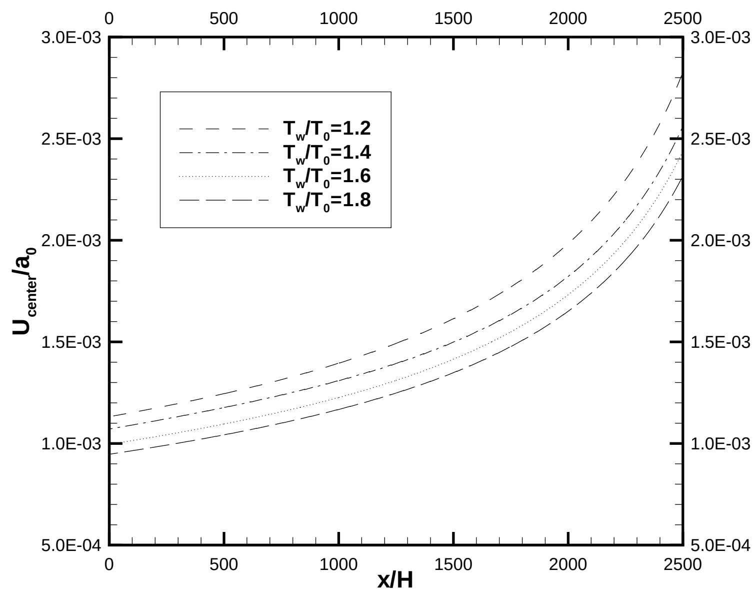

(a)

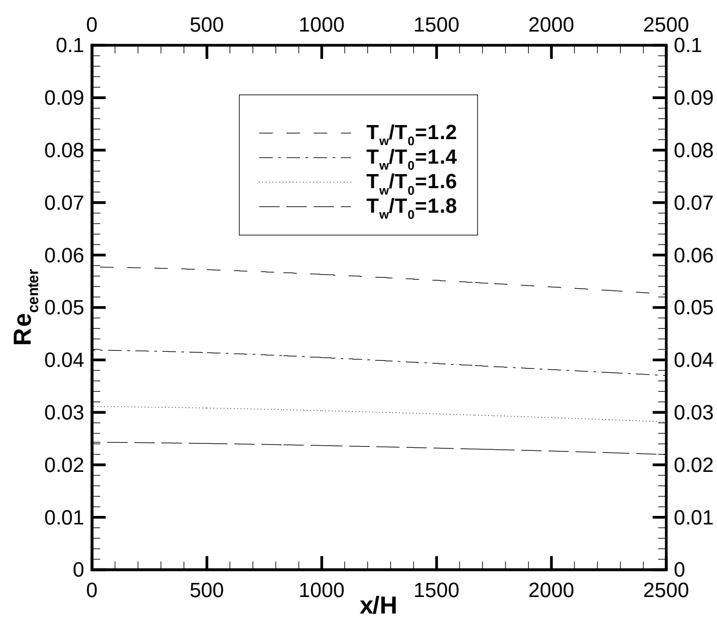

(b)

Figure 3.11: Centerline flow conditions for the cases with different wall temperatures. (a) U-velocity; (b) Reynolds number.

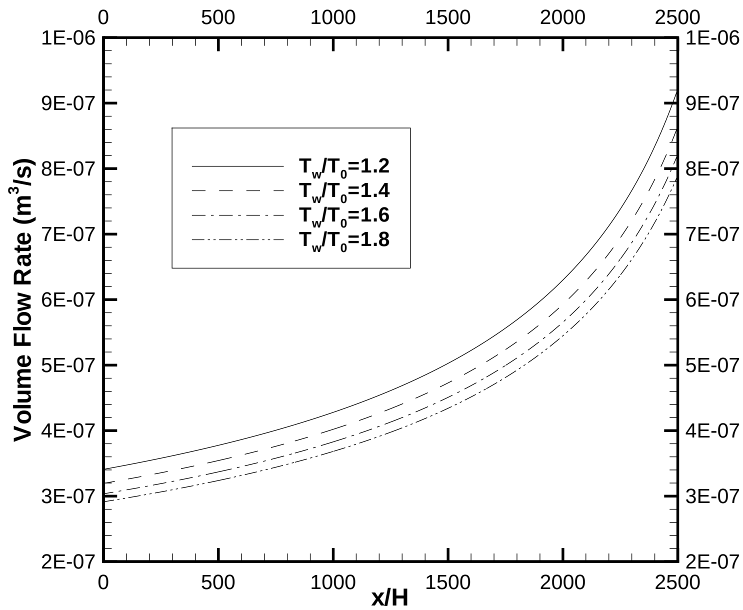

(a)

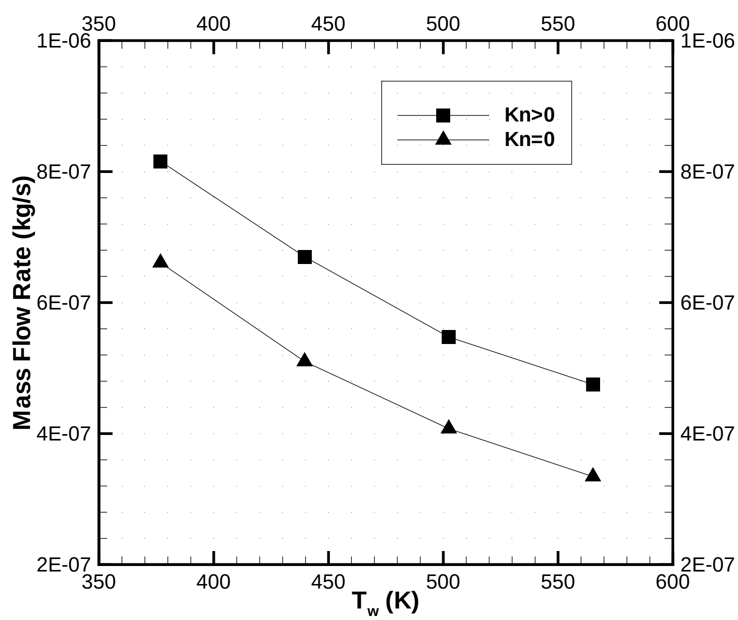

(b)

Figure 3.12: Flow rates for the cases with different wall temperatures. (a) Volume flow rate; (b) Mass flow rate.

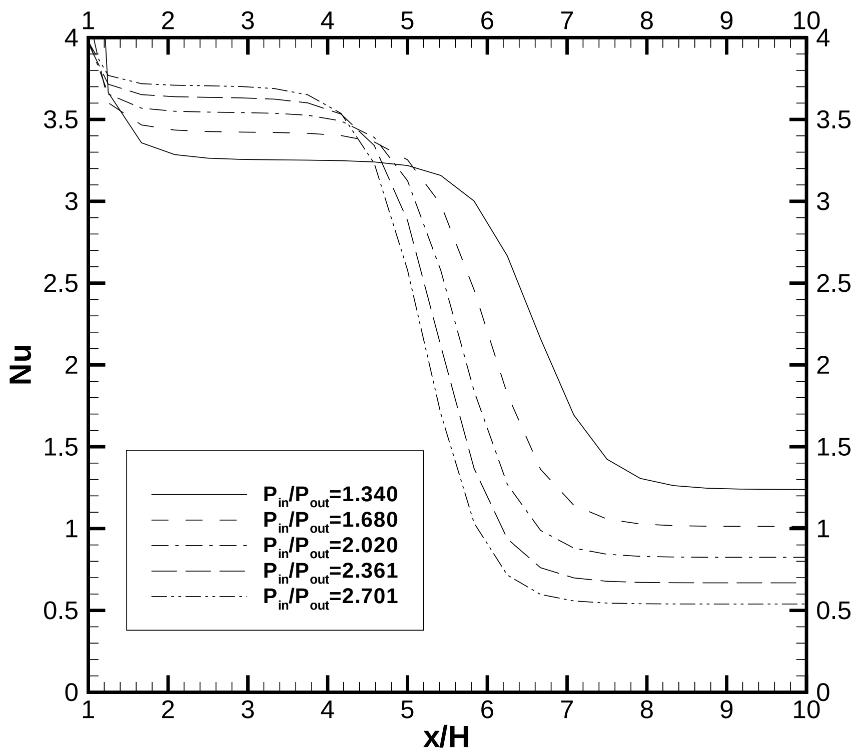

Figure 3.13: Local Nusselt number in thermal entrance region for the cases with different inlet/outlet pressure ratios.

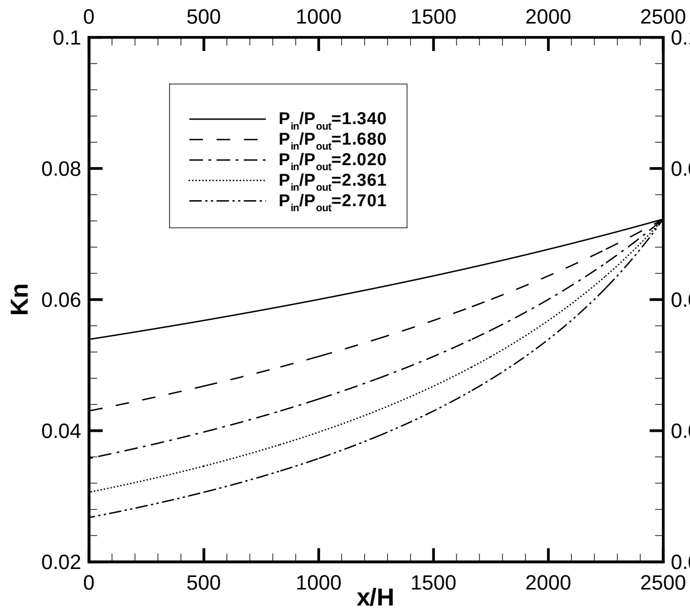

Figure 3.14: Knudsen number for the cases with different inlet/outlet pressure ratios.

then leads to the increase of Nu along the channel. In previous studies on gaseous slip flows with isothermal wall boundary condition, the impact of rarefaction on near-wall mass transport and thermal resistance is investigated very well, while the influence of rarefaction on PW and VD did not draw sufficient attention. Also it is found that for perfect gas, if there is no rarefaction, PW and VD cancel out. To my best knowledge, there is no proof available for this cancelation, which is thus to be further verified in the study on the cases with uniform wall heat flux boundary condition.

3.4 Conclusions

Based on the results presented in section 3.3, for pressure-driven microchannel nitrogen slip flow with isothermal wall boundary condition, some conclusions are made below:

- For long microchannels with very large length-to-height ratios, thermal entrance length is very small. Therefore, on the majority part of the channel, microchannel nitrogen slip flow under isothermal wall boundary condition is almost a pure fluid field problem.

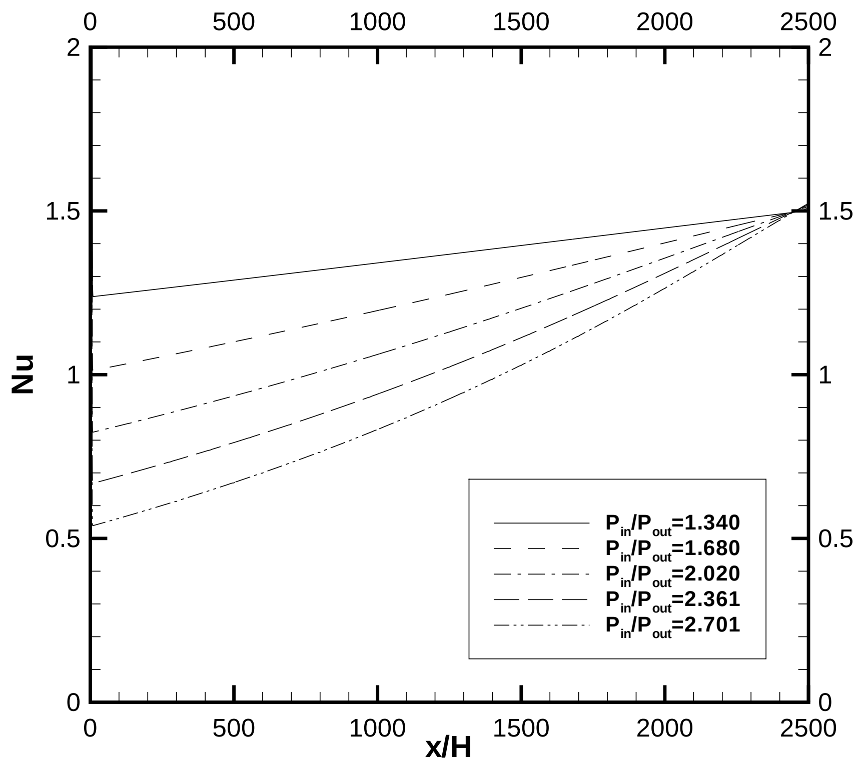

Figure 3.15: Local Nusselt number in thermally developed region for the cases with different inlet/outlet pressure ratios.

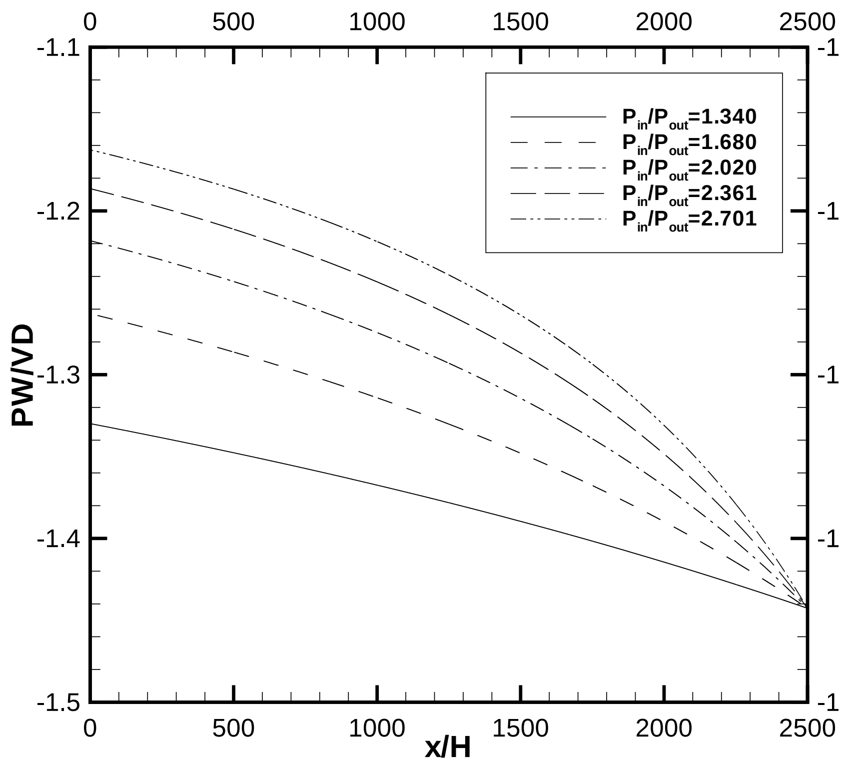

Figure 3.16: Local pressure work over viscous dissipation ratio for the cases with different inlet/outlet pressure ratios.

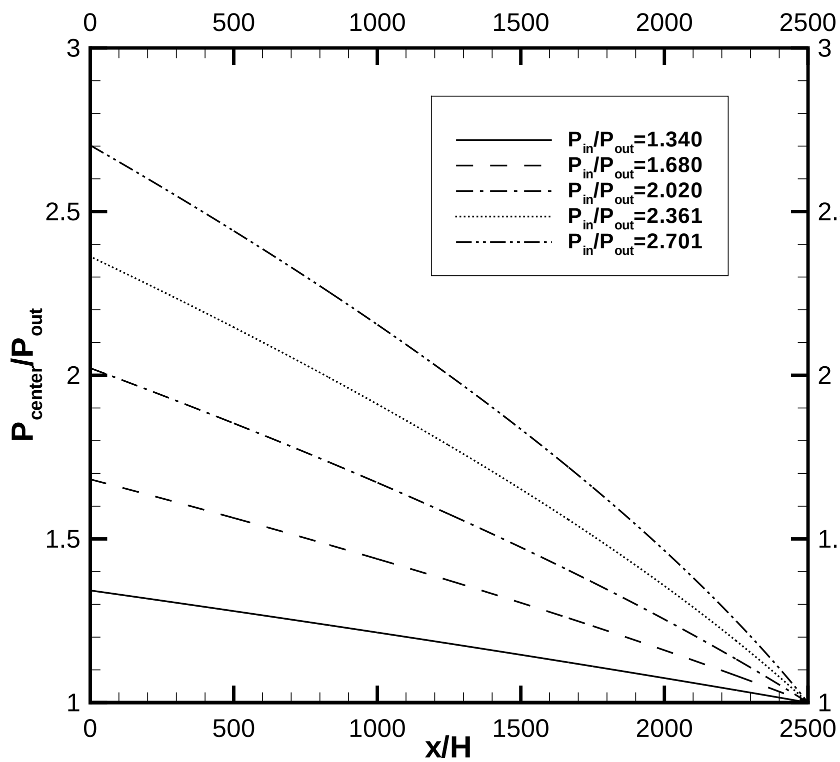

Figure 3.17: Centerline pressure distribution for the cases with different inlet/outlet pressure ratios.

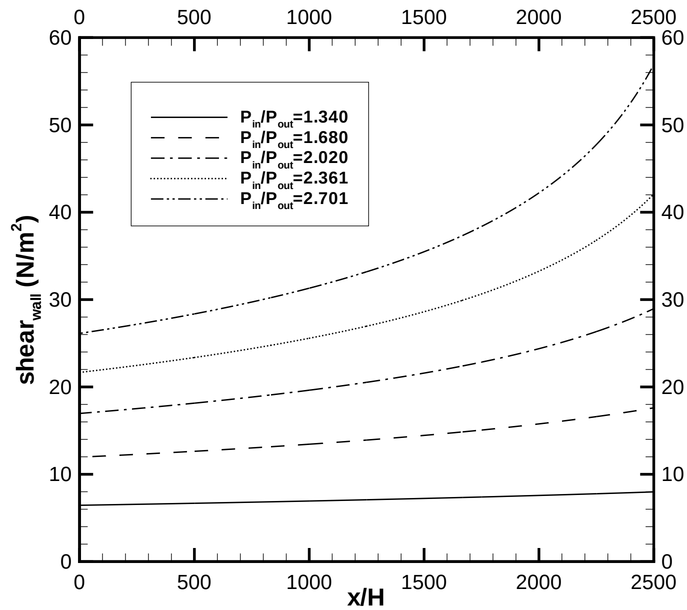

Figure 3.18: Wall shear stress for the cases with different inlet/outlet pressure ratios.

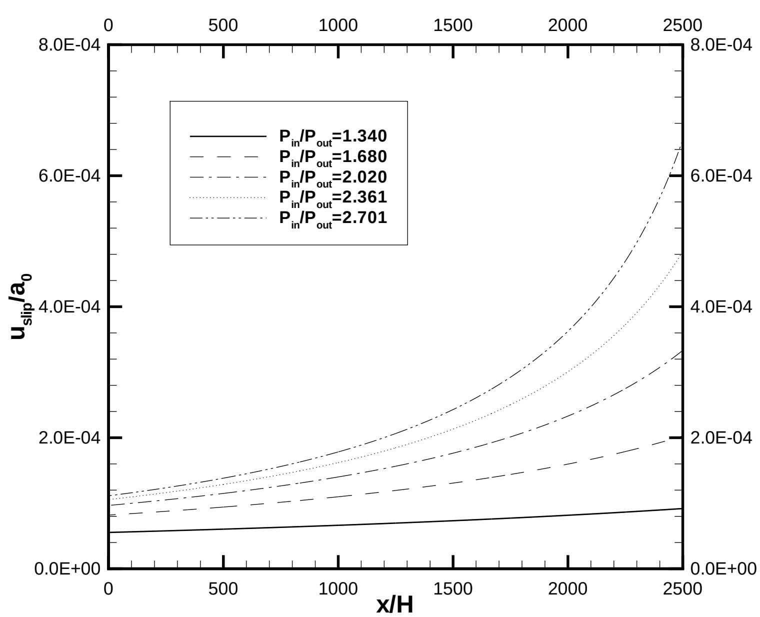

Figure 3.19: Slip velocity for the cases with different inlet/outlet pressure ratios.

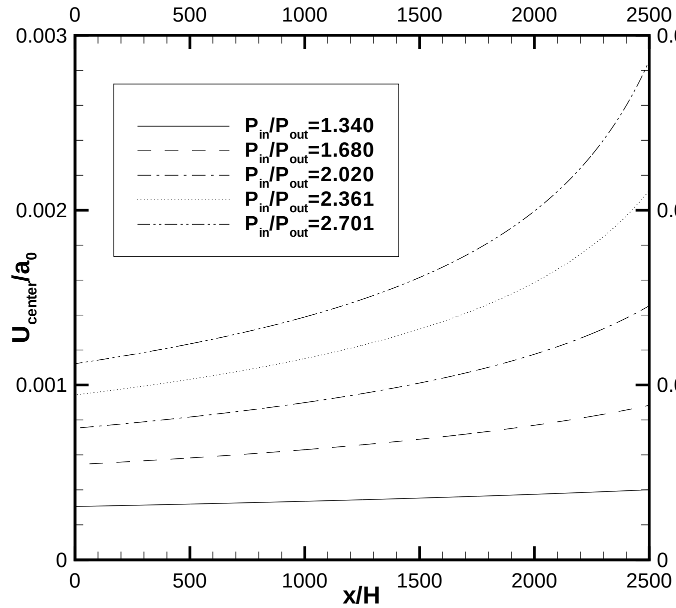

Figure 3.20: Centerline U-velocity for the cases with different inlet/outlet pressure ratios.

- Rarefaction influences Nusselt number in different ways along the channel. Nusselt number drops twice in thermal entrance region. During the first drop, thermal field is developing and wall heat flux is dominant over the energy loss within gas flows on Nusselt number. So the increased thermal resistance due to temperature jump plays the main role on Nusselt number before the second drop. Therefore, before the second drop, rarefaction leads to lower Nusselt number. After the second drop, thermal field is developed and the energy loss within gas flows, which is a function of Knudsen number, becomes dominant on Nusselt number. Specifically, Nusselt number increases as the magnitude of pressure work over viscous dissipation ratio, which increases as Knudsen number. Therefore, after the second drop, rarefaction leads to larger Nusselt number.

- Pressure work to viscous dissipation ratio is a function of the degree of rarefaction. Rarefaction reduces viscous dissipation near the wall as well as increases pressure work near centerline, and thus makes pressure work dominant over viscous dissipation for perfect gases.

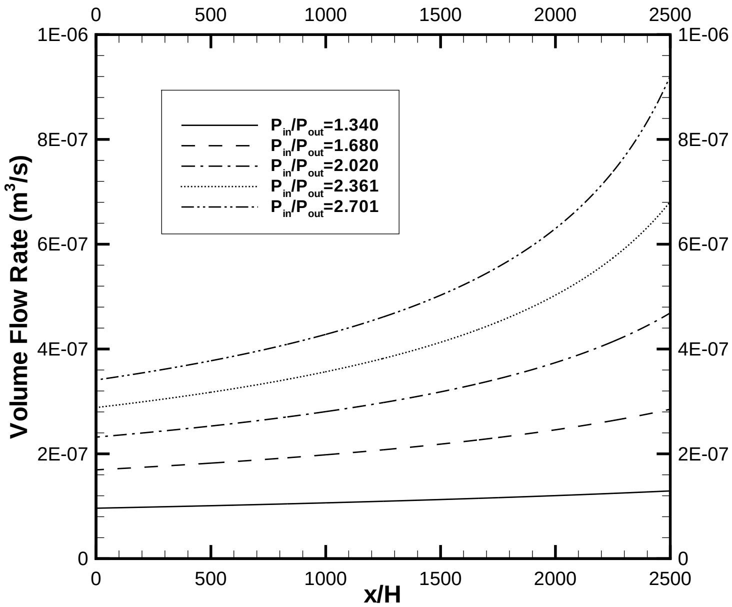

(a)

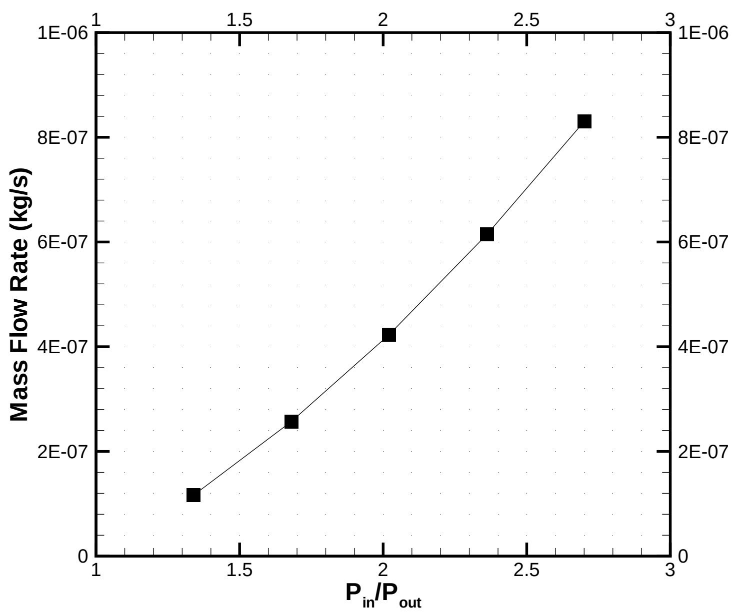

(b)

Figure 3.21: Flow rates for the cases with different inlet/outlet pressure ratios. (a) Volume flow rate; (b) Mass flow rate.

- There is no fully developed fluid field; for different wall temperatures with inlet and outlet pressures fixed, the difference on pressure distribution is negligible; both volume and mass flow rates decrease with wall temperature and increase as inlet/outlet pressure difference.

Chapter 4

Two Dimensional Steady-State Pressure-Driven Nitrogen Flow in Long Microchannels Under Uniform Heat Flux Wall Boundary Condition

4.1 Introduction

Analytical solutions of fully-developed slip-flow heat transfer with uniform heat flux wall boundary condition in microtubes were given by Sparrow et al. [12] in as early as 1962. With slip boundary conditions, Sparrow et al. [12] found that fully-developed Nusselt number decreased with Knudsen number. Instead of using slip boundary conditions to model laminar microscale fully developed flow, in their analytical study, Li et al. [14] proposed the 'wall-adjacent layer', where the change of gas thermal conductivity results in significant influence on heat transfer and is able to make accurate qualitative predictions. Laminar fully-developed slip-flow forced convection in rectangular microchannels with isoflux wall boundary condition was investigated analytically by Yu and Ameel [16]. They discussed the effects of velocity slip and temperature jump on Nusselt number and showed that, compared to no-slip flow condition, heat transfer could be either reduced or enhanced. Tunc and Bayazitoglu [17] conducted an analytical study on convective heat transfer in a rectangular microchannel, where the flow is assumed to be thermally and hydrodynamically fully-developed. In their paper, the variation of Nu with Kn as well as the channel aspect ratio are presented and discussed. As one of the very recent attempts, Jeong and Jeong [19] analytically studied microchannel hydrodynamically developed gas flow with uniform heat flux wall boundary condition, where rarefaction, streamwise conduction and viscous dissipation are all included.

The analytical studies mentioned above revealed the physics of microchannel gas flow in a very neat and indicative manner. However, due to the limitations of analytical methods, the physical pictures presented in [12, 14, 16, 17, 19] are under some strong assumptions, including fully developed fluid field, constant gas properties, negligible compressibility and so on. Unfortunately, for pressure-driven gas flows, such assumptions are rarely valid. For example, it has been shown numerically by Guo and Wu [21] and in Chapter 3 that hydrodynamically fully developed pressure-driven microchannel gas flows do not arise due to compressibility. Therefore, a lot of researchers employ experimental and/or numerical methods to study microchannel pressure-driven gas flows. In the early 1990s, several groups of experimentalists reported the discrepancy between microchannel slip flows and continuum theory [7, 8, 9, 10]. It is these early experimental findings that motivated many people to study microchannel gaseous slip flows. Arkilic et al. [13] studied pressure-driven helium flow in a long microchannel both analytically and experimentally. It was found that by taking velocity slip and compressibility into account, 2D Navier-Stokes equation could fairly accurately predict mass flow rate. Beskok et al. [20] presented their numerical simulations, where rarefaction, compressibility, viscous dissipation as well as thermal creep were considered. They discussed the competing effects of compressibility and rarefaction on the non-linear pressure distribution of gas flows within long microchannels, which interpreted the experimental findings by Pong et al. [9]. Guo and Wu [21] numerically studied the compressibility effect on gas flow and heat transfer in a microtube, where rarefaction was not considered. They concluded that fully developed pressure-driven gas flow does not exist due to compressibility. It was also shown by Guo and Wu [21] that, because of the large dependence of thermal field on flow field, for microchannel gas flows with non-negligible Mach number, fully developed thermal field does not arise. To reproduce the experimental results by Pong et al. [9], Chen et al. [18] conducted 2D numerical simulations, where slip flows in rectangular microchannels were modeled as compressible with rarefaction and viscous dissipation. Recently, Raju and Roy [23] numerically studied supersonic microchannel flows and compared their results with published direct-simulation Monte Carlo results. As an extension of Chapter 2 and Chapter 3, this chapter concentrates on uniform wall heat flux boundary condition for a long microchannel with 500:1 length-to-height ratio. The organization is as follows: section 4.2 briefs the numerical model; section 4.3 presents the numerical results with discussions; finally, conclusions are given in section 4.4.

4.2 Numerical Model Description

The readers can refer to Chapter 2 for mathematical model and numerical procedure. In this chapter, nitrogen gas flows with uniform heat flux wall boundary condition are investigated. Variable properties, rarefaction (velocity slip, thermal creep and temperature jump), compressibility and viscous dissipation are all included. The employed computational method is based on the SIMPLER algorithm and has both a serial and a parallel version. The parallel solver is built with the domain decomposition method (DDM). As we did before, parallel solver is first employed and runs until some convergence criteria are reached. Then to eliminate the singularity caused by the DDM, the results from parallel solver are fed to serial solver, which then runs until the desired convergence is achieved. To get steady state solution, time marching method is used. The convergence criteria for parallel solver are of the form

$$\varepsilon = \max \left\{ \begin{array}{ll} \text{if } \xi^n \neq 0 & \frac{|\xi^{n+1}-\xi^n|}{|\xi^n|} \\ \text{if } \xi^n = 0 & |\xi^{n+1}| \end{array} \right\} \tag{4.1}$$

where ξ applies to streamwise velocity u, temperature T as well as the variables in the overlapping regions of the subdomains and the superscripts denote the time step. The convergence criteria for serial solver take the same form as for parallel solver, while ξ only applies to streamwise velocity u and temperature T. The computation for all cases involved in this chapter stopped when ε falls below 1×10^{-12} for the final serial run. In this chapter, the channel to be studied is the Channel #2 given in Fig. 2.1 and Table 2.1 in Chapter 2. Using the grid dependence test results presented in Table 2.2 of Chapter 2, the grid size 2300×29 (X×Y) is selected.

4.3 Results and Comments

All the cases involved in this chapter are on the Channel #2 that is described by Fig. 2.1 and Table 2.1 in Chapter 2, and using nitrogen as the working gas. In section 4.3.1, the results of the cases with different wall heat fluxes are presented and analyzed. Then in section 4.3.2, rarefaction is turned off by setting Knudsen number to zero, and the results are compared with those in section 4.3.1. Section 4.3.3 focuses on the influence of inlet/outlet pressure ratio. Finally, some comments are given in section 4.3.4.

4.3.1 Wall Heat Flux

For the five cases involved in this section, the pressure ratio, $PR = P_{out}/P_{in}$, is fixed at 2.0, while the dimensionless wall heat flux $\bar{q}_w = \frac{q_w H}{T_0 k_0}$ ranges from 5×10^{-5} to 2.5×10^{-4}. Fig. 4.1 shows a typical velocity profile of the case with $\bar{q}_w = 5 \times 10^{-5}$, where Fig. 4.1(a) and (b) shows u- and v-velocity profiles at three streamwise locations, respectively. Fig. 4.2 shows the temperature profile at $x/H = 400$. From Fig. 4.1(a) and (b), we found that, compared to u-velocity, v-velocity is negligible. Based on Fig. 4.2, temperature gradient on a single cross-section of the microchannel is very small, i.e., centerline temperature can very well represent bulk temperature.

Centerline pressure profile is shown in Fig. 4.3, from which it is found that the tilting from linear profile becomes greater as wall heat flux increases. This increased departure from linearity for centerline pressure profile as wall heat flux goes up, is mainly caused by the increased thermal expansion accompanying temperature rise. In Fig. 4.4, it is found that bulk temperature increases along the channel, however, its profile is nonlinear and lower than linear profile.

Flow conditions along the centerline of microchannel are described in Fig. 4.5. From centerline streamwise velocity in Fig. 4.5(a), the acceleration due to compressibility is obvious. Fig. 4.5(b) shows centerline Reynolds number, from which we can find that flows are within laminar regime and Reynolds number decreases along the microchannel. In addition, from Fig. 4.5(b), it is clear that with the same PR, Reynolds number decreases as wall heat flux. The decrease of Reynolds number with wall heat flux can

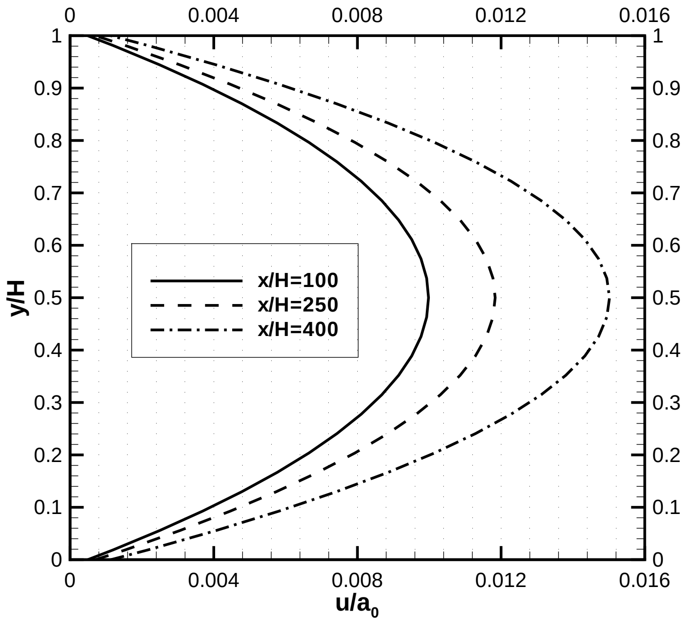

(a)

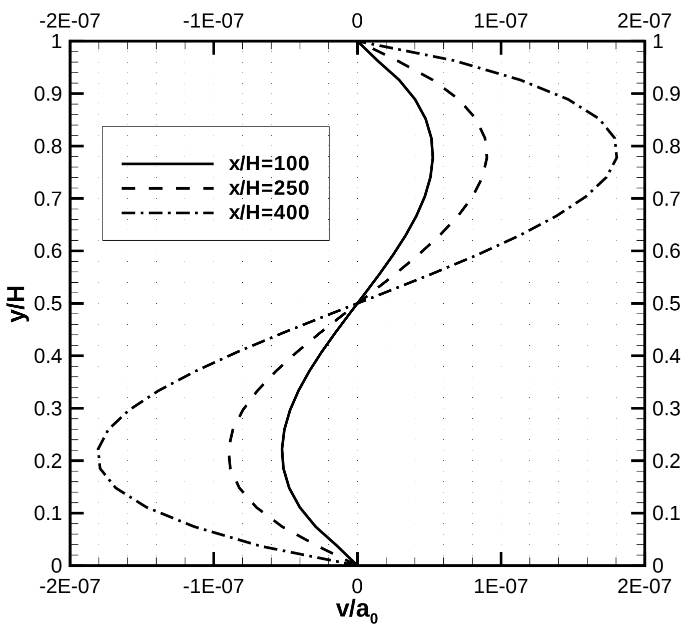

(b)

Figure 4.1: Velocity profile at the channel cross-sections of the case with $\bar{q}_w = 5 \times 10^{-5}$ and $PR = P_{out}/P_{in} = 2.0$. (a) U-velocity profile at three streamwise locations; (b) V-velocity profile at three streamwise locations.

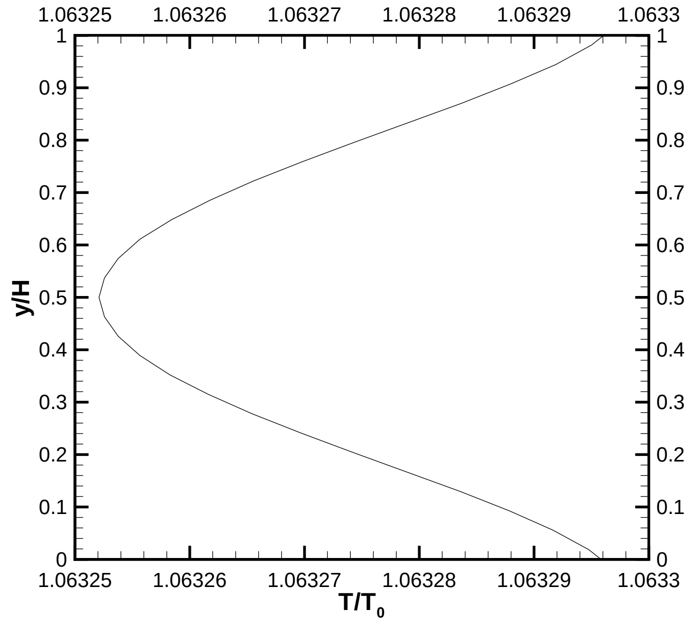

Figure 4.2: Temperature profile at the channel cross-section $x/H = 400$ of the case with $\bar{q}_w = 5 \times 10^{-5}$ and $PR = P_{out}/P_{in} = 2.0$.

be explained by the reduced density and centerline velocity, as well as the increased viscosity.

Fig. 4.6 and Fig. 4.7 describe the flow condition close to channel wall. Fig. 4.6(a) shows that Kn increases along the microchannel and as wall heat flux. The increase of Kn along the channel is due to the drop of pressure and gas density as well as the increase of viscosity caused by the rise of temperature. The increase of Kn with wall heat flux can be explained by the lower density and larger viscosity due to higher temperature. Slip velocity is shown in Fig. 4.6(b). For all five cases with different wall heat fluxes, slip velocity increases along the microchannel, which is consistent with the trend of Kn shown in Fig. 4.6(a). However, slip velocity does not always increase as wall heat flux. There is a turnaround point around $x/H = 200$, before which slip velocity decreases as wall heat flux while increases as wall heat flux thereafter. This is because velocity slip is a function of not only Kn but also velocity gradient at the wall. As an interpretation of Fig. 4.6(b), Fig. 4.7(b) clearly shows that, closer to inlet, the difference on velocity gradient at the wall between the lower and higher heat flux

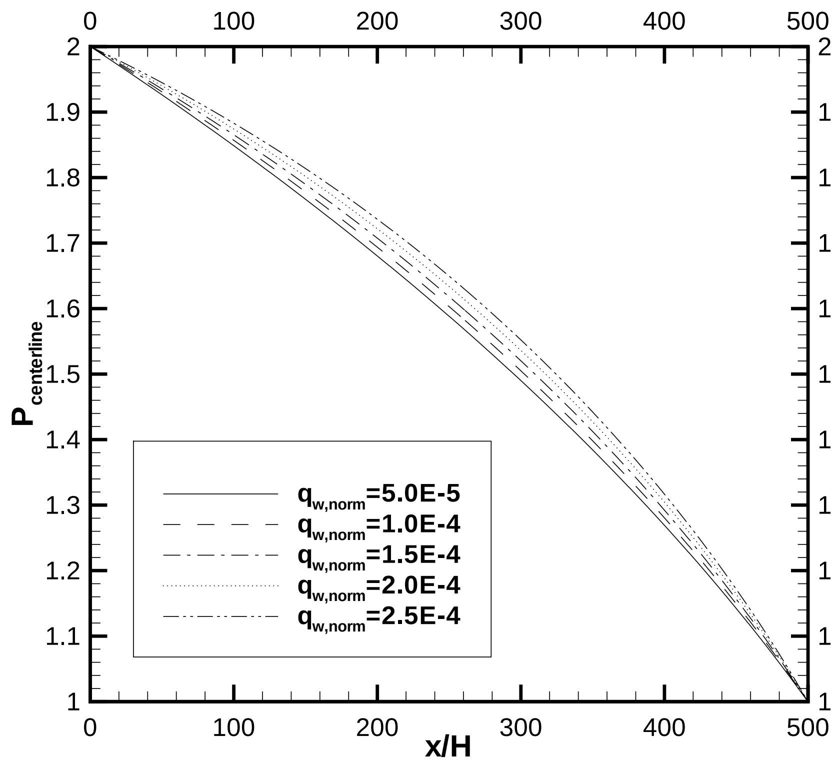

Figure 4.3: Centerline pressure distribution for the cases with $PR = P_{out}/P_{in} = 2.0$ and $\bar{q}_w$ ($q_{w,norm}$ in figure) ranging from 5×10^{-5} to 2.5×10^{-4}.

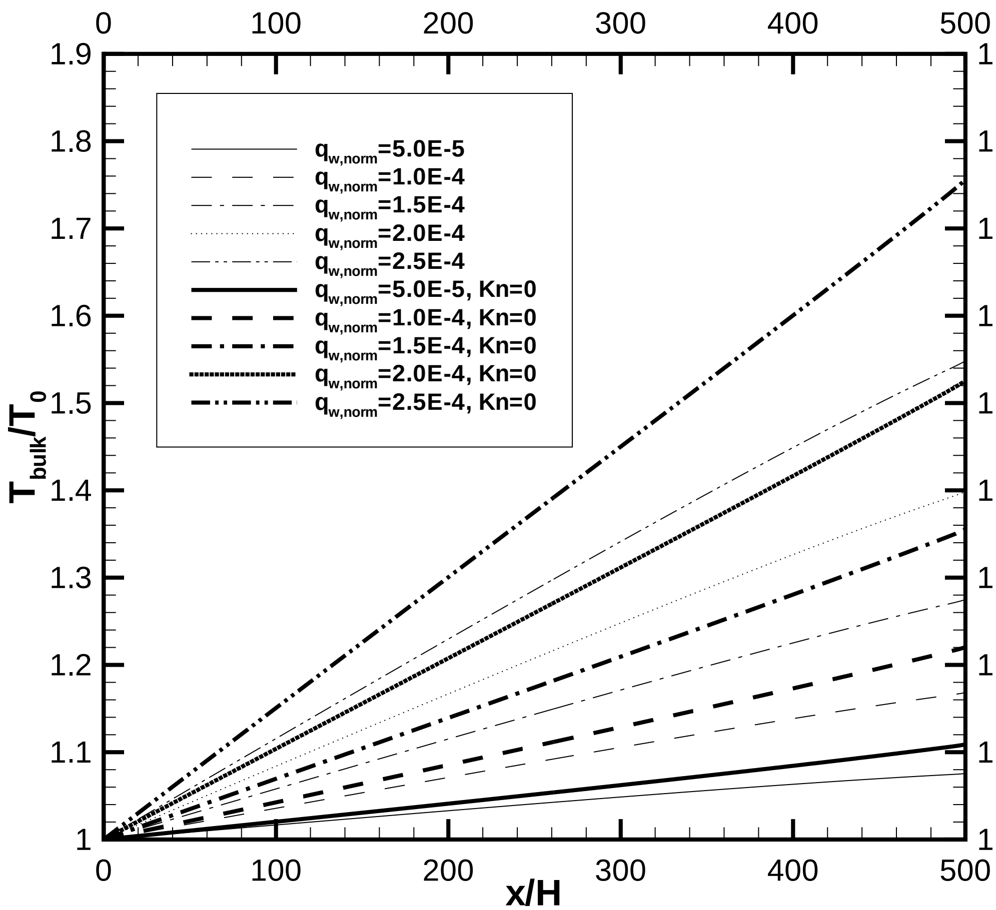

Figure 4.4: Bulk temperature distribution for the cases with $PR = P_{out}/P_{in} = 2.0$ and $\bar{q}_w$ ($q_{w,norm}$ in figure) ranging from 5×10^{-5} to 2.5×10^{-4}.

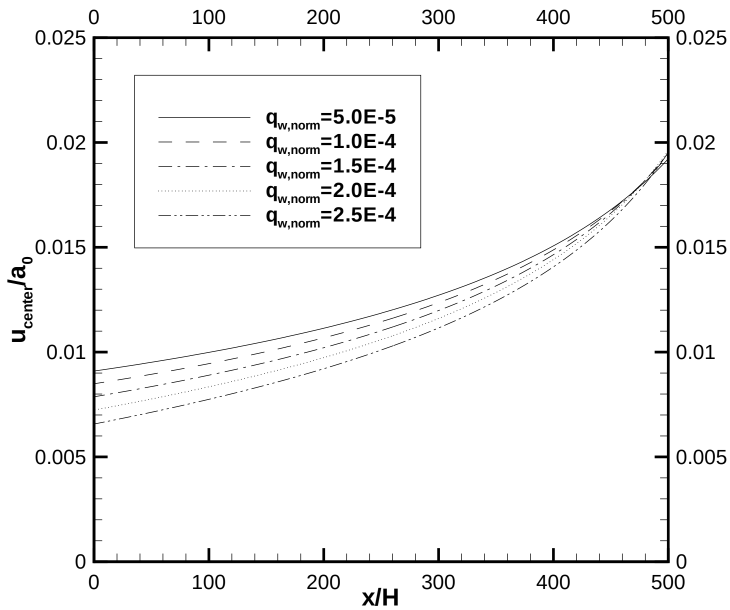

(a)

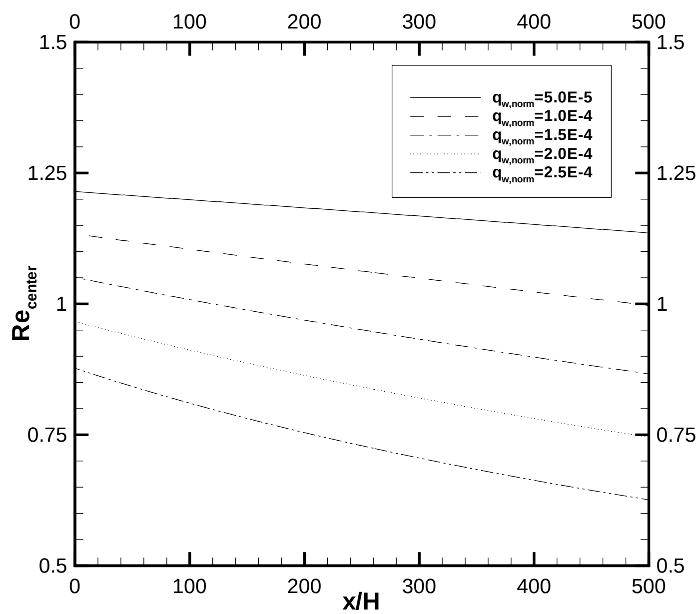

(b)

Figure 4.5: Centerline flow condition for the cases with $PR = P_{out}/P_{in} = 2.0$ and $\bar{q}_w$ ($q_{w,norm}$ in figure) ranging from 5×10^{-5} to 2.5×10^{-4}. (a) U-velocity; (b) Reynolds number.

cases is greater than the difference in far downstream region. Fig. 4.7(a) tells us that although both Kn and velocity slip increase along the channel, wall shear stress always increases along the channel. To understand this fact, first from Fig. 4.7(b), we find that velocity gradient at the wall increases along the channel. In addition, viscosity also increases along the wall due to the rise of gas temperature. Fig. 4.7(a) also shows a turnaround point around $x/H = 250$, before which wall shear stress decreases as wall heat flux while increases as wall heat flux thereafter. Similar to velocity slip, the behavior of wall shear stress can be explained by Fig. 4.7(b) together with the increase of viscosity as wall heat flux.

So far we have got the pictures at a single cross-section, along the centerline, and along the channel wall. We understand most of them but the nonlinear bulk temperature profile along the channel. There are two source terms in energy equation: pressure work and viscous dissipation, which could cause the tilting of bulk temperature profile. Another factor could be the rise of specific heat due to the increase of temperature. For the largest heat flux case ($\bar{q}_w = 2.5 \times 10^{-4}$), the change of specific heat along the channel is within 4%. Our analysis shows that the variation of specific heat is far from enough to cause the big tilting of bulk temperature profile. That is, pressure work and viscous dissipation are the main cause of the nonlinear behavior of bulk temperature. To demonstrate this point, the ratio of pressure work over viscous dissipation, PW/VD, along the microchannel is plotted in Fig. 4.8. It is clear that the magnitude of pressure work is more than that of viscous dissipation. This draining of energy from the flow leads to the nonlinear bulk temperature profile. From Fig. 4.8, it is found that the magnitude of PW/VD increases as wall heat flux and increases along the microchannel.

Besides outlet temperature, mass flow rate is another main concern. Fig. 4.9(a) and (b) plotted volume and the mass flow rates, respectively. Fig. 4.9(a) is very consistent with Fig. 4.5(a). Fig. 4.9(b) tells us that mass flow rate decreases as wall heat flux, which means in Fig. 4.7(a), the overall shear is greater for higher wall heat flux cases. From Fig. 4.9(b), it is obvious that the higher outlet temperatures achieved by higher wall heat flux cases are not only due to feeding more energy, but also because of the

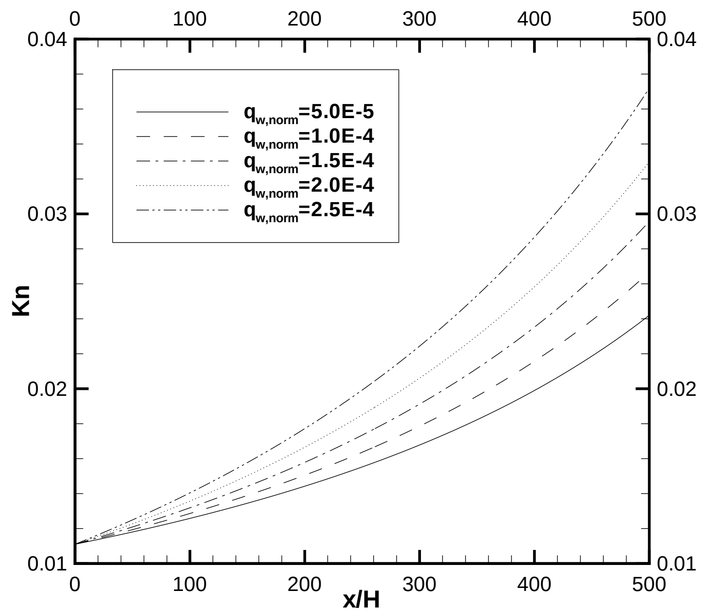

(a)

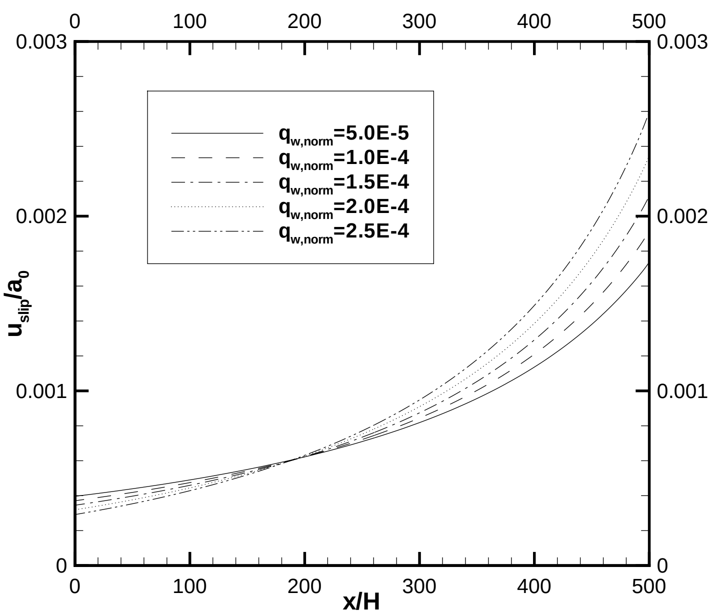

(b)

Figure 4.6: Knudsen number and slip velocity for the cases with $PR = P_{out}/P_{in} = 2.0$ and $\bar{q}_w$ ($q_{w,norm}$ in figure) ranging from 5×10^{-5} to 2.5×10^{-4}. (a) Knudsen number; (b) Slip velocity.

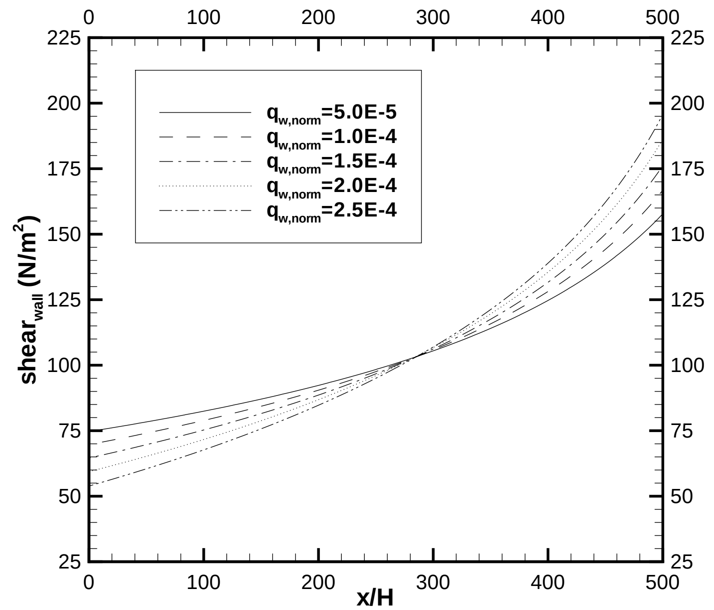

(a)

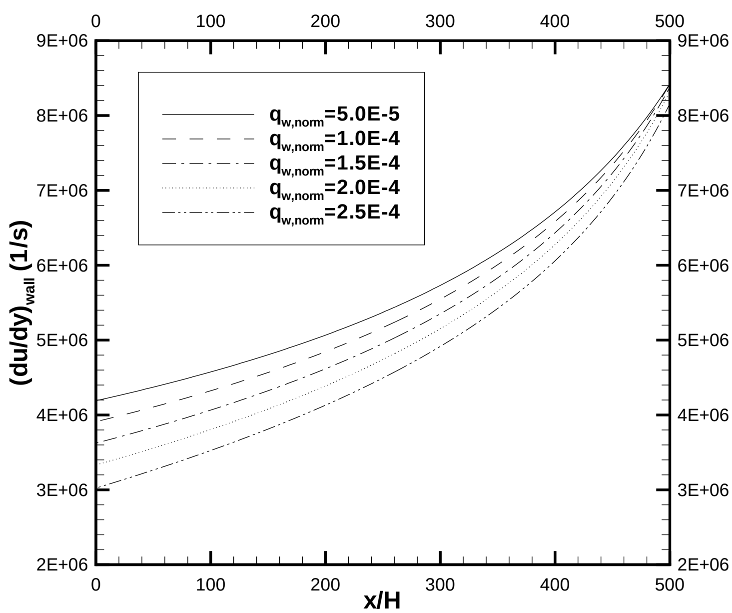

(b)

Figure 4.7: Wall shear stress for the cases with $PR = P_{out}/P_{in} = 2.0$ and $\bar{q}_w$ ($q_{w,norm}$ in figure) ranging from 5×10^{-5} to 2.5×10^{-4}. (a) Wall shear stress; (b) Velocity gradient at the wall.

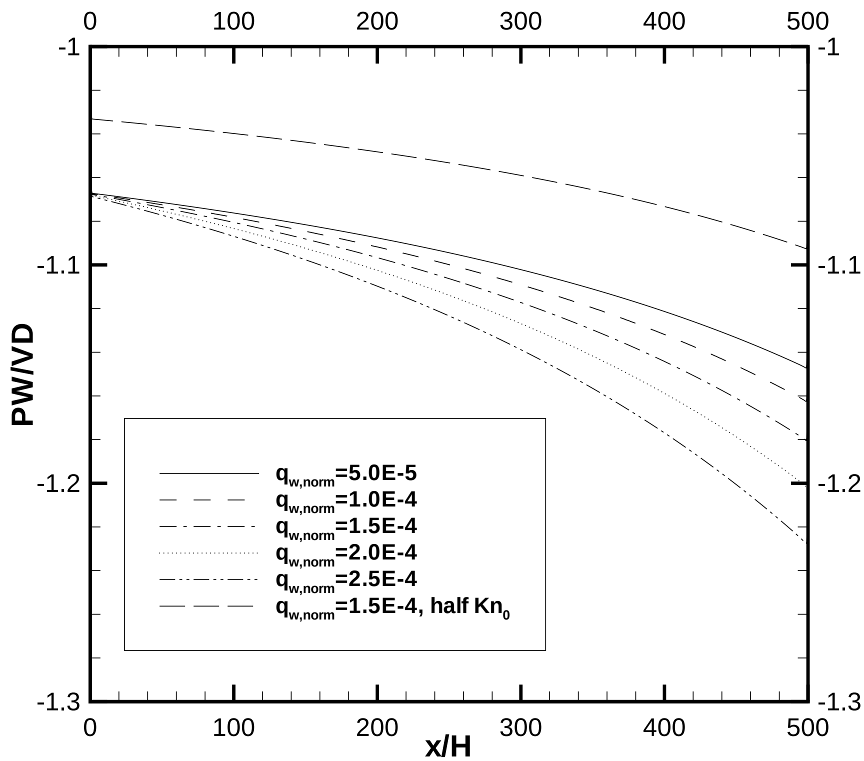

Figure 4.8: Local pressure work over viscous dissipation ratio for the cases with $PR = P_{out}/P_{in} = 2.0$ and $\bar{q}_w$ ($q_{w,norm}$ in figure) ranging from 5×10^{-5} to 2.5×10^{-4}.

reduced mass transport ability. The Nusselt number,

$$Nu = \frac{q_w H}{k(T_w - T_{bulk})} \tag{4.2}$$

is plotted in Fig. 4.9, which shows that Nu decreases along the channel for all five cases. Additionally, the Nu's of higher wall heat flux cases are higher than those of lower wall heat flux cases. During the calculation of Nu, wall temperature, T_w, is calculated by the temperature jump boundary condition,

$$T_g - T_w = \frac{2 - \sigma_T}{\sigma_T} \left(\frac{2\gamma}{1 + \gamma} \right) \frac{\lambda}{\mathrm{Pr}} \left(\frac{\partial T}{\partial n} \right)_w \tag{4.3}$$

where the thermal accommodation coefficient $\sigma_T = 1$, i.e., rough wall surface.

4.3.2 Rarefaction Effects

In this section, for the five cases studied in section 4.3.1, rarefaction is turned off by setting Knudsen number to zero, and the results without rarefaction are compared with those with rarefaction. When rarefaction is excluded from the model, the first anticipated change is the lower volume (Fig. 4.9 (a)) and mass flow rates (Fig. 4.9 (b)). Compared to the strongly nonlinear bulk temperature profile of the cases with rarefaction, Fig. 4.4 shows that the bulk temperature profiles for the corresponding cases without rarefaction are almost linear. In Chapter 3, pressure work (PW) over viscous dissipation (VD) ratio, PW/VD, has been shown to be minus unity when rarefaction is turned off. The same phenomena are observed here. To understand it, first, from energy equation, the pressure source term has a coefficient βT, which is unity under the perfect gas assumption. The coefficient βT is much less than unity for most liquid, which can explain why viscous dissipation is dominant over pressure work in most liquid flows. Secondly, in current model, the unique violation against continuum theory is the discontinuous boundary conditions at wall, which is characterized by Knudsen number. Once Kn is set to zero, the model will comply with continuum theory. For the cases studied in section 4.3.1, Kn is nonzero and increases along the channel, in the meanwhile PW/VD departs from the minus unity further and further along the channel. The results in Chapter 3 show the same trend. Definitely, some connection

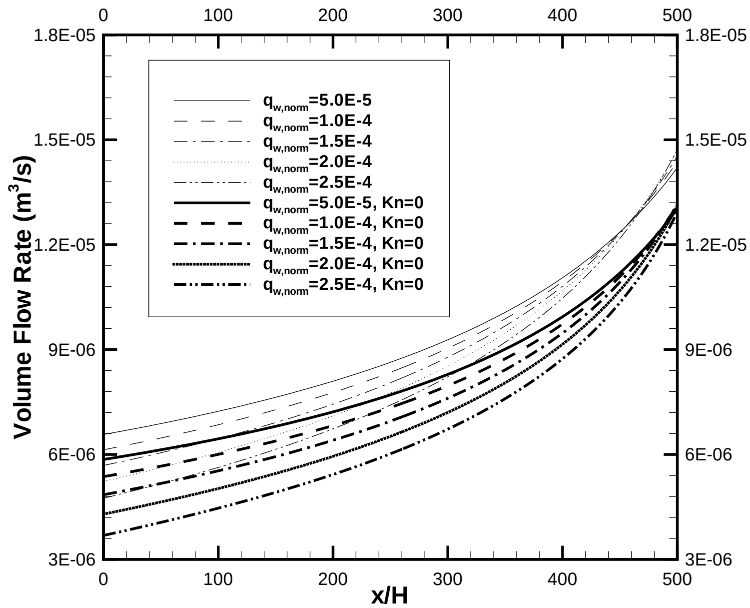

(a)

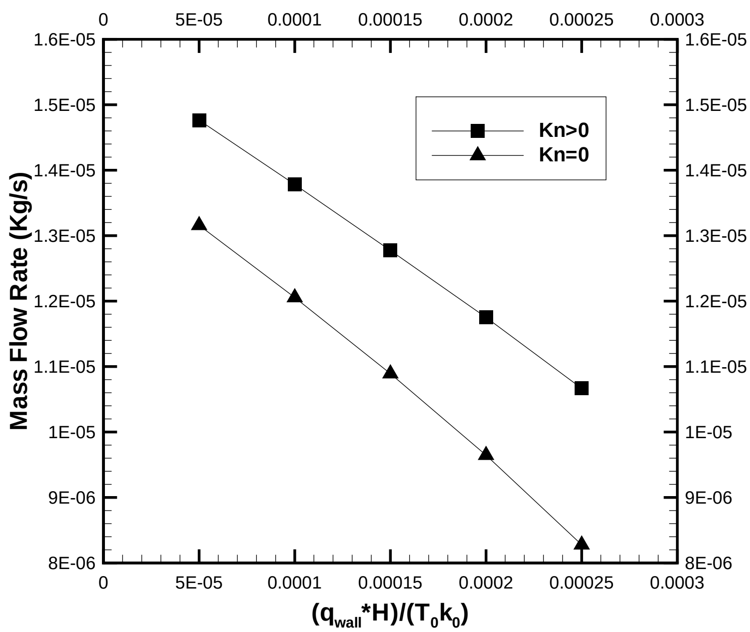

(b)

Figure 4.9: The influence of rarefaction on flow rates for the cases with $PR = P_{out}/P_{in} = 2.0$ and $\bar{q}_w$ ($q_{w,norm}$ in figure) ranging from 5×10^{-5} to 2.5×10^{-4}. (a) Volume flow rate; (b) Mass flow rate.

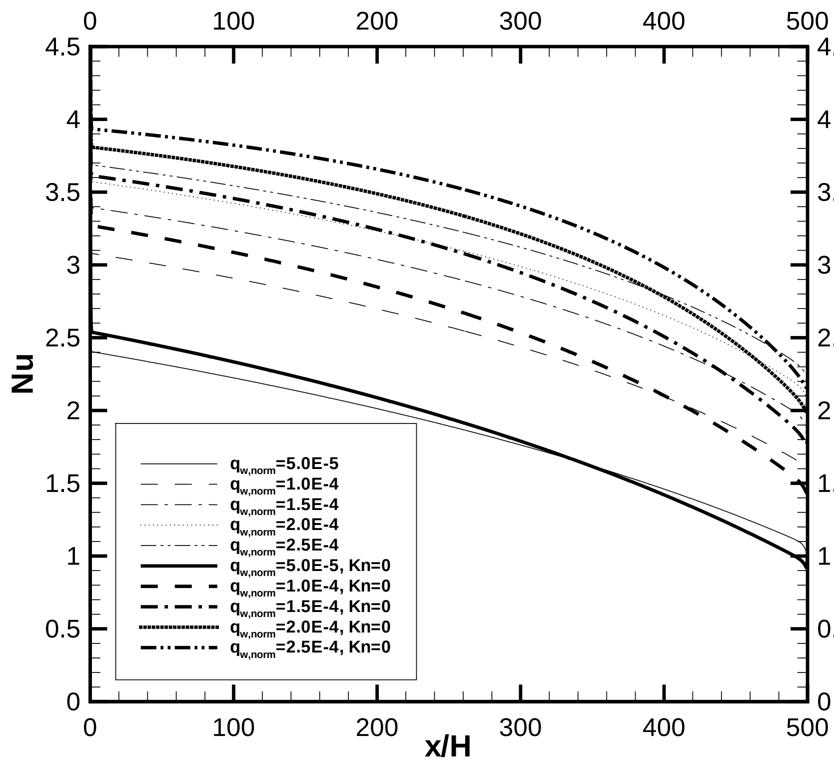

Figure 4.10: The influence of rarefaction on local Nusselt number for the cases with $PR = P_{out}/P_{in} = 2.0$ and $\bar{q}_w$ ($q_{w,norm}$ in figure) ranging from 5×10^{-5} to 2.5×10^{-4}.

exists between the magnitude of PW/VD and Kn. Rarefaction reduces viscous dissipation close to the wall and increases pressure work near the centerline, which finally leads to the increase of the magnitude of PW/VD. For perfect gases, this connection can be summarized as: the magnitude of PW/VD increases with Kn and is equal to unity when Kn is zero. To further verify this trend, a test case is done, where the inlet Knudsen number, Kn_0, is manually set to one half of the actual value for the case with $\bar{q}_w = 1.5 \times 10^{-4}$. Fig. 4.8 shows that the resulting PW/VD curve falls between the minus unity line and the curve with the actual value of Kn_0. Apart from the linear bulk temperature profile, Fig. 4.4 also shows that, if rarefaction is neglected, outlet temperature will be overestimated, which can be explained by the change of PW/VD and the reduced mass flow rate.

As for Nu, according to Fig. 4.10, the influence of rarefaction on Nu is inconsistent along the channel. There is a turnaround point close to outlet. Before this turnaround point, rarefaction results in lower Nu, while leads to larger Nu thereafter. Fig. 4.10 shows that this turnaround point moves closer to outlet as wall heat flux increases. In general, for the wall heat fluxes tried in this chapter, rarefaction gives lower overall Nu. To understand the findings in Fig. 4.10, two mechanisms must be considered. First, rarefaction influences Nu through wall heat flux. That is, there is a competition between velocity slip and temperature jump on Nu. Velocity slip promotes mass and hence energy transport at the wall, while temperature jump increases thermal resistance at the wall. For the case with nitrogen and rough wall surface, temperature jump is always dominant over velocity slip in this competition. Therefore, in the first mechanism, rarefaction leads to lower Nu. The second mechanism by which rarefaction influences Nu is through the source terms in energy equation. Specifically, velocity slip reduces VD near the wall while promotes PW near the centerline. It has been learned from the discussion in Chapter 3 that, the magnitude of PW/VD increases as rarefaction and Nu increases as the magnitude of PW/VD. Therefore, in the second mechanism, rarefaction results in larger Nu. For the case with uniform wall heat flux boundary condition, these two mechanisms concurrently exist along the channel. Therefore, the inconsistency of the influence of rarefaction on Nu found in Fig. 4.10 is the combined effects of these two mechanisms. Specifically, before the turnaround point, the first mechanism is dominant, while the second mechanism becomes dominant thereafter.

4.3.3 Inlet/Outlet Pressure Ratio

To improve convective heat transfer, the most intuitive way is to increase Reynolds number, specifically inlet/outlet pressure ratio ($PR = P_{in}/P_{out}$) for pressure driven flows with outlet pressure fixed. Fig. 4.11, Fig. 4.12, and Fig. 4.13 compare the results of five cases with the same wall heat flux $\bar{q}_w = 1 \times 10^{-4}$ but different inlet/outlet pressure ratios ranging from 1.5 to 3.5. Fig. 4.11 shows that bulk temperature increases along the channel except for the case with $PR = 3.5$, which is shown separately in a small window within the same figure. Fig. 4.12 shows that the magnitude of pressure work over viscous dissipation ratio decreases with inlet/outlet pressure ratio. This seems to be unable to result in the trend found in Fig. 4.11, where for larger pressure ratios, bulk temperature profile departs more from linear distribution. The only reasonable explanation for the bulk temperature profile of the case with $PR = 3.5$ is, the magnitudes of viscous dissipation and pressure work increase with PR. Fig. 4.13(a) shows that Nusselt number decreases as inlet/outlet pressure ratio. Based on the definition of Nusselt number, it is clear that $q_w H$ is the same for all cases in Fig. 4.13(a) and thermal conductivity k rises with temperature, which will lead to the increase of Nusselt number as inlet/outlet pressure ratio. To produce the trend shown in Fig. 4.13(a), temperature difference $T_w - T_{bulk}$ must increases as inlet/outlet pressure ratio, as shown in Fig. 4.13(b). From Fig. 4.13(b), one may find that $T_w - T_{bulk}$ increases along the channel for all cases except the case with $PR = 1.5$, as shown separately in a small window within the same figure. Finally, Fig. 4.14 shows the mass flow rate, where the expected increase with PR is obvious. In summary, the increase of PR can significantly promote mass transport and hence benefit microchannel cooling, as depicted by Fig. 4.14 and Fig. 4.11, respectively.

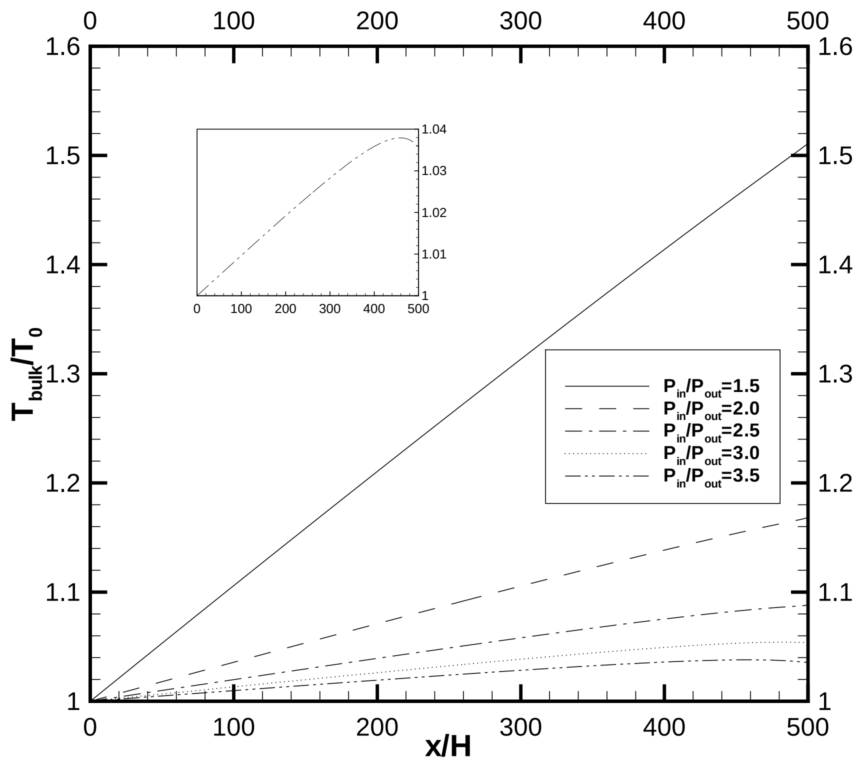

Figure 4.11: The influence of inlet/outlet pressure ratio on the bulk temperature.

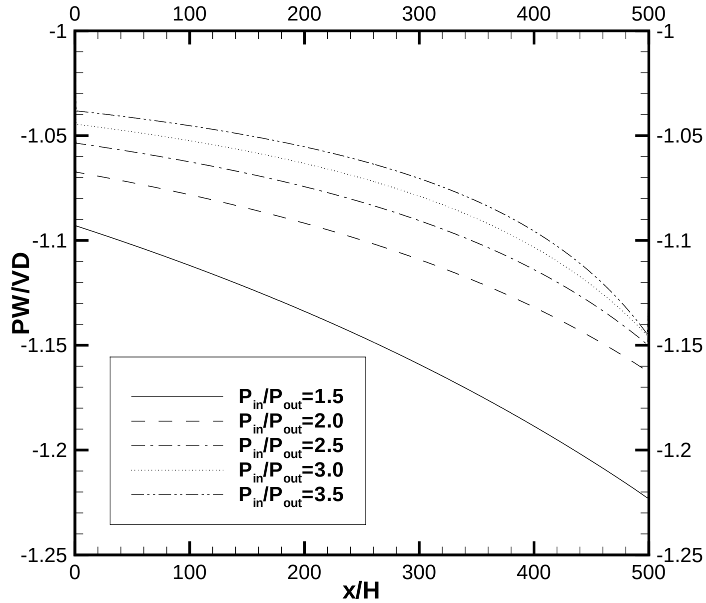

Figure 4.12: The influence of inlet/outlet pressure ratio on the ratio of pressure work over viscous dissipation.

4.3.4 Comments

Based on the results obtained, for pressure driven nitrogen slip flows, the draining of energy due to compressibility acceleration improves the cooling effect. This effect is normally ignored in the analytical studies [12, 14, 16, 17, 19]. In most analytical studies [12, 16, 17, 19], the influence of rarefaction on convective heat transfer is summarized as the competition between velocity slip and temperature jump, and has been showed to reduce the convective efficiency for most engineering gas media. Here the authors showed that this is probably not true in practice (Fig. 4.10). In fact, for strongly coupled factors, one can never isolate some factors and analyze their effects separately. For example, as shown in Fig. 4.8 and Fig. 4.9(b), not only can rarefaction alter mass and hence energy transport as well as the thermal resistance close to the wall, but also the source terms in energy equation, and thus make the influence of rarefaction on Nu inconsistent along the microchannel (Fig. 4.10). It has been demonstrated in section 4.3.3 that, the larger the inlet/outlet pressure ratio, the better the cooling effect is. Due to the easily expected increase of mass flow rate, this is not surprising at all. However,

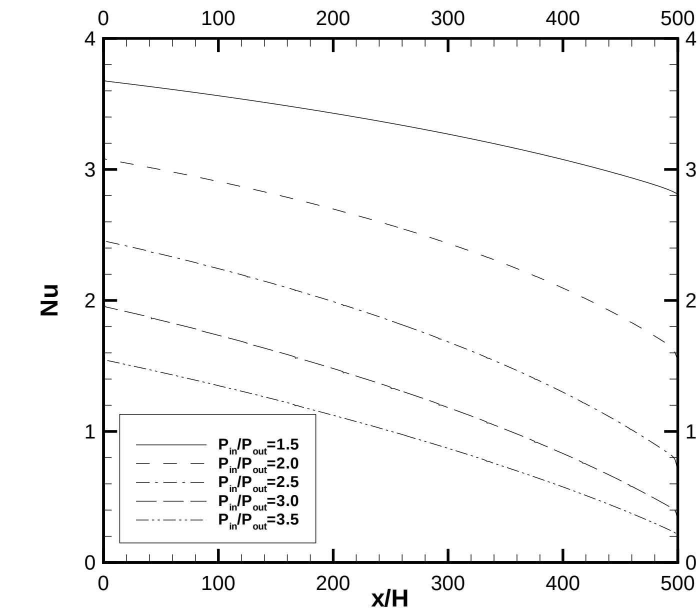

(a)

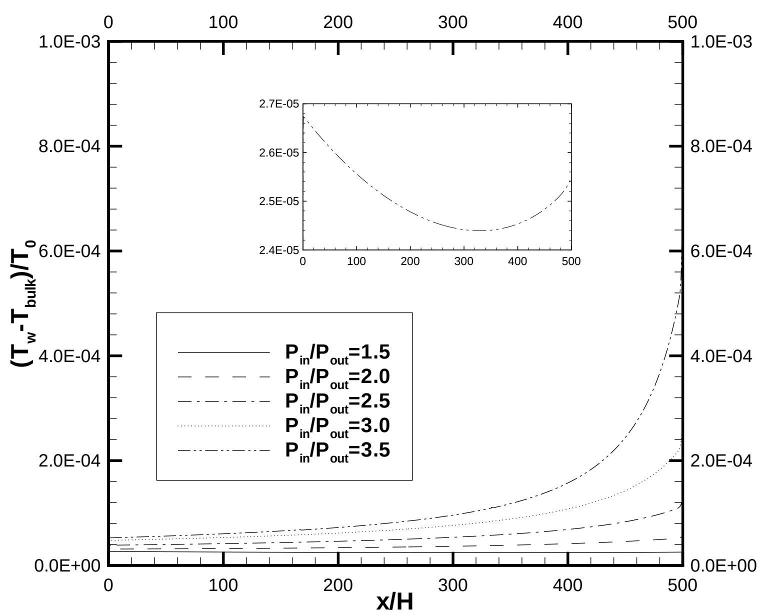

(b)

Figure 4.13: The influence of inlet/outlet pressure ratio on (a) Nusselt number; (b) The difference between wall and bulk temperature;

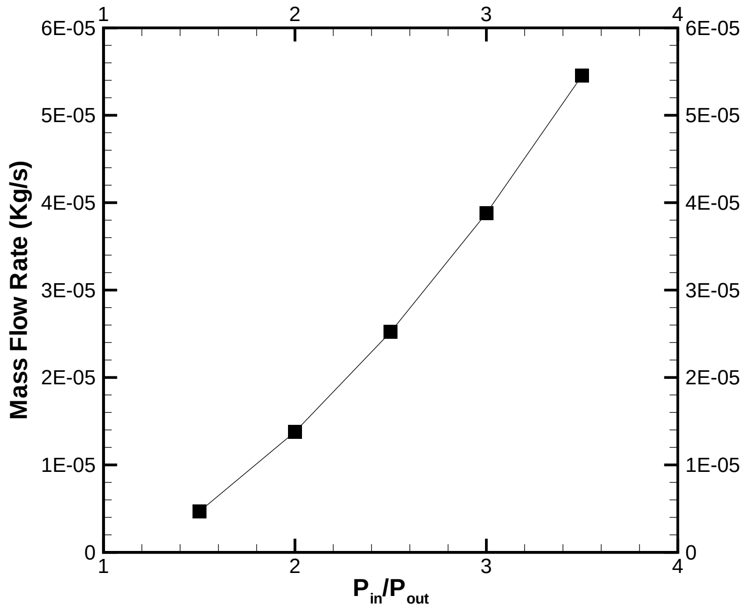

Figure 4.14: The influence of inlet/outlet pressure ratio on mass flow rate.

as inlet/outlet pressure ratio increases, some unusual phenomena, such as the decrease of bulk temperature close to outlet (Fig. 4.11), may happen.

4.4 Conclusions

Based on the results and analysis in section 4.3, several conclusions are made below for microchannel pressure-driven gas flows under uniform heat flux wall boundary condition:

- Both bulk temperature profile and centerline pressure profile along the microchannel are nonlinear. The former is mainly caused by the combined effects of pressure work and viscous dissipation, while the latter is due to compressibility.

- The ratio of pressure work over viscous dissipation, PW/VD, is a function of Knudsen number. Under the perfect gas assumption, the magnitude of PW/VD increases with Knudsen number and is equal to unity when Knudsen number is zero.

- The influence of rarefaction on Nusselt number is inconsistent along the microchannel. Rarefaction reduces Nusselt number near inlet, while promotes Nusselt number near outlet.

- The increase of inlet/outlet pressure ratio can significantly promote mass transport and hence benefit microchannel cooling.

Chapter 5

Two Dimensional Steady-State Pressure-Driven Nitrogen Flow in Larger-Dimension Microchannels Under Uniform Heat Flux Wall Boundary Condition

5.1 Introduction

This chapter is a continuation of Chapter 4. As detailed in section 4.1, microscale fluid and thermal phenomena have been studied by a lot of groups with a variety of tools. Besides the microchannels with characteristic dimensions below 10 microns, such as the channels studied in Chapter 2-4, microchannels with characteristic dimensions between 10 and 100 microns are also widely used in industry. Compared to smaller-dimension microchannels, for microchannels of larger dimension, the most expectable change is the reduced rarefaction. An important question to answer is whether continuum model is capable of giving good enough prediction on thermal and fluid fields for microchannels of larger dimension. One of the most important design parameters is inlet/outlet pressure difference. It is clear that as the channel size decreases, inlet/outlet pressure difference increases dramatically to achieve comparable Reynolds numbers. The variation of inlet/outlet pressure difference versus channel size needs to be found either numerically or experimentally. In this chapter, two microchannels (Table 5.1) with characteristic dimensions of 20μm and 50μm, respectively, will be studied. The schematic of the two microchannels listed in Table 5.1 is the same as that in Fig. 2.1. Nitrogen is still the working gas. The organization of this chapter is as follows: section 5.2 briefs the numerical model; section 5.3 and 5.4 present the numerical results with discussions for the two larger-dimension microchannels, respectively; finally, conclusions are given in section 5.5.

Table 5.1: Parameters of larger-dimension microchannel nitrogen flows.

Parameter	Channel#3	Channel#4
Length L	2000μm	2000μm
Height H	20μm	50μm
Pressure Ratio $PR = P_{in}/P_{out}$	1.01, 1.02, 1.03	1.001, 1.002, 1.003
Inlet Temperature T_0	300K	300K
Density of Nitrogen at Inlet Temperature and $1 \times 10^5 Pa$ ρ_0	1.1233 kg/m^3	1.1233 kg/m^3
Outlet Pressure P_{out}	$1 \times 10^5 Pa$	$1 \times 10^5 Pa$
Inlet Dynamic Viscosity μ_0	1.782 $\times 10^{-5}$ N $\cdot$ s/m^2	1.782 $\times 10^{-5}$ N $\cdot$ s/m^2
Inlet Thermal Conductivity k_0	2.59 $\times 10^{-2}$ W/(K·m)	2.59 $\times 10^{-2}$ W/(K·m)
Inlet Sound Speed a_0	353.07m/s	353.07m/s
Inlet Specific Heat c_p	1041 J/(kg·K)	1041 J/(kg·K)
Specific Gas Constant R	296.8 J/(kg·K)	296.8 J/(kg·K)
Specific Heat Ratio γ	1.4	1.4

5.2 Numerical Model Description

The readers can refer to Chapter 2 for mathematical model and numerical procedure. In this chapter, nitrogen slip flow with uniform heat flux wall boundary condition is investigated. Variable properties, rarefaction (velocity slip, thermal creep and temperature jump), compressibility and viscous dissipation are all included. The employed computational method is based on the SIMPLER algorithm and has both a serial and a parallel version. The parallel solver is built with the domain decomposition method (DDM). As we did before, parallel solver is first employed and runs until some convergence criteria are reached. Then to eliminate the singularity caused by the DDM, the results from parallel solver are fed to serial solver, which then runs until the desired convergence is achieved. To get steady state solution, time marching method is used. The convergence criteria for parallel solver are of the form

$$\varepsilon = \max \left\{ \begin{array}{ll} \text{if } \xi^n \neq 0 & \frac{|\xi^{n+1}-\xi^n|}{|\xi^n|} \\ \text{if } \xi^n = 0 & |\xi^{n+1}| \end{array} \right\} \tag{5.1}$$

where ξ applies to streamwise velocity u, temperature T as well as the variables in the overlapping regions of adjacent subdomains and the superscripts denote the time step. The convergence criteria for serial solver take the same form as for parallel solver, while ξ only applies to streamwise velocity u and temperature T. For Channel #3, a 500×29 (X×Y) grid is employed. Parallel scheme is employed for Channel #3. The computation for all the cases associated with Channel #3 stopped when ε falls below 1×10^{-12} for the final serial run. For Channel #4, a 200×29 (X×Y) grid is employed. Serial solver is employed for Channel #4. The computation for all the cases associated with Channel #4 stopped when ε falls below 1×10^{-12}.

5.3 Channel #3 with Characteristic Dimension of 20 μm

All the cases involved in this section are on Channel #3 that is described by Fig. 2.1 and Table 5.1, and using nitrogen as the working gas. The channel height H is 20 μm. In section 5.3.1, the results of the cases with different wall heat fluxes are presented and analyzed. Then in section 5.3.2, rarefaction is turned off by setting Knudsen number to zero, and the results are compared with those in section 5.3.1. Section 5.3.3 focuses on the influence of inlet/outlet pressure ratio.

5.3.1 Wall Heat Flux

For the three cases involved in this section, the inlet/outlet pressure ratio, $PR = P_{out}/P_{in}$, is fixed at 1.03, while the dimensionless wall heat flux $\bar{q}_w = \frac{q_w H}{T_0 k_0}$ ranges from 1×10^{-3} to 3×10^{-3}. Fig. 5.1 shows a typical velocity profile of the case with $\bar{q}_w = 1 \times 10^{-3}$, where Fig. 5.1(a) and (b) present u- and v-velocity profiles at three streamwise locations, respectively. From Fig. 5.1(a) and (b), we found that, compared to u-velocity, v-velocity is negligible. Fig. 5.2 shows the temperature profile at $x/H = 50$.

Centerline pressure profile is shown in Fig. 5.3, from which it is found that the tilting from linear profile becomes greater as wall heat flux increases. This increased departure from linearity for centerline pressure profile as wall heat flux goes up, is mainly caused by the increased thermal expansion accompanying temperature rise. In Fig. 5.4, it is found that bulk temperature increases along the channel, however, its profile is nonlinear and lower than linear profile.

Flow conditions along the microchannel centerline are described in Fig. 5.5. From the centerline velocity in Fig. 5.5(a), the acceleration due to compressibility is obvious. Fig. 5.5(b) shows centerline Reynolds number, from which we can find that flows are within laminar regime and Reynolds number decreases along the microchannel. In addition, from Fig. 5.5(b), it is clear that with the same PR, Reynolds number decreases as wall heat flux. The decrease of Reynolds number with wall heat flux can be explained by the reduced density and centerline velocity, as well as the increased viscosity.

Fig. 5.6 and Fig. 5.7 describe the flow conditions close to the channel wall. Fig. 5.6(a) shows that Kn increases along the microchannel and as wall heat flux. The increase of Kn along the channel is due to the drop of pressure and gas density as well as the increase of viscosity caused by temperature rise. The increase of Kn with the wall heat flux can be explained by the lower density and higher viscosity due to higher

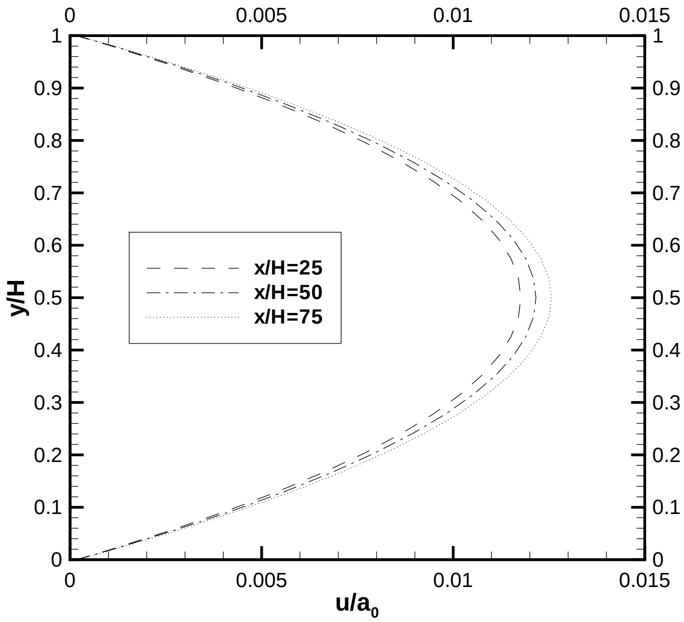

(a)

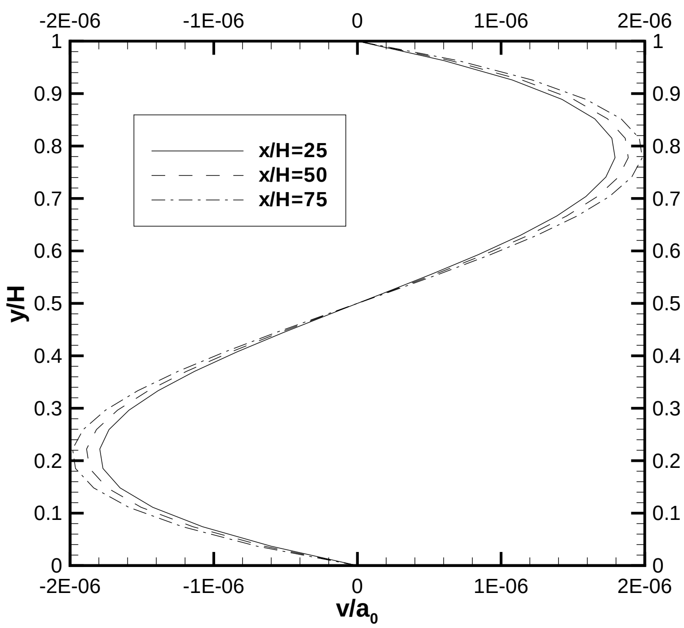

(b)

Figure 5.1: Velocity profile at the channel cross-sections of the case with $\bar{q}_w = 1 \times 10^{-3}$ and $PR = P_{out}/P_{in} = 1.03$. (a) U-velocity profile at three streamwise locations; (b) V-velocity profile at three streamwise locations.

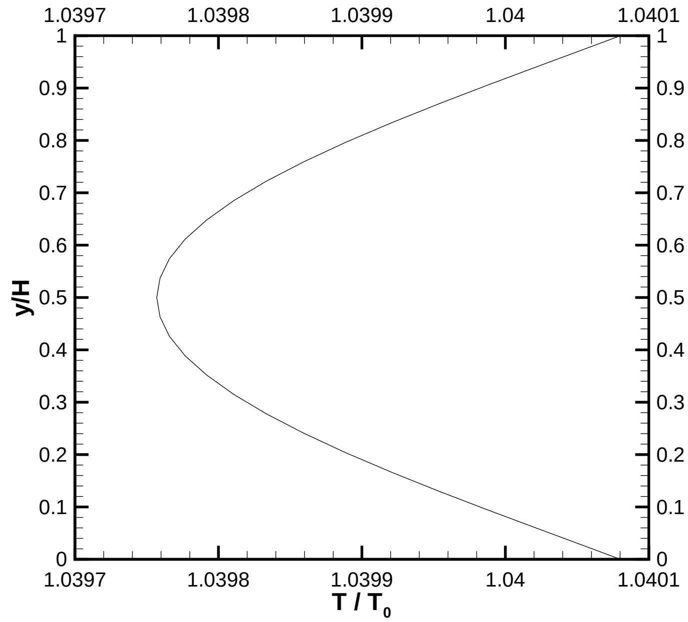

Figure 5.2: Temperature profile at the channel cross-section $x/H = 50$ of the case with $\bar{q}_w = 1 \times 10^{-3}$ and $PR = P_{out}/P_{in} = 1.03$.

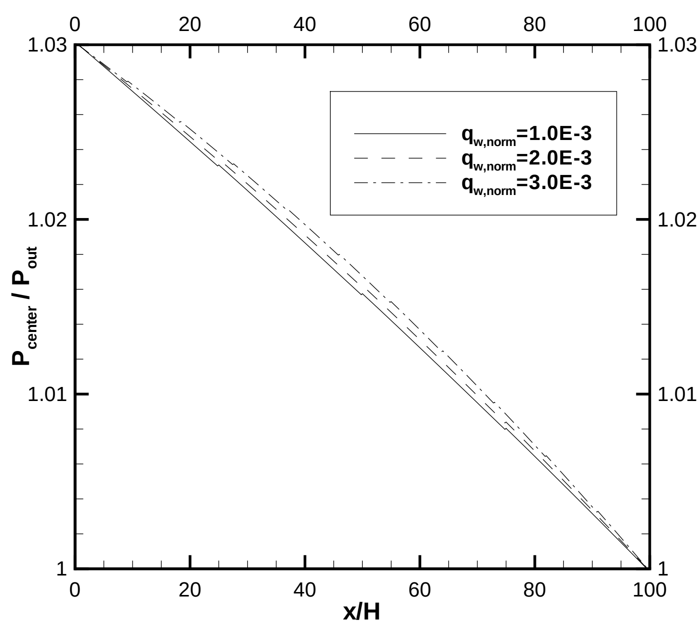

Figure 5.3: Centerline pressure distribution for the cases with $PR = P_{out}/P_{in} = 1.03$ and $\bar{q}_w$ ($q_{w,norm}$ in figure) ranging from 1×10^{-3} to 3×10^{-3}.

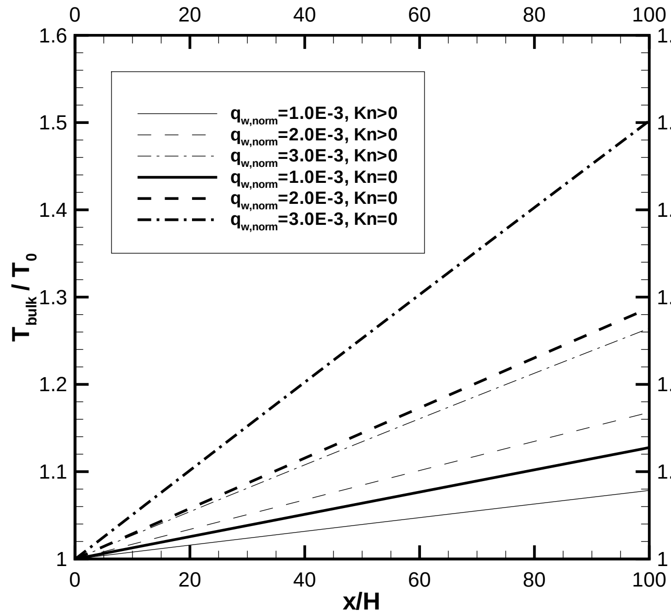

Figure 5.4: Bulk temperature distribution for the cases with $PR = P_{out}/P_{in} = 1.03$ and $\bar{q}_w$ ($q_{w,norm}$ in figure) ranging from 1×10^{-3} to 3×10^{-3}.

temperature. Slip velocity is shown in Fig. 5.6(b). For all three cases with different wall heat fluxes, slip velocity increases along the microchannel, which is consistent with the trend of Kn shown in Fig. 5.6(a). However, slip velocity does not always increase as wall heat flux. There is a turnaround point around $x/H = 30$, before which slip velocity decreases as wall heat flux while increases as wall heat flux thereafter. This is because velocity slip is a function of not only Kn but also the velocity gradient at the wall. As an interpretation of Fig. 5.6(b), Fig. 5.7(b) clearly shows that, closer to inlet, the difference on the velocity gradient at the wall between lower and higher heat flux cases is greater than the difference in far downstream region. Fig. 5.7(a) tells us that although both Kn and velocity slip increase along the channel, wall shear stress always increases along the channel. To understand this fact, first from Fig. 5.7(b), we find that the velocity gradient at the wall increases along the channel. In addition, viscosity also increases along the channel due to temperature rise. Fig. 5.7(a) also shows a turnaround point around $x/H = 50$, before which wall shear stress decreases as wall heat flux while increases as wall heat flux thereafter. Similar to velocity slip, the

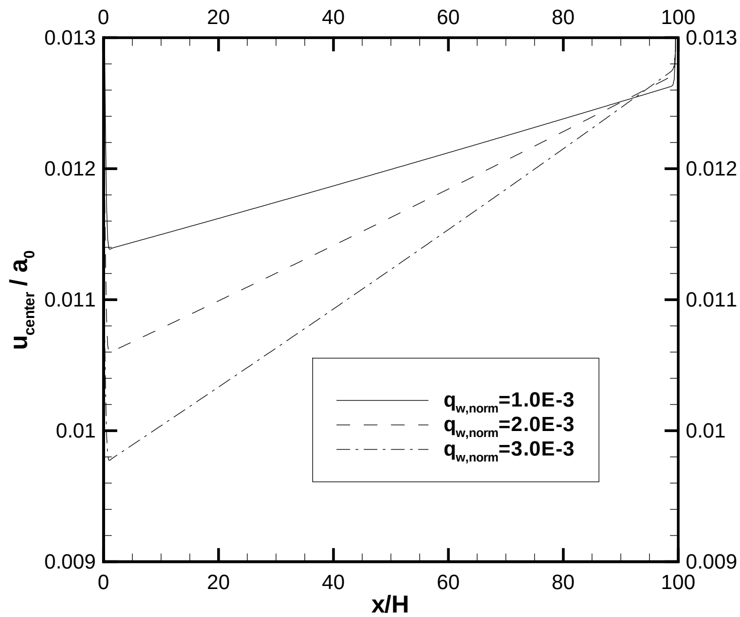

(a)

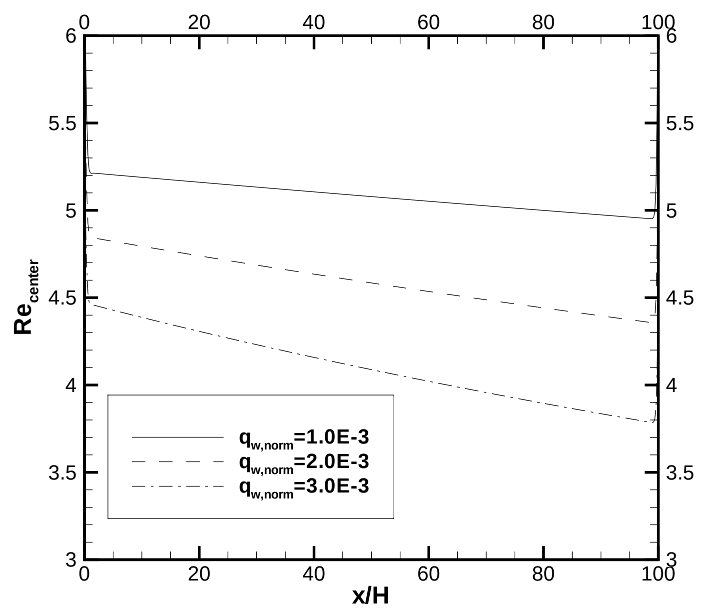

(b)

Figure 5.5: Centerline flow conditions for the cases with $PR = P_{out}/P_{in} = 1.03$ and $\bar{q}_w$ ($q_{w,norm}$ in figure) ranging from 1×10^{-3} to 3×10^{-3}. (a) U-velocity; (b) Reynolds number.

behavior of wall shear stress can be explained by Fig. 5.7(b) together with the increase of viscosity as wall heat flux. The ratio of pressure work over viscous dissipation, PW/VD, along the microchannel is plotted in Fig. 5.8. Using the knowledge learned from Chapter 3-4, Fig. 5.8 is able to interpret the nonlinear bulk temperature profile shown in Fig. 5.4.

Besides outlet temperature, mass flow rate is another main concern. Fig. 5.9(a) and (b) plot volume and mass flow rates, respectively. Fig. 5.9(a) is very consistent with Fig. 5.5(a). Fig. 5.9(b) tells us that mass flow rate decreases as wall heat flux, which means in Fig. 5.7(a), the overall shear is greater for higher wall heat flux cases. From Fig. 5.9(b), it is obvious that the higher outlet temperature achieved in higher wall heat flux cases is not only due to feeding more energy, but also the reduced mass transport ability. The Nusselt number, which is defined by equation 4.2, is plotted in Fig. 5.9, which shows that Nu decreases along the channel for all three cases. Additionally, the Nu's in higher wall heat flux cases are larger than those in lower wall heat flux cases.

5.3.2 Rarefaction Effects

In this section, for the three cases studied in section 5.3.1, rarefaction is turned off by setting Knudsen number to zero, and the results without rarefaction are compared with those with rarefaction. When rarefaction is excluded from the model, the first anticipated change is the lower volume (Fig. 5.9 (a)) and mass flow rates (Fig. 5.9 (b)). Compared to the nonlinear bulk temperature profile of the cases with rarefaction, Fig. 5.4 shows that the bulk temperature profiles for the corresponding cases without rarefaction are almost linear. As for Nu, according to Fig. 5.10, rarefaction leads to lower Nu's for all three cases. Based on the knowledge learned from Chapter 3 and Chapter 4, to understand the findings in Fig. 5.10, two mechanisms must be considered. First, rarefaction influences Nu through wall heat flux. That is, there is a competition between velocity slip and temperature jump on Nu. Velocity slip promotes mass and hence energy transport at the wall, while temperature jump increases thermal resistance at the wall. For the case with nitrogen and rough wall surface, temperature jump is always dominant over velocity slip in this competition. Therefore, in the first

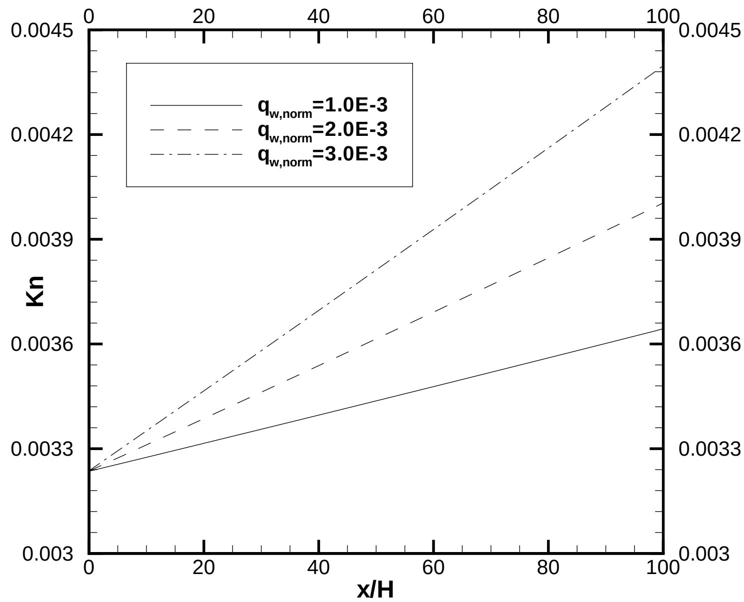

(a)

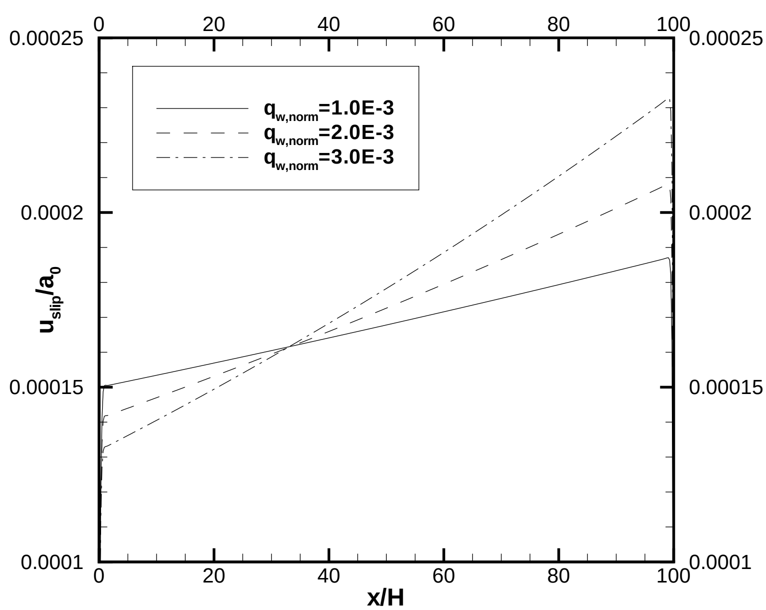

(b)

Figure 5.6: Knudsen number and slip velocity for the cases with $PR = P_{out}/P_{in} = 1.03$ and $\bar{q}_w$ ($q_{w,norm}$ in figure) ranging from 1×10^{-3} to 3×10^{-3}. (a) Knudsen number; (b) Slip velocity.

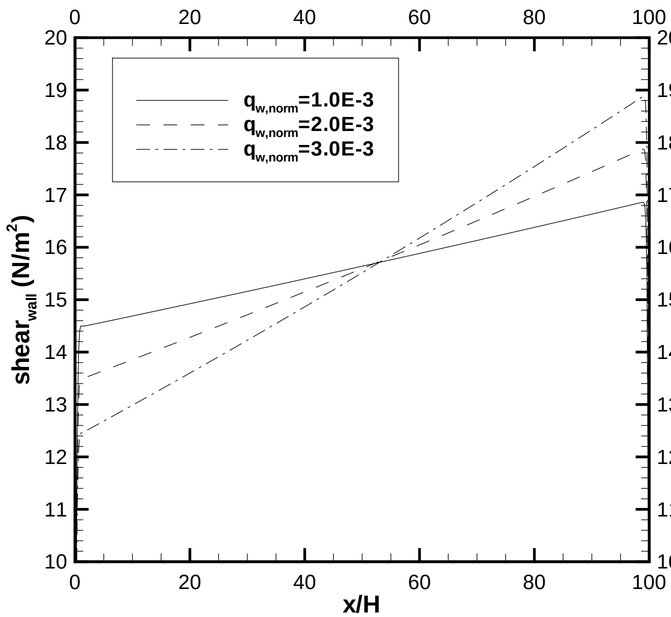

(a)

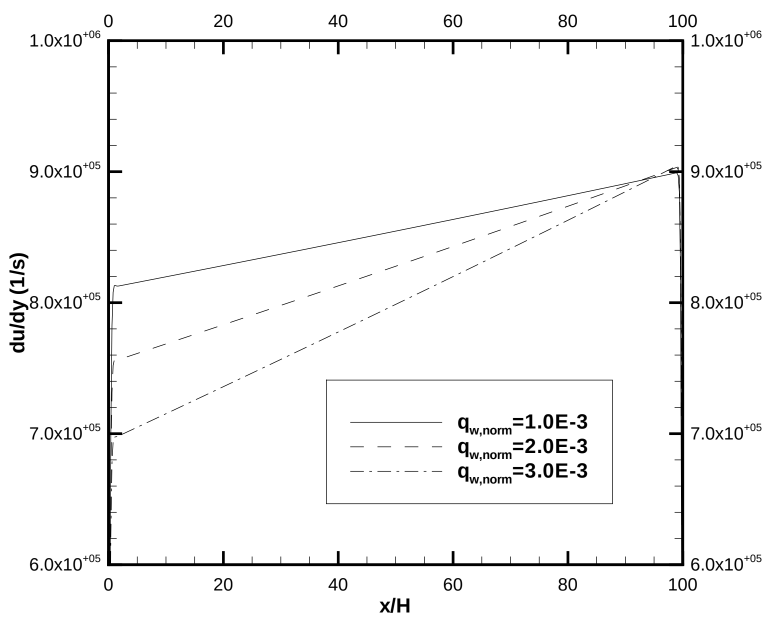

(b)

Figure 5.7: Wall shear stress for the cases with $PR = P_{out}/P_{in} = 1.03$ and $\bar{q}_w$ ($q_{w,norm}$ in figure) ranging from 1×10^{-3} to 3×10^{-3}. (a) Wall shear stress; (b) Velocity gradient at wall.

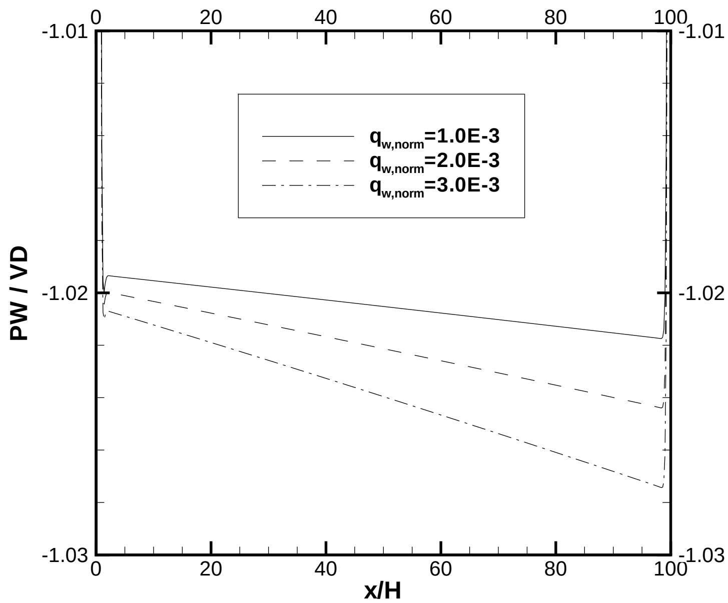

Figure 5.8: Local pressure work over viscous dissipation ratio for the cases with $PR = P_{out}/P_{in} = 1.03$ and $\bar{q}_w$ ($q_{w,norm}$ in figure) ranging from 1×10^{-3} to 3×10^{-3}.

mechanism, rarefaction leads to lower Nu. The second mechanism by which rarefaction influences Nu is through the source terms in energy equation. Specifically, velocity slip reduces VD near the wall while promotes PW near the centerline. It has been learned from the discussion in Chapter 3 that, the magnitude of PW/VD increases as rarefaction and Nu increases as the magnitude of PW/VD. Therefore, in the second mechanism, rarefaction results in larger Nu. For the case with uniform wall heat flux boundary condition, these two mechanisms concurrently exist along the channel. The findings in Fig. 5.10 indicates that the first mechanism is dominant over the second mechanism for the three cases involved.

5.3.3 Inlet/Outlet Pressure Ratio

Fig. 5.11-5.14 compare the results of the three cases with the same heat flux $\bar{q}_w = 2 \times 10^{-3}$ but different inlet/outlet pressure ratios ranging from 1.01 to 1.03. Fig. 5.11 shows that bulk temperature decreases with inlet/outlet pressure ratio. Fig. 5.12 shows that the magnitude of pressure work over viscous dissipation ratio decreases with

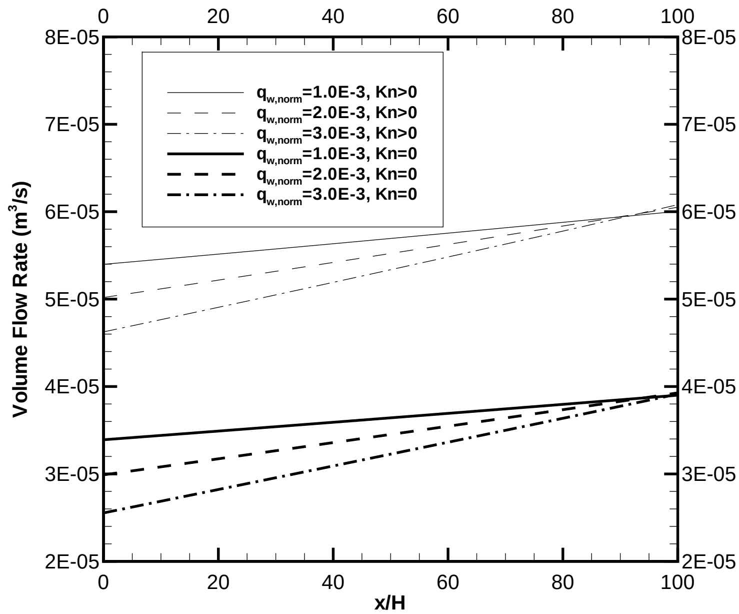

(a)

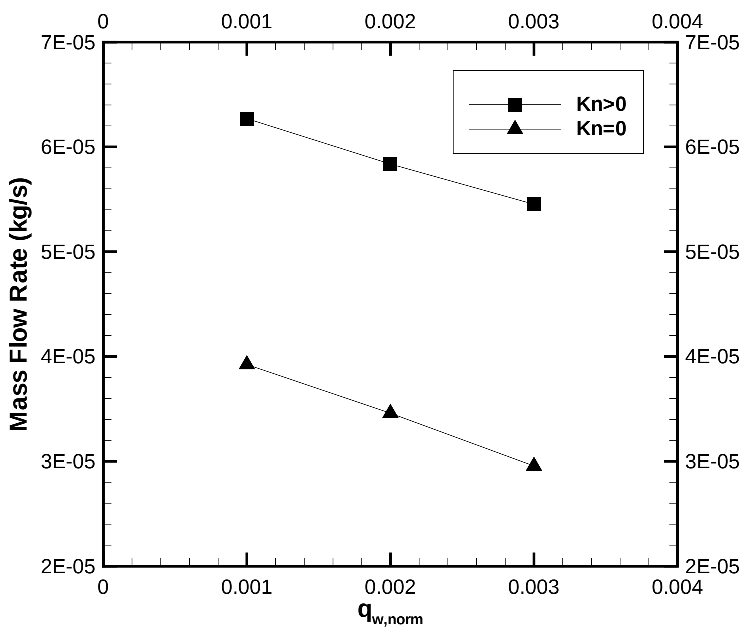

(b)

Figure 5.9: The influence of rarefaction on flow rates for the cases with $PR = P_{out}/P_{in} = 1.03$ and $\bar{q}_w$ ($q_{w,norm}$ in figure) ranging from 1×10^{-3} to 3×10^{-3}. (a) Volume flow rate; (b) Mass flow rate.

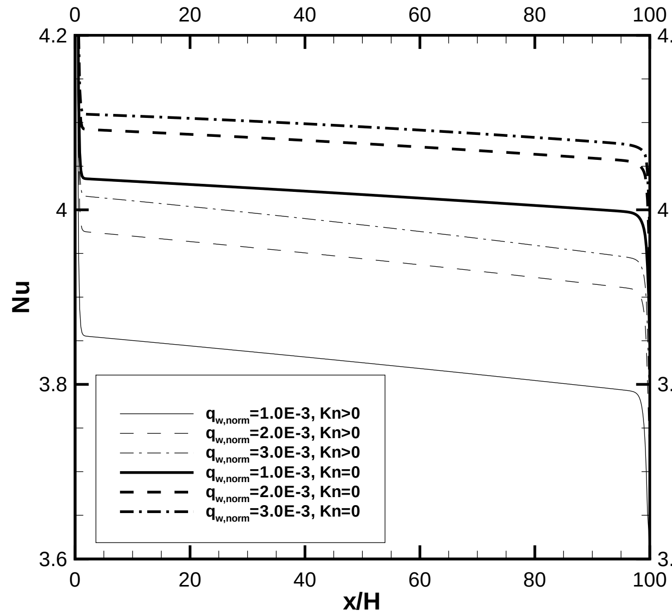

Figure 5.10: The influence of rarefaction on local Nusselt number for the cases with $PR = P_{out}/P_{in} = 1.03$ and $\bar{q}_w$ ($q_{w,norm}$ in figure) ranging from 1×10^{-3} to 3×10^{-3}.

inlet/outlet pressure ratio. Fig. 5.13 shows that local Nusselt number decreases with inlet/outlet pressure ratio due to the increased temperature difference between the wall and bulk fluid, which is caused by the increased mass flow rate as shown in Fig. 5.14.

5.4 Channel #4 with the Characteristic Dimension of 50 μm

All the cases involved in this section are on Channel #4 that is described by Fig. 2.1 and Table 5.1, and using nitrogen as the working gas. The channel height H is 50 μm. In section 5.4.1, the results of the cases with different wall heat fluxes are presented and analyzed. Then in section 5.4.2, rarefaction is turned off by setting Knudsen number to zero, and the results are compared with those in section 5.4.1. Section 5.4.3 focuses on the influence of inlet/outlet pressure ratio.

5.4.1 Wall Heat Flux

For the three cases involved in this section, the inlet/outlet pressure ratio, $PR = P_{out}P_{in}$, is fixed at 1.001, while the dimensionless wall heat flux $\bar{q}_w = \frac{q_w H}{T_0 k_0}$ ranges

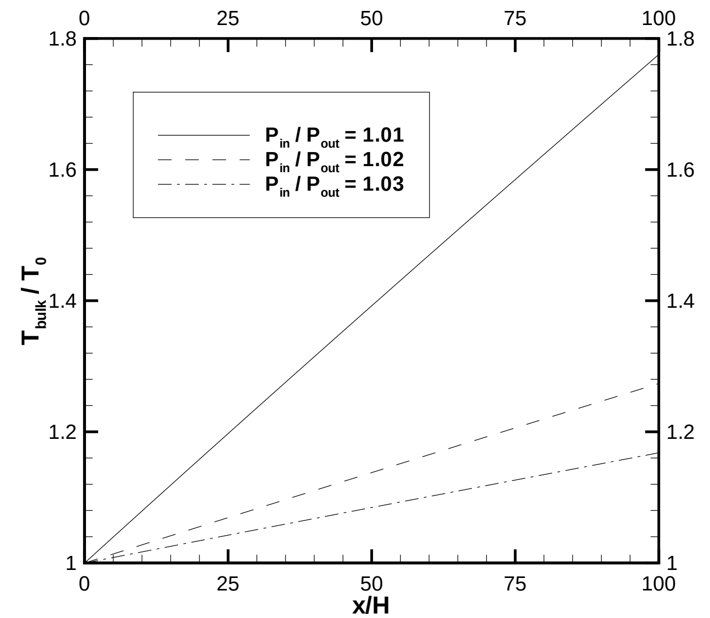

Figure 5.11: The influence of inlet/outlet pressure ratio on bulk temperature.

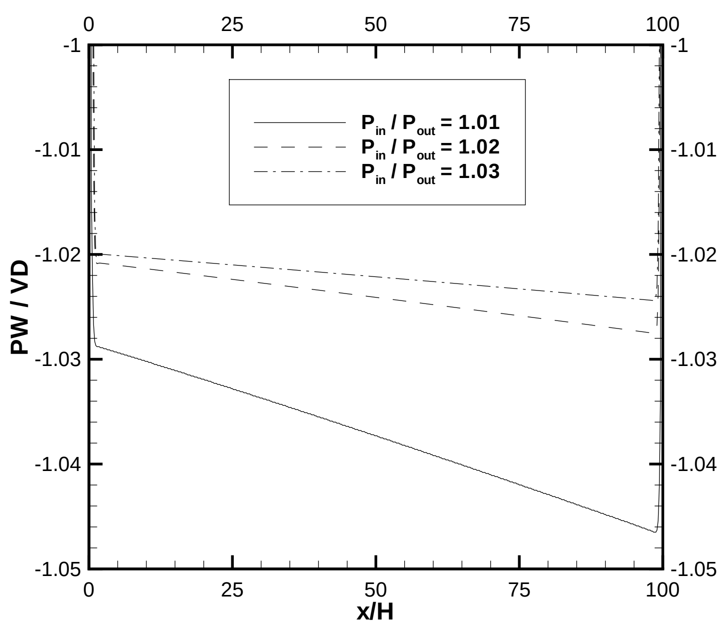

Figure 5.12: The influence of inlet/outlet pressure ratio on the ratio of pressure work over viscous dissipation.

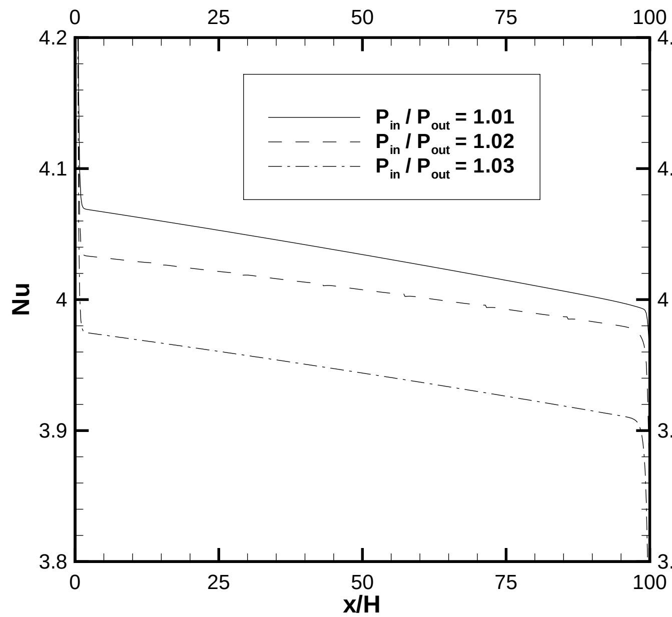

Figure 5.13: The influence of inlet/outlet pressure ratio on Nusselt number.

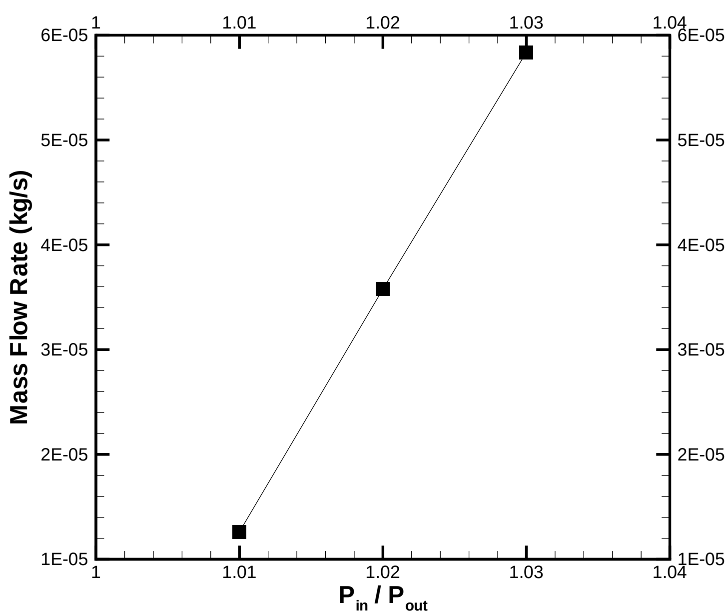

Figure 5.14: The influence of inlet/outlet pressure ratio on mass flow rate.

from 3×10^{-3} to 9×10^{-3}. Fig. 5.1 shows a typical velocity profile of the case with $\bar{q}_w = 3 \times 10^{-3}$, where Fig. 5.15(a) and (b) shows u- and v-velocity profiles at three streamwise locations, respectively. From Fig. 5.15(a) and (b), we found that, compared to u-velocity, v-velocity is negligible. Fig. 5.16 shows the temperature profile at $x/H = 20$.

Centerline pressure profile is shown in Fig. 5.17, from which it is found that the tilting from linear profile becomes greater as wall heat flux increases. This increased departure from linearity for centerline pressure profile as wall heat flux goes up, is mainly caused by the increased thermal expansion accompanying temperature rise. In Fig. 5.18, it is found that bulk temperature increases along the channel, however, its profile is nonlinear and lower than linear profile.

Flow conditions along microchannel centerline are described in Fig. 5.19. From the centerline velocity in Fig. 5.19(a), the acceleration due to compressibility is obvious. Fig. 5.19(b) shows centerline Reynolds number, from which we can find that flows are within laminar regime and Reynolds number decreases along the microchannel. In addition, from Fig. 5.19(b), it is clear that with the same PR, Reynolds number decreases as wall heat flux. The decrease of Reynolds number with wall heat flux can be explained by the reduced density and centerline velocity, as well as the increased viscosity.

Fig. 5.20 and Fig. 5.21 describe the flow conditions close to the channel wall. Fig. 5.20(a) shows that Kn increases along the microchannel and as wall heat flux. The increase of Kn along the channel is due to the drop of pressure and gas density as well as the increase of viscosity caused by temperature rise. The increase of Kn with wall heat flux can be explained by the lower density and higher viscosity due to higher temperature. Slip velocity is shown in Fig. 5.20(b). For all three cases with different wall heat fluxes, slip velocity increases along the microchannel, which is consistent with the trend of Kn shown in Fig. 5.20(a). The slip velocity also increase as wall heat flux. Fig. 5.21(b) shows that, closer to inlet, the difference on the velocity gradient at the wall between the lower and higher heat flux cases is greater than the difference in far downstream region. Fig. 5.21(a) tells us that although both Kn and velocity

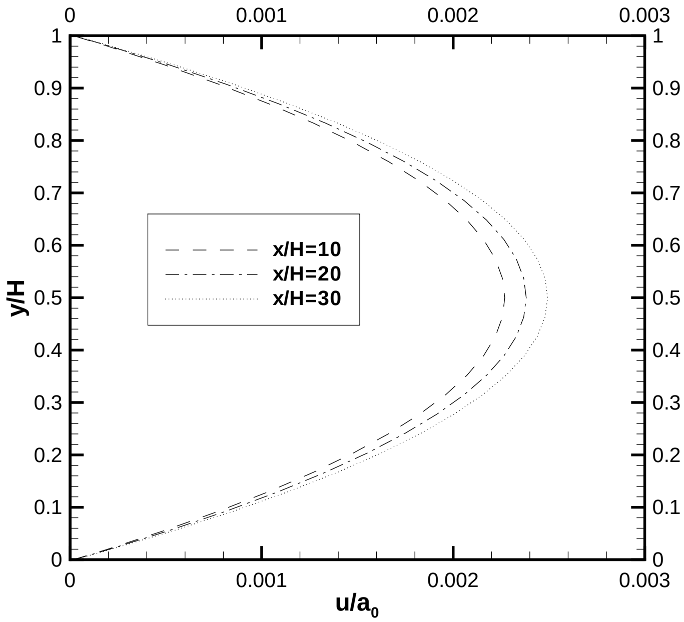

(a)

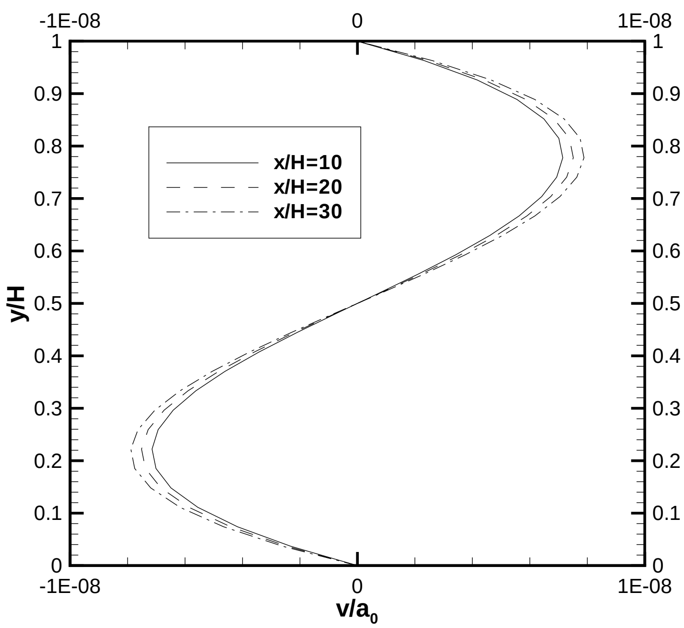

(b)

Figure 5.15: Velocity profile at the channel cross-sections of the case with $\bar{q}_w = 3 \times 10^{-3}$ and $PR = P_{out}/P_{in} = 1.001$. (a) U-velocity profile at three streamwise locations; (b) V-velocity profile at three streamwise locations.

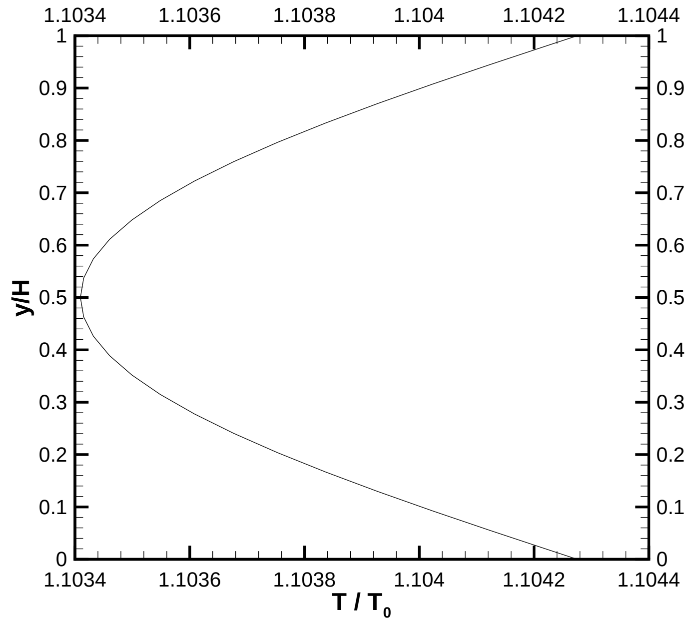

Figure 5.16: Temperature profile at the channel cross-section $x/H = 20$ of the case with $\bar{q}_w = 3 \times 10^{-3}$ and $PR = P_{out}/P_{in} = 1.001$.

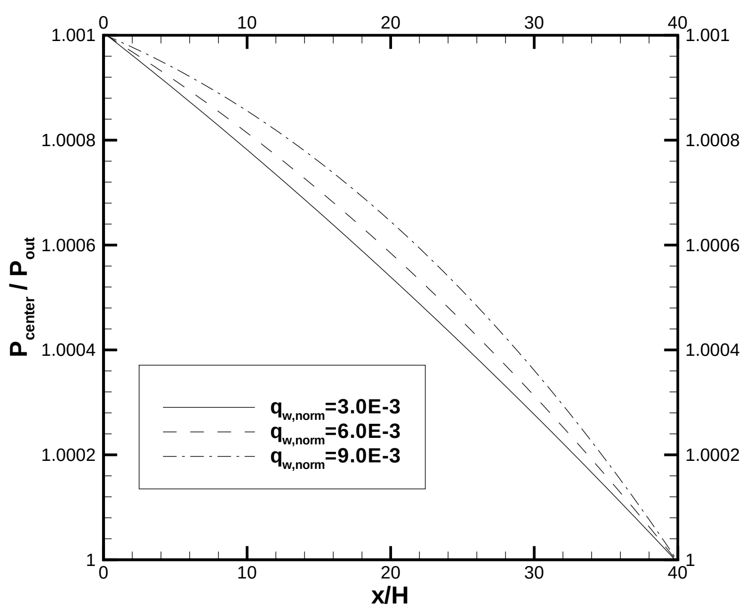

Figure 5.17: Centerline pressure distribution for the cases with $PR = P_{out}/P_{in} = 1.001$ and $\bar{q}_w$ ($q_{w,norm}$ in figure) ranging from 3×10^{-3} to 9×10^{-3}.

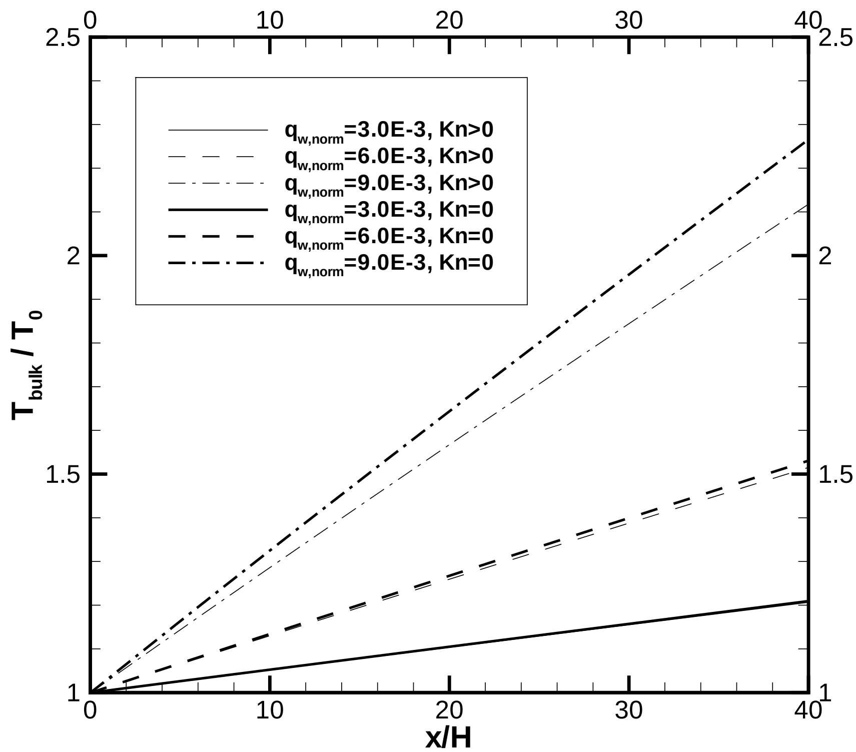

Figure 5.18: Bulk temperature distribution for the cases with $PR = P_{out}/P_{in} = 1.001$ and $\bar{q}_w$ ($q_{w,norm}$ in figure) ranging from 3×10^{-3} to 9×10^{-3}.

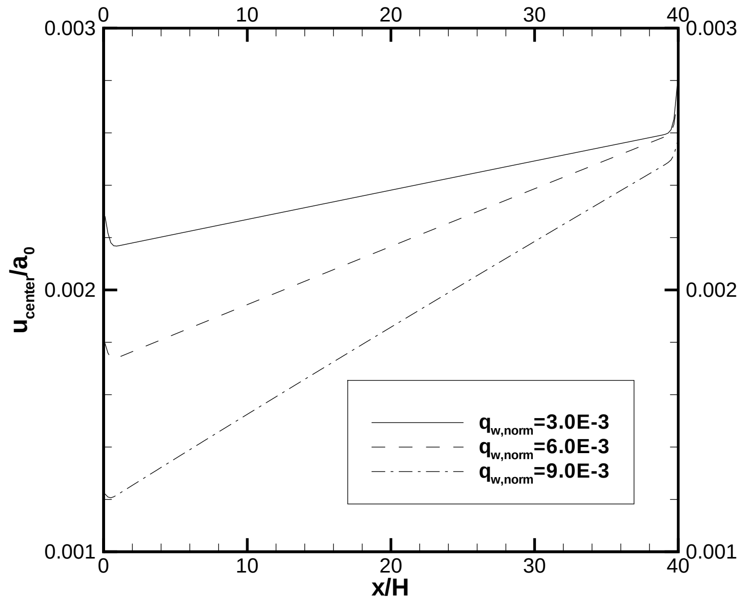

(a)

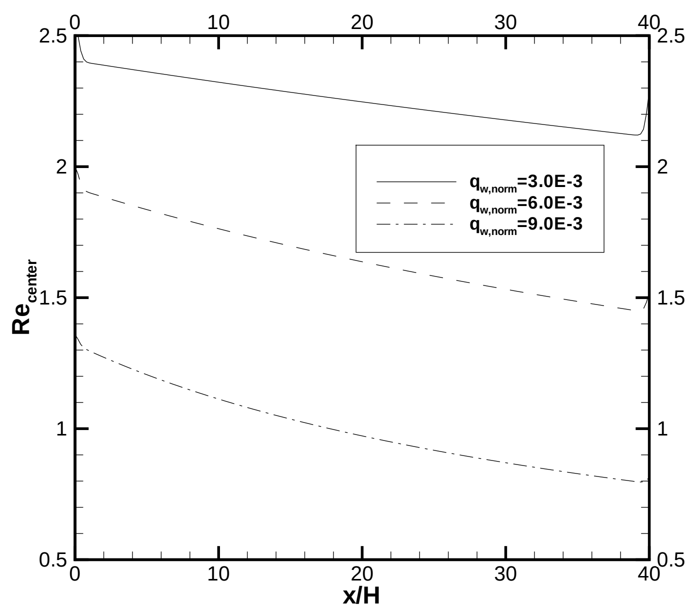

(b)

Figure 5.19: Centerline flow conditions for the cases with $PR = P_{out}/P_{in} = 1.001$ and $\bar{q}_w$ ($q_{w,norm}$ in figure) ranging from 3×10^{-3} to 9×10^{-3}. (a) U-velocity; (b) Reynolds number.

slip increase along the channel, wall shear stress always increases along the channel. To understand this fact, first from Fig. 5.21(b), we find that velocity gradient at wall increases along the channel. In addition, viscosity also increases along the wall due to temperature rise. Fig. 5.21(a) shows a turnaround point around $x/H = 20$, before which wall shear stress decreases as wall heat flux while increases as wall heat flux thereafter. This behavior can be explained by Fig. 5.21(b) together with the increase of viscosity as wall heat flux. The ratio of pressure work over viscous dissipation, PW/VD, along the microchannel is plotted in Fig. 5.22. Using the knowledge learned from Chapter 3-4, Fig. 5.22 is able to interpret the nonlinear bulk temperature profile shown in Fig. 5.18.

Besides outlet temperature, mass flow rate is another main concern. Fig. 5.23(a) and (b) plot volume and the mass flow rates, respectively. Fig. 5.23(a) is very consistent with Fig. 5.19(a). Fig. 5.23(b) tells us that mass flow rate decreases as wall heat flux, which means in Fig. 5.21(a), the overall shear is greater for higher wall heat flux cases. From Fig. 5.23(b), it is obvious that the higher outlet temperature achieved in higher wall heat flux cases is not only due to feeding more energy, but also the reduced mass transport ability. The Nusselt number, which is defined by equation 4.2, is plotted in Fig. 5.23, which shows that Nu decreases along the channel for all three cases. Fig. 5.23 shows that the Nu's in higher wall heat flux cases are higher than those in lower wall heat flux cases before a turnaround point around x/H=15, while lower thereafter. This turnaround behavior is very different from what are found in Fig. 4.10 and Fig. 5.10, where local Nu increases as wall heat flux along the channel.

5.4.2 Rarefaction Effects

In this section, for the three cases studied in section 5.4.1, rarefaction is turned off by setting Knudsen number to zero, and the results without rarefaction are compared with those with rarefaction. When rarefaction is excluded from the model, the first anticipated change is the lower volume (Fig. 5.23 (a)) and mass flow rates (Fig. 5.23 (b)). Compared to the nonlinear bulk temperature profile of the cases with rarefaction, Fig. 5.18 shows that the bulk temperature profiles for the corresponding cases without

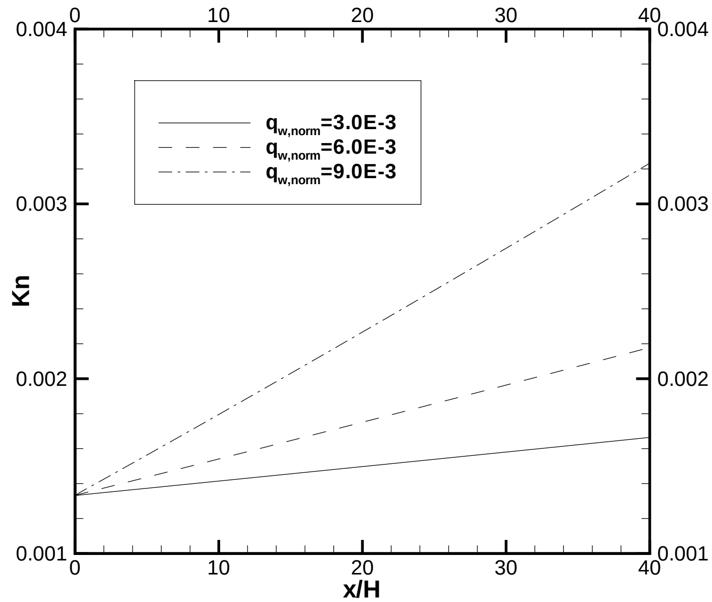

(a)

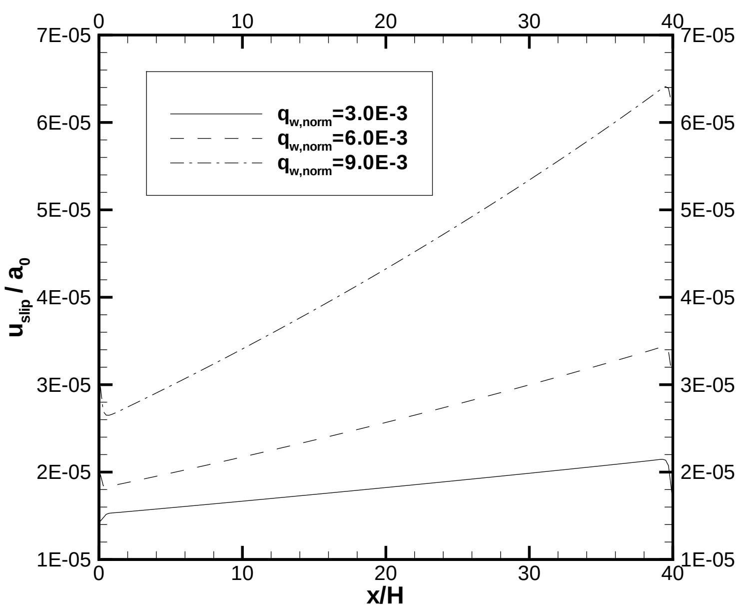

(b)

Figure 5.20: Knudsen number and slip velocity for the cases with $PR = P_{out}/P_{in} = 1.001$ and $\bar{q}_w$ ($q_{w,norm}$ in figure) ranging from 3×10^{-3} to 9×10^{-3}. (a) Knudsen number; (b) Slip velocity.

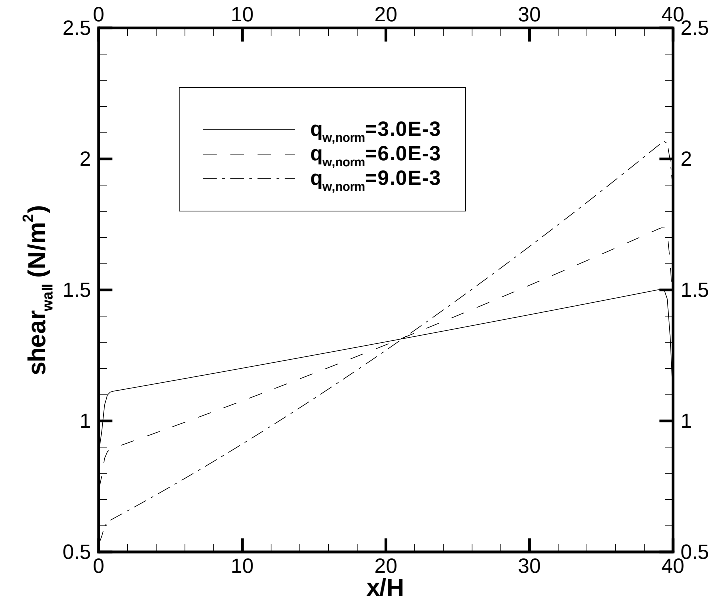

(a)

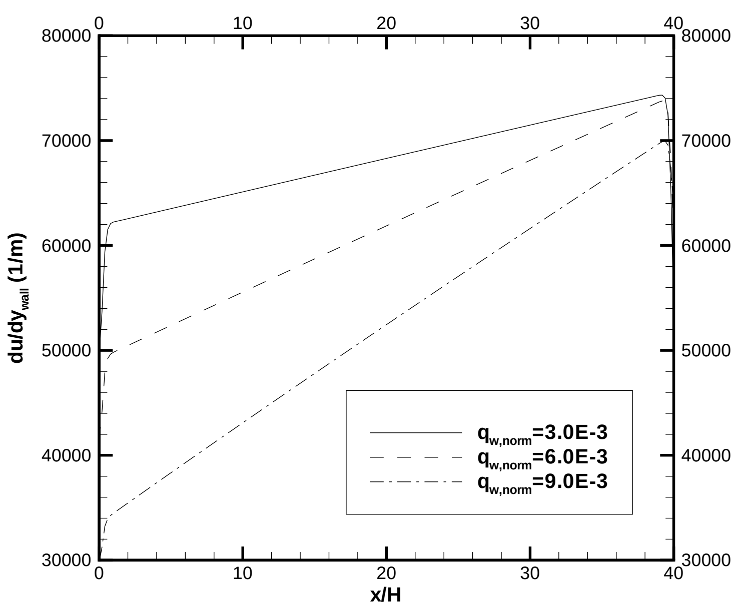

(b)

Figure 5.21: Wall shear stress for the cases with $PR = P_{out}/P_{in} = 1.001$ and $\bar{q}_w$ ($q_{w,norm}$ in figure) ranging from 3×10^{-3} to 9×10^{-3}. (a) Wall shear stress; (b) Velocity gradient at wall.

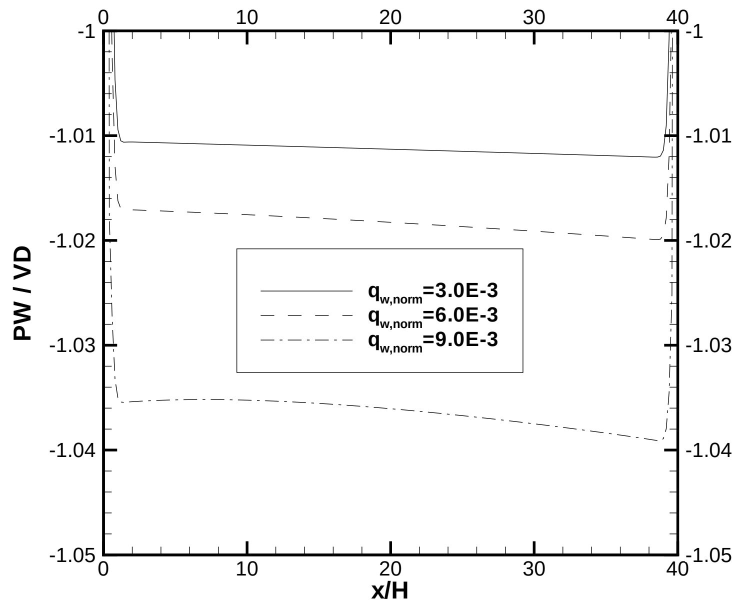

Figure 5.22: Local pressure work over viscous dissipation ratio for the cases with $PR = P_{out}/P_{in} = 1.001$ and $\bar{q}_w$ ($q_{w,norm}$ in figure) ranging from 3×10^{-3} to 9×10^{-3}.

rarefaction are almost linear. It is also found from Fig. 5.18 that the influence of rarefaction is more significant for higher wall heat flux cases. Generally, rarefaction results in lower bulk temperature because of the promoted mass transport and the energy taken up by pressure work. As for Nu, according to Fig. 5.24, the influences of rarefaction are different for the cases with different wall heat fluxes. For the highest wall heat flux, i.e., $\bar{q}_w = 9 \times 10^{-3}$, the influence of rarefaction is inconsistent along the channel. There is a turnaround point around $x/H = 16$. Before this turnaround point, rarefaction result in higher Nu, while leads to lower Nu thereafter. For lower wall heat fluxes, i.e., $\bar{q}_w = 3 \times 10^{-3}$ and $\bar{q}_w = 6 \times 10^{-3}$, rarefaction constantly lead to lower Nu. As discussed in section 4.3.2, there are two mechanisms for rarefaction to either promote or reduce Nu. Whether rarefaction leads to higher or lower Nu essentially depends on the relative strength of these two mechanisms.

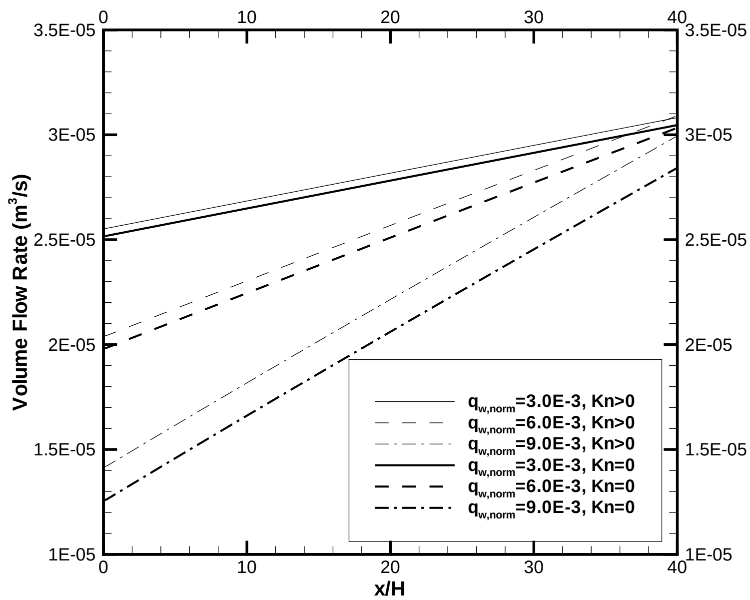

(a)

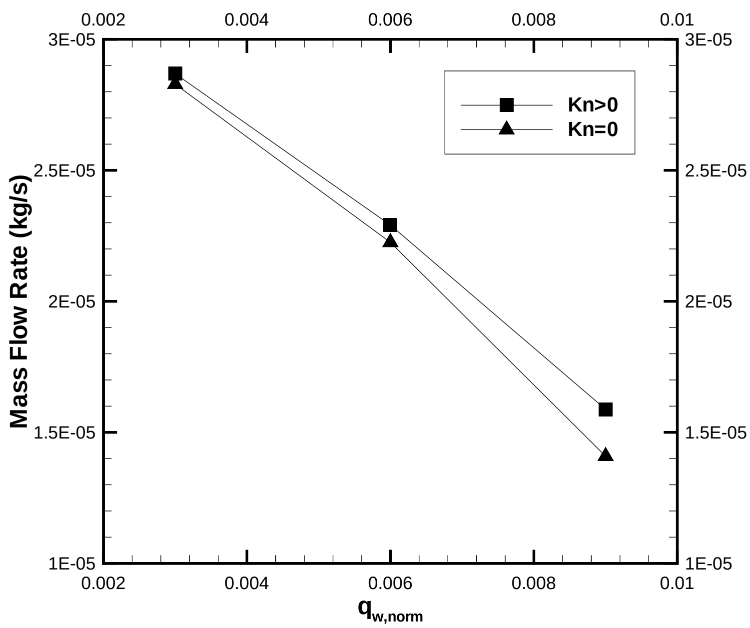

(b)

Figure 5.23: The influence of rarefaction on flow rates for the cases with $PR = P_{out}/P_{in} = 1.001$ and $\bar{q}_w$ ($q_{w,norm}$ in figure) ranging from 3×10^{-3} to 9×10^{-3}. (a) Volume flow rate; (b) Mass flow rate.

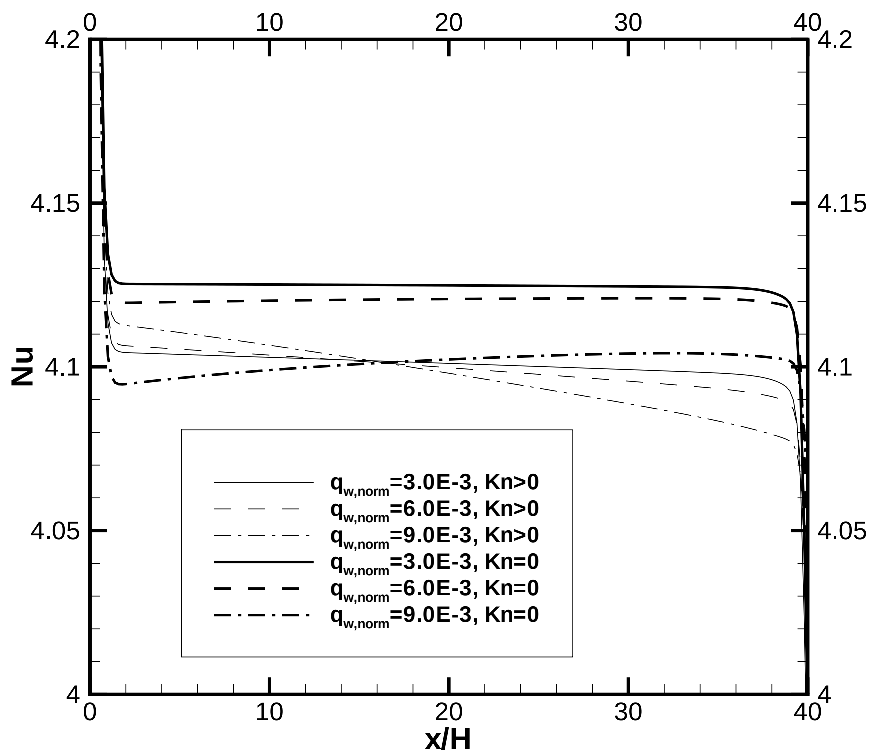

Figure 5.24: The influence of rarefaction on local Nusselt number for the cases with $PR = P_{out}/P_{in} = 1.001$ and $\bar{q}_w$ ($q_{w,norm}$ in figure) ranging from 3×10^{-3} to 9×10^{-3}.

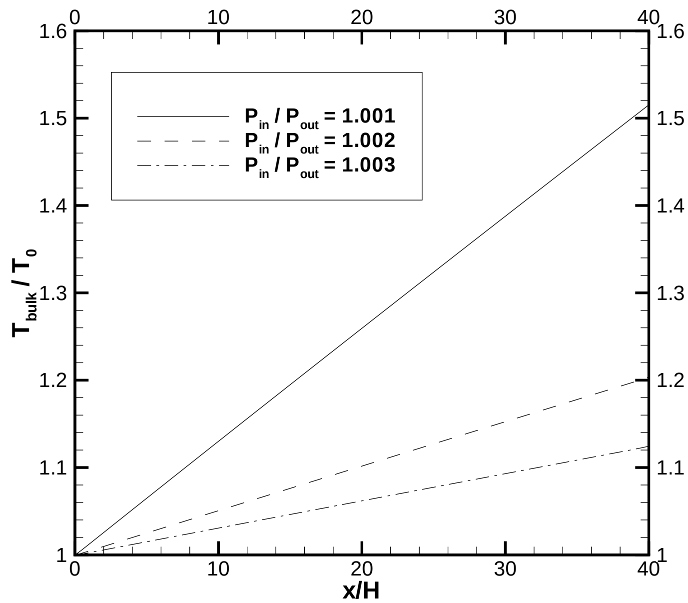

Figure 5.25: The influence of inlet/outlet pressure ratio on bulk temperature.

5.4.3 Inlet/Outlet Pressure Ratio

Fig. 5.25-5.28 compare the results of three cases with the same heat flux $\bar{q}_w = 6 \times 10^{-3}$ but different inlet/outlet pressure ratios ranging from 1.001 to 1.003. Fig. 5.25 shows that bulk temperature decreases with inlet/outlet pressure ratio. Fig. 5.26 shows that the magnitude of pressure work over viscous dissipation ratio decreases with inlet/outlet pressure ratio. Fig. 5.27 shows that local Nusselt number decreases with inlet/outlet pressure ratio due to the increased temperature difference between the wall and bulk fluid, which is caused by the increased mass flow rate as shown in Fig. 5.28.

5.5 Conclusions

Based on the results and analysis in section 5.3 and section 5.4, several conclusions are made below for the larger-dimension ($10 - 100\mu m$) microchannel pressure-driven nitrogen slip flows under uniform heat flux wall boundary condition:

- The inlet/outlet pressure difference required to get similar Reynolds numbers as those of the microchannels with characteristic dimensions below 10 μm drops

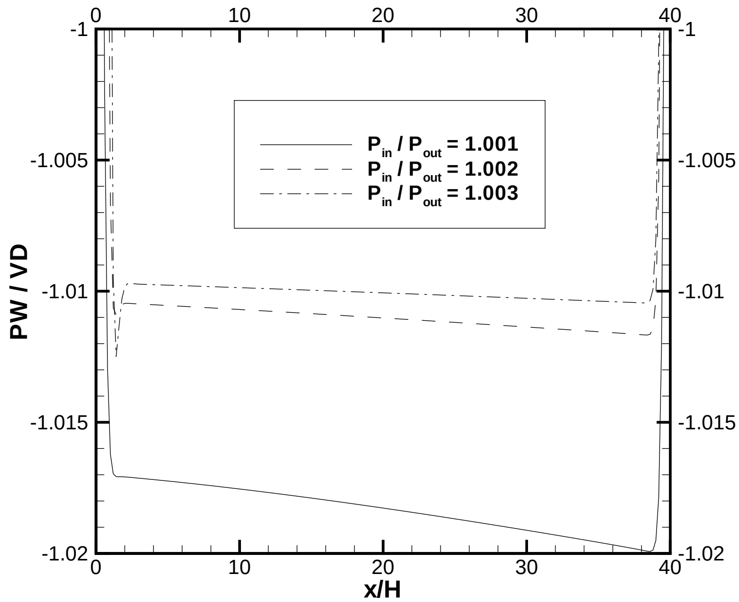

Figure 5.26: The influence of inlet/outlet pressure ratio on the ratio of pressure work over viscous dissipation.

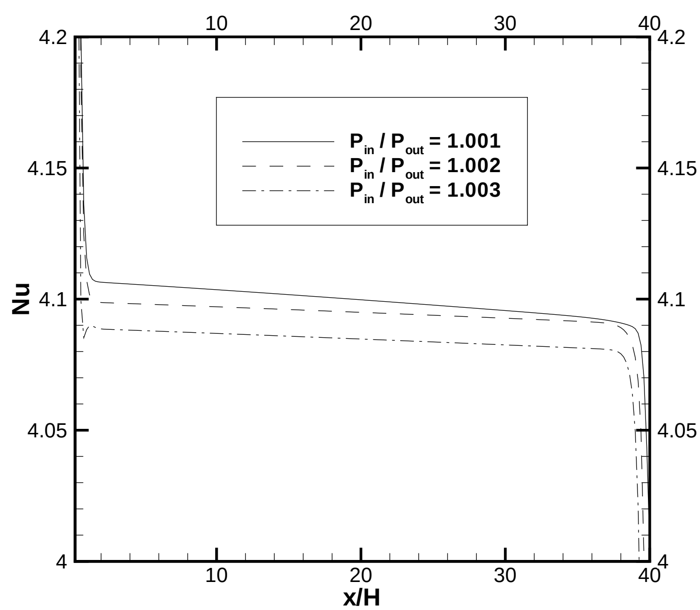

Figure 5.27: The influence of inlet/outlet pressure ratio on Nusselt number.

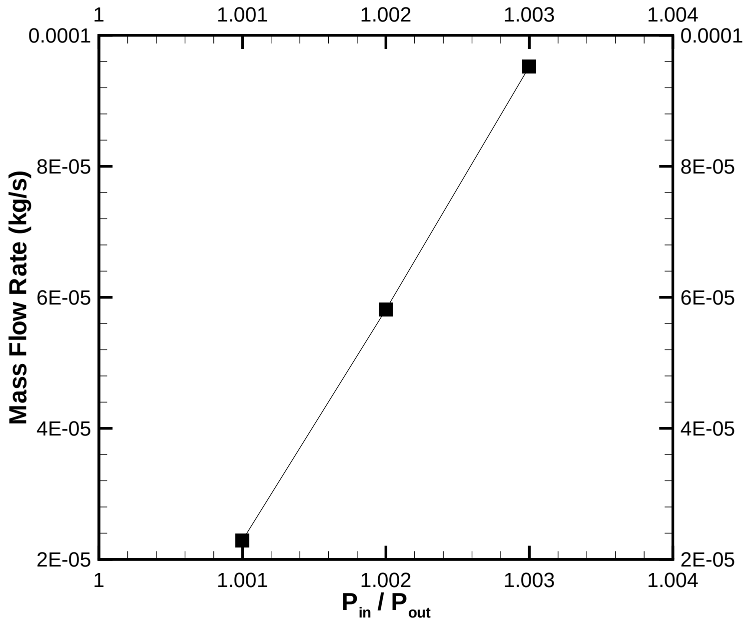

Figure 5.28: The influence of inlet/outlet pressure ratio on mass flow rate.

dramatically: compared to the inlet/outlet pressure difference required by the channel of 3μm high, for the microchannels of 20 and 50μm high, the required pressure drops are about one and 0.1 percent, respectively.

- The hydraulic and thermal characteristics are very similar to those of the microchannels with a characteristic dimension of $3\mu m$.
- Rarefaction is weaker compared to that of the microchannels with characteristic dimensions below $10\mu m$. However, rarefaction is still nonnegligible.

Chapter 6

Two Dimensional Steady-State Conjugate Heat Transfer for Pressure-Driven Nitrogen Flow in Long Microchannels Under Uniform Heat Flux Wall Boundary Condition

6.1 Introduction

Due to the small height of rectangular microchannel and the fabrication requirement, the ratio of substrate thickness over microchannel height is no longer negligible as in most macrochannel cases. Axial conduction is a potential factor that could lead to the discrepancy between existing experimental results [7] and continum theory. Therefore, conjugate heat transfer is of great interest for microchannel flows. For conjugate heat transfer, a number of issues need to be carefully examined, including the role of axial conduction in substrates, the influence of substrate thickness over channel height ratio and substrate material properties. Conjugate analysis for microchannel liquid flows has been conducted by several groups [38, 39, 40, 41, 42]. On the other hand, based on my literature review, very little has been done on the conjugate heat transfer for microchannel gaseous slip flows. As an extension of Chapter 4, this chapter concentrates on the conjugate heat transfer under uniform wall heat flux boundary condition for the same long microchannel as that investigated in Chapter 4 with 500:1 length-to-height ratio. Nitrogen is still the working gas. Four different kinds of substrate materials are studied, including fused silica, pyroceram, silicon nitride and commercial bronze (Table 6.1). The organization of this chapter is as follows: section 6.2 describes the mathematical model and numerical procedure; section 6.3 presents the numerical results with analysis; finally, conclusions are given in section 6.4.

Table 6.1: Substrate material properties at 300K and the variable property models.

Material	Commercial Bronze	Silicon Nitride	Pyroceram	Fused Silica
Density at 300K (kg/m^3), ρ_0	8800	2400	2600	2220
Thermal Conductivity at 300K $(W/m \cdot K)$, k_0	52	16	3.98	1.38
Thermal Capacity at 300K $(J/kg \cdot K)$, $C_{p,0}$	420	691	808	745
Thermal Conductivity at Temperature T, k	k_0	$k_0(T/T_0)^{-0.49}$	$k_0(T/T_0)^{-0.26}$	$k_0(T/T_0)^{0.33}$
Thermal Capacity at Temperature T, C_p	$C_{p,0}(T/T_0)^{0.38}$	$C_{p,0}(T/T_0)^{0.44}$	$C_{p,0}(T/T_0)^{0.35}$	$C_{p,0}(T/T_0)^{0.62}$

6.2 Model Description and Numerical Procedure

Fig. 6.1 shows the computational domain of the current 2D conjugate heat transfer problem, where the shaded areas are channel walls and the blank area is the channel. The readers can refer to section 2.2 for governing equations as well as boundary conditions used at the inlet and outlet for the gas flow within the channel. When solving the fluid field, variable properties, rarefaction (velocity slip, thermal creep and temperature jump), compressibility and viscous dissipation are all included. The substrates are governed by energy equation,

$$c_p \left[\frac{\partial \rho T}{\partial t} + \frac{\partial \rho u T}{\partial x} + \frac{\partial \rho v T}{\partial y} \right] = \frac{\partial}{\partial x} \left(k \frac{\partial T}{\partial x} \right) + \frac{\partial}{\partial y} \left(k \frac{\partial T}{\partial y} \right) \tag{6.1}$$

The boundary conditions in y-direction, i.e., at $y = 0$ and $y = 2H_s + H$ are given by $q = q_w$. The temperatures at gas-solid interfaces are obtained by solving the two equations

$$\begin{aligned} T_g - T_w &= \frac{2 - \sigma_T}{\sigma_T} \left(\frac{2\gamma}{1+\gamma} \right) \frac{\lambda}{\mathrm{Pr}} \left(\frac{\partial T}{\partial n} \right)_w \\ q_g &= q_s \end{aligned} \tag{6.2}$$

where the first equation is from the temperature jump at wall, and the second is required by the fact that no energy is stored at gas-solid interface. The two ends of the substrates in streamwise direction are insulated, i.e., $\partial T / \partial x = 0$. Variable property model is applied to the solid domain, too. Four different substrate materials are studied, whose properties at 300K and the corresponding variable property models are listed in Table 6.1. Different from gas, since the solid is almost incompressible, only thermal conductivity and thermal capacity are treated as variable.

The readers can refer to section 2.3 for numerical procedure. Here solid phase is treated as the extension of fluid phase but with zero velocity. The employed computational method is based on the SIMPLER algorithm and has both a serial and a parallel version. The parallel solver is built with the domain decomposition method (DDM). As we did before, parallel solver is first employed and runs until some convergence criteria are reached. Then to eliminate the singularity caused by the DDM, the results from parallel solver are fed to serial solver, which then runs until the desired convergence is

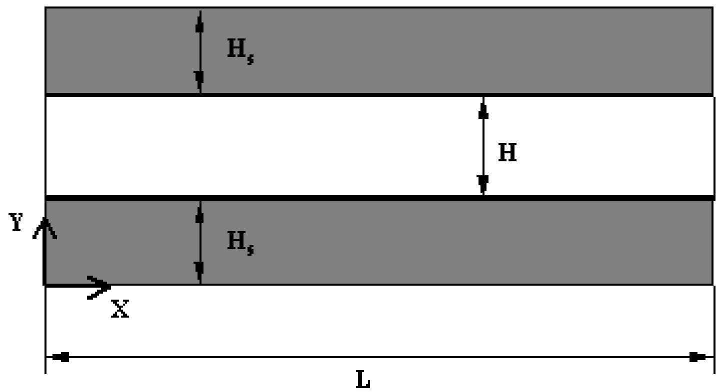

Figure 6.1: The schematic of the 2D computational domain for the current conjugate heat transfer problem, where the shaded areas are channel walls and the blank area is the channel.

achieved. To get steady state solution, time marching method is used. The convergence criteria for parallel solver are of the form

$$\varepsilon = \max \left\{ \begin{array}{ll} \text{if } \xi^n \neq 0 & \frac{|\xi^{n+1}-\xi^n|}{|\xi^n|} \\ \text{if } \xi^n = 0 & |\xi^{n+1}| \end{array} \right\} \tag{6.3}$$

where ξ applies to streamwise velocity u, temperature T as well as the variables in the overlapping regions of adjacent subdomains and the superscripts denote the time step. The convergence criteria for serial solver take the same form as for parallel solver, while ξ only applies to streamwise velocity u and temperature T. Time marching stops when ε falls below 1×10^{-8} for the final serial run. In this chapter, the channel to be studied is Channel #2 described by Table 2.1. Using the grid dependence test results presented in Table 6.2, the 1100×46 $(X \times Y)$ grid is selected for the case with $H_s/H = 1.0$. For the cases with $H_s/H \neq 1.0$, the grid size in y-direction will be scaled proportionally.

6.3 Results and Discussion

This section presents the results and analysis of the conjugate heat transfer for Channel #2 (Table 2.1). Section 6.3.1 concentrates on thermal characteristics, where the influence of substrate axial conduction is revealed. Section 6.3.2 shows the influence of substrate thickness. Finally, section 6.3.3 studied the effects of variable properties of substrate materials.

Table 6.2: Grid dependence test results for a case using fused silica as substrate material and with $H_s/H = 1.0$, $P_{in}/P_{out} = 2.0$ and $\bar{q}_w = 2 \times 10^{-4}$. (a)Centerline temperature; (b)Centerline streamwise velocity.

(a) T_{center}/T_0

Grid	$x = 300\mu m$	$x = 600\mu m$	$x = 900\mu m$	$x = 1200\mu m$
550×22	1.08753386	1.14376144	1.19000868	1.22207080
1100×46	1.08789430	1.14635700	1.19420753	1.22723114
2200×88	1.08701757	1.14570431	1.19358562	1.22642706

(b) $(u_{center}/a_0) \times 100$

Grid	$x = 300\mu m$	$x = 600\mu m$	$x = 900\mu m$	$x = 1200\mu m$
550×22	0.94459918	1.08393455	1.26435517	1.52055352
1100×46	0.90380646	1.03867656	1.21313704	1.46018316
2200×88	0.89489648	1.02909980	1.20219017	1.44748167

6.3.1 Thermal Characteristics

Fig. 6.2 shows a typical temperature profile at the channel cross-section $x/H = 250$ of the case using fused silica as substrate material with $\bar{q}_w = 1 \times 10^{-4}$, $H_s/H = 1.0$ and $PR = P_{out}/P_{in} = 2.0$. In Fig. 6.2, the slope discontinuity at gas interfaces is very apparent. Fig. 6.3 presents the bulk temperature profile along the microchannel for the cases with $P_{in}/P_{out} = 2.0$, $\bar{q}_w = 2 \times 10^{-4}$ and $H_s/H = 1.0$. It is clear that, due to the axial conduction within the substrates, bulk temperature profile becomes flatter as the thermal conductivity of substrates increases. Fig. 6.4 compares the maximum temperature of the cases with $P_{in}/P_{out} = 2.0$, $\bar{q}_w$ ranging from 1×10^{-4} to 3×10^{-4} and $H_s/H = 1.0$. From Fig. 6.4, the maximum temperature decreases with the thermal conductivity of substrate material, which is in agreement with Fig. 6.3. The Nu, which is defined by eqn 4.2, is plotted in Fig. 6.5 for the cases with $\bar{q}_w = 2 \times 10^{-4}$, $H_s/H = 1.0$ and $PR = P_{out}/P_{in} = 2.0$. Fig. 6.5 shows that local Nu decreases as the thermal conductivity of substrate material. This trend can be explained by the lower heat flux from the substrate to the fluidwhich results from the stronger axial conduction within substrates. It is also found in Fig. 6.5 that, local Nu does not go monotonously along the channel for the case using commercial bronze as substrate material. This fact can also be explained by the strong axial conduction in substrates, which makes the temperature difference between substrates and bulk fluid smaller in

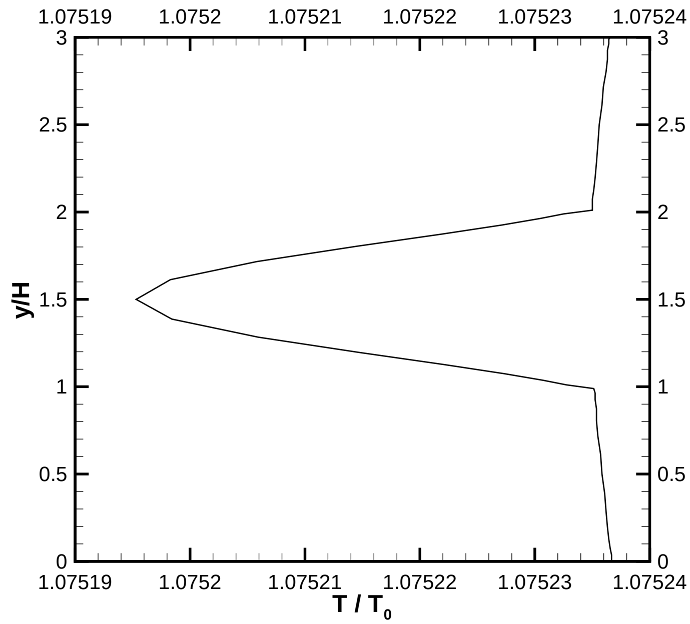

Figure 6.2: Temperature profile at the channel cross-section $x/H = 250$ of the case using fused silica as substrate material with $\bar{q}_w = 1 \times 10^{-4}$, $H_s/H = 1.0$ and $PR = P_{out}/P_{in} = 2.0$.

outlet region. Fig. 6.6 (a)-(d) show the local Nu for the four different substrate materials, respectively, where $P_{in}/P_{out} = 2.0$, $\bar{q}_w$ ranging from 1×10^{-4} to 3×10^{-4} and $H_s/H = 1.0$. It is found that Nu increases with wall heat flux for all four substrate materials. Again, in Fig. 6.6, it is found that Nu does not go monotonously along the channel for some high heat flux cases with high-thermal-conductivity substrate materials. The bulk temperature profiles for the cases with P_{in}/P_{out} ranging from 1.5 to 2.5, $\bar{q}_w = 2 \times 10^{-4}$ and $H_s/H = 1.0$ are shown in Fig. 6.7. For all four substrate materials, bulk temperature decreases as P_{in}/P_{out}, which can be readily interpreted with the consideration of mass flow rate. Fig. 6.8 shows that the maximum temperature decreases as P_{in}/P_{out}, which is in accordance with Fig. 6.7. Local Nu is shown to decrease as P_{in}/P_{out} by Fig. 6.9. This is because mass flow rate increases as P_{in}/P_{out}, which leads to larger temperature difference between substrates and bulk fluid. Fig. 6.9 clearly shows the non-monotonous feature of Nu along the channel for some high heat flux cases with high-thermal-conductivity substrate materials, which can be explained with the same theory used to explain the similar phenomena found in Fig. 6.5 and 6.6.

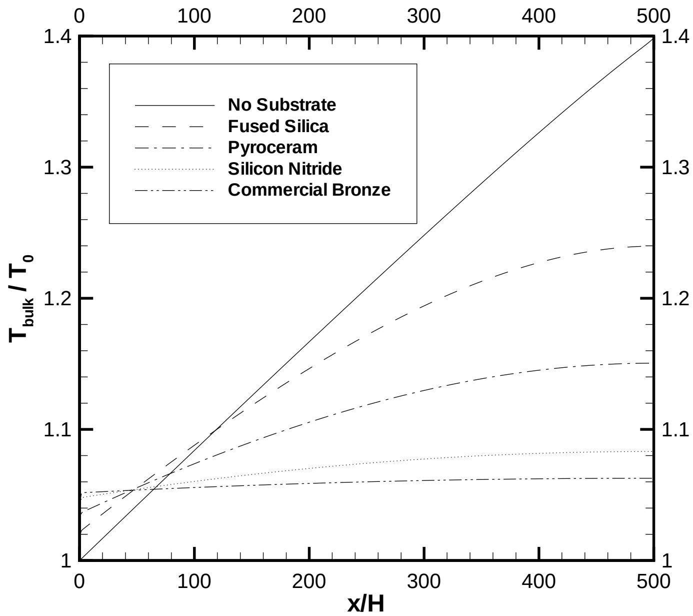

Figure 6.3: Bulk temperature profiles for the cases with $\bar{q}_w = 2 \times 10^{-4}$, $H_s/H = 1.0$ and $PR = P_{out}/P_{in} = 2.0$.

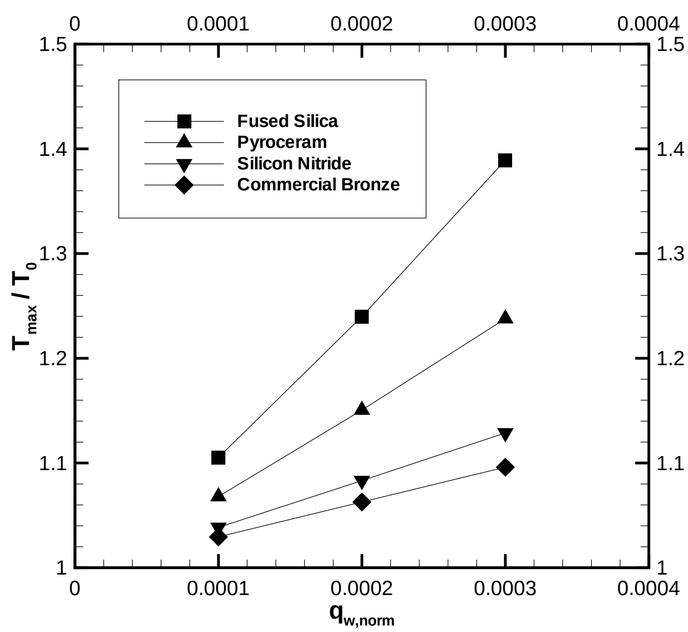

Figure 6.4: The maximum temperatures for the cases with $P_{in}/P_{out} = 2.0$, $\bar{q}_w$ ranging from 1×10^{-4} to 3×10^{-4} and $H_s/H = 1.0$.

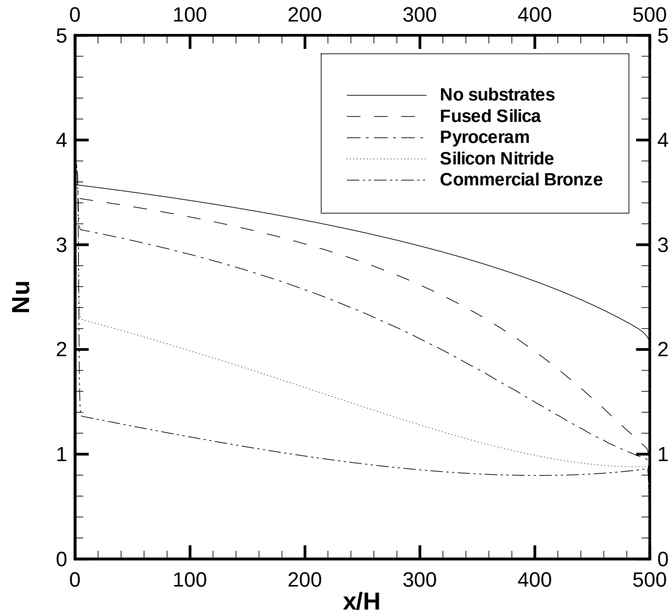

Figure 6.5: Local Nusselt number for the cases with $\bar{q}_w = 2 \times 10^{-4}$, $H_s/H = 1.0$ and $PR = P_{out}/P_{in} = 2.0$.

6.3.2 The Substrate Thickness

As mentioned in section 6.1, the influence of substrate thickness is of great interest for microchannel conjugate heat transfer. For $H_s/H = 10.0$, due to the strong axial conduction in substrates, the results for silicon nitride and commercial bronze do not meet the convergence criteria mentioned in section 6.2, i.e., $\varepsilon < 1\times10^{-8}$. For these two cases, $\varepsilon < 1\times10^{-5}$ is used to identify convergence. Fig. 6.10 plots the bulk temperature profiles along the microchannel for the cases with $P_{in}/P_{out} = 2.0$ and $\bar{q}_w = 2\times10^{-4}$ but different H_s/H's. Fig. 6.10 (a)-(d) show the influence of substrate thickness for the four different substrate materials involved in this study, respectively. For all four substrate materials, the bulk temperature profiles become flatter as substrate thickness increases. Fig. 6.11 shows that the maximum temperature decreases as substrate thickness for all four substrate materials, where all the maximum temperatures are normalized by that of the case without substrates. Local Nusselt number is presented in Fig. 6.12 (a)-(d) for the four substrate materials involved in this study. It is found that Nu decreases as substrate thickness for all four substrate materials, which can be explained by the

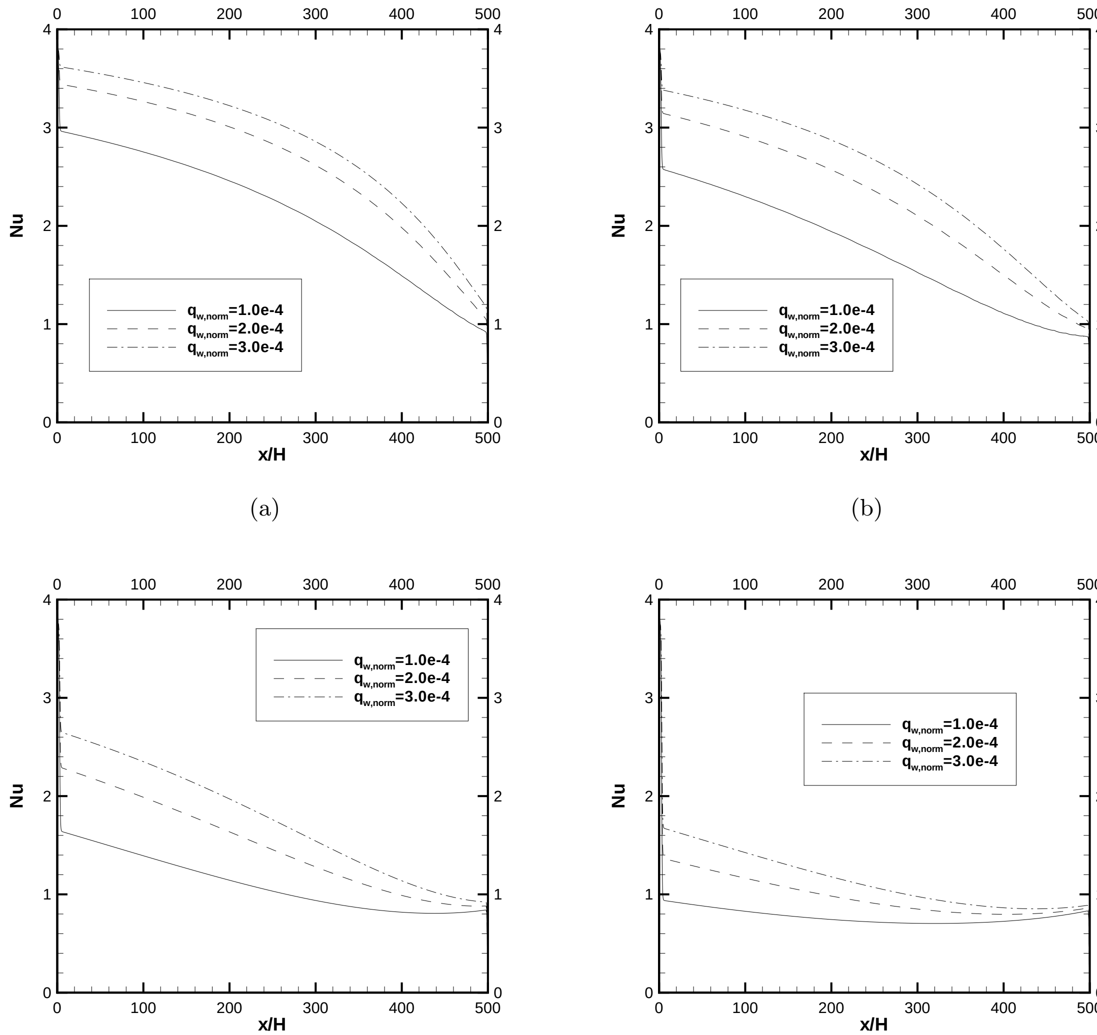

(a) (b) (c) (d)

Figure 6.6: Local Nusselt number for the cases with $\bar{q}_w$ ranging from 1×10^{-4} to 3×10^{-4}, $H_s/H = 1.0$ and $PR = P_{out}/P_{in} = 2.0$. The substrate material is (a) Fused silica; (b) Pyroceram; (c) Silicon Nitride; (d) Commercial Bronze.

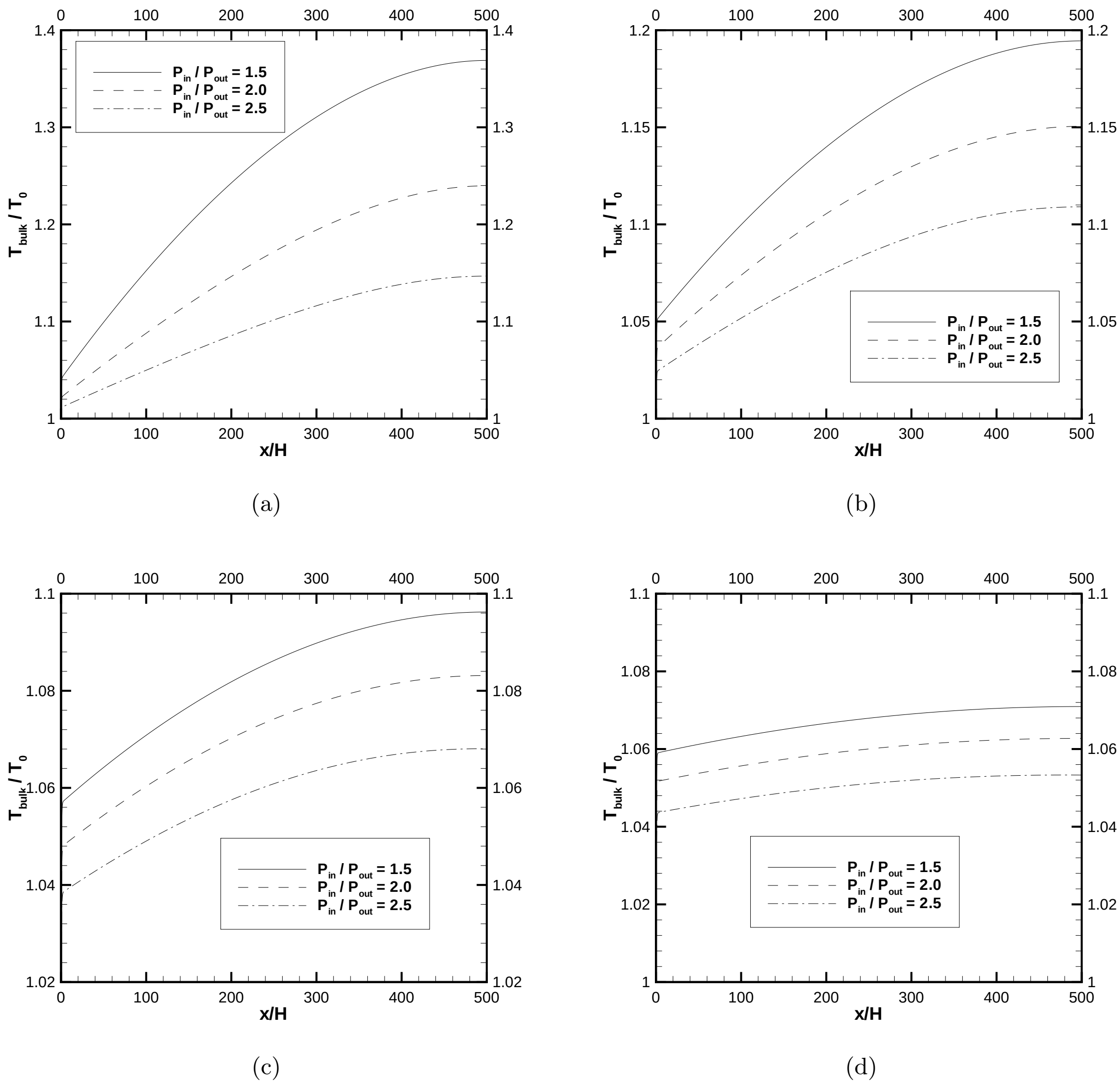

Figure 6.7: Bulk temperature profiles along the microchannel for the cases with P_{in}/P_{out} ranging from 1.5 to 2.5, $\bar{q}_w = 2 \times 10^{-4}$ and $H_s/H = 1.0$. The substrate material is (a) Fused silica; (b) Pyroceram; (c) Silicon Nitride; (d) Commercial Bronze.

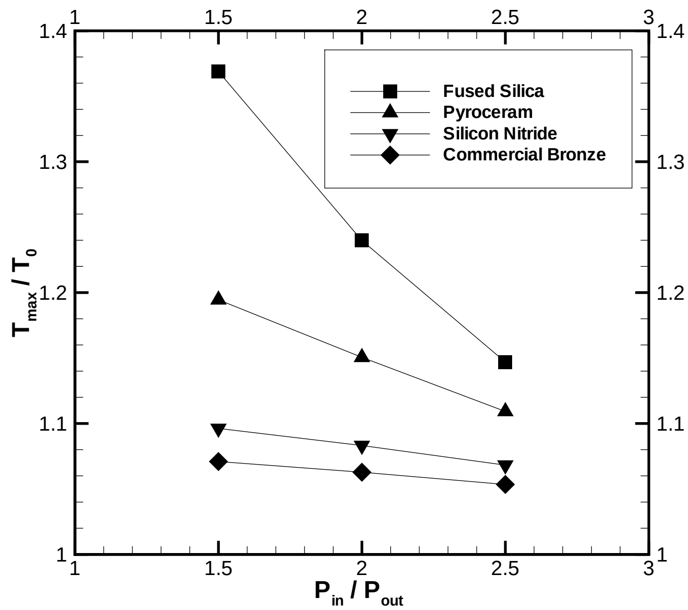

Figure 6.8: The maximum temperatures for the cases with P_{in}/P_{out} ranging from 1.5 to 2.5, $\bar{q}_w = 2 \times 10^{-4}$ and $H_s/H = 1.0$.

reduced heat flux from substrates to bulk fluid caused by the increased axial conduction in substrates. From Fig. 6.12, the non-monotonous feature of Nu along the channel exists not only in some cases with high-thermal-conductivity substrate materials but also in some cases with high substrate thickness and low-thermal-conductivity substrate materials. It is showed in Fig. 6.12 (d) that for the extreme case, where high substrate thickness and high thermal conductivity exist at the same time, Nu increases along the channel. Based on Fig. 6.10-6.12, the effects of substrate thickness is very similar to those of substrate thermal conductivity, which can be readily understood with the consideration of substrate axial thermal resistance. Therefore, the theory used to explain Fig. 6.3-6.6 can also explain Fig. 6.10-6.12.

6.3.3 Variable Properties of Substrate Materials

Since we are only interested in steady state solution, for substrates, only thermal conductivity can influence results. Based on Table 6.1, the variation of thermal conductivity with temperature are different for different substrate materials: for commercial bronze,

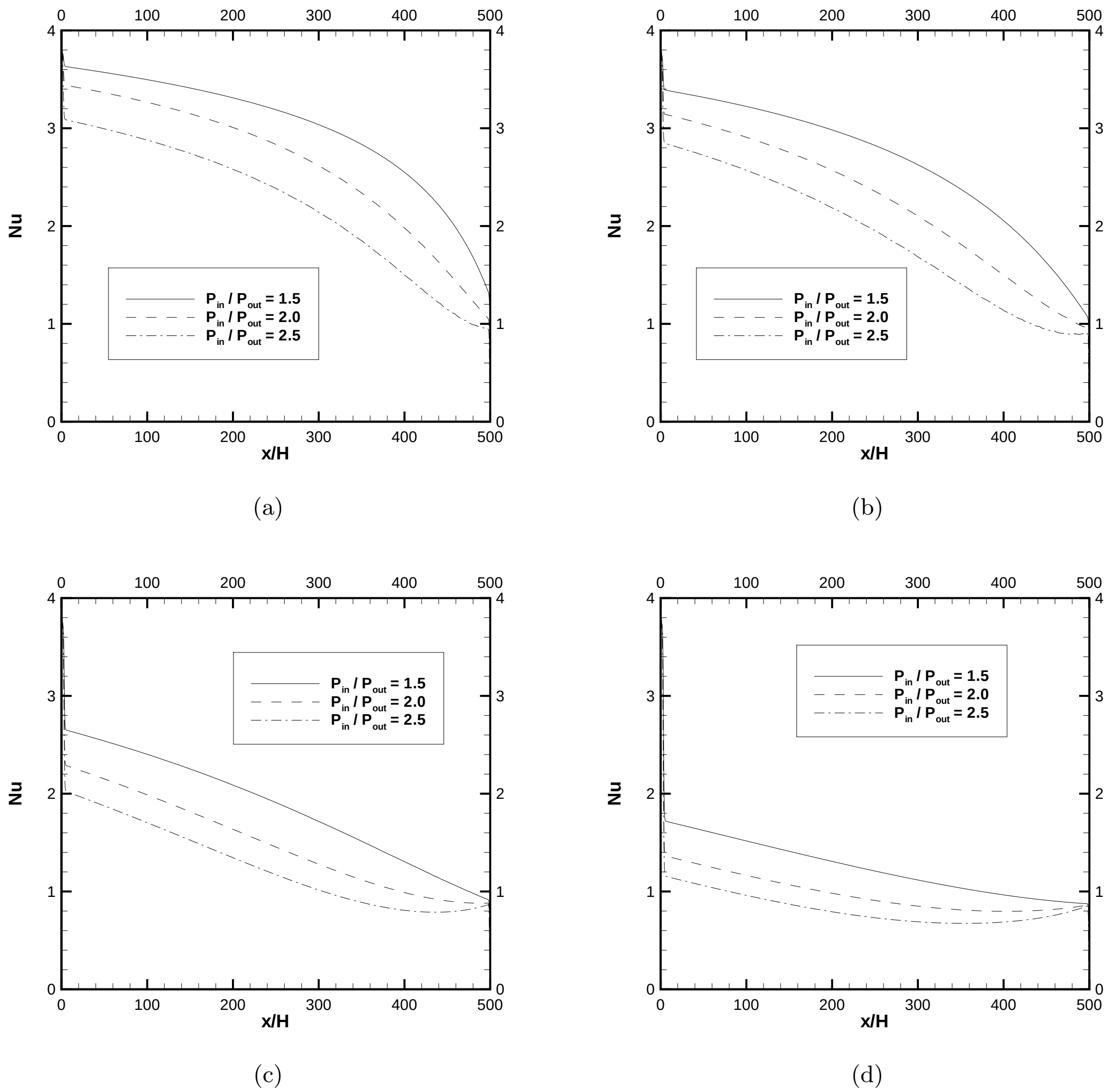

Figure 6.9: Local Nusselt number along the microchannel for the cases with P_{in}/P_{out} ranging from 1.5 to 2.5, $\bar{q}_w = 2 \times 10^{-4}$ and $H_s/H = 1.0$. The substrate material is (a) Fused silica; (b) Pyroceram; (c) Silicon Nitride; (d) Commercial Bronze.

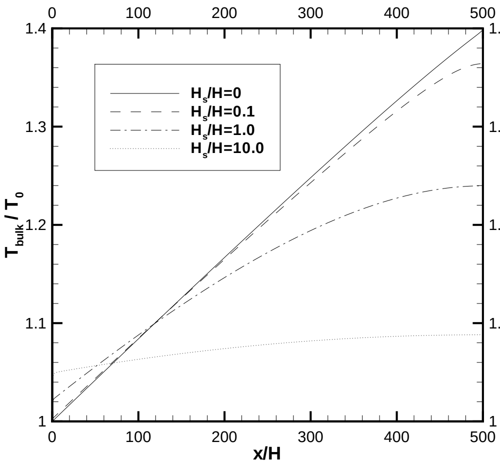

(a)

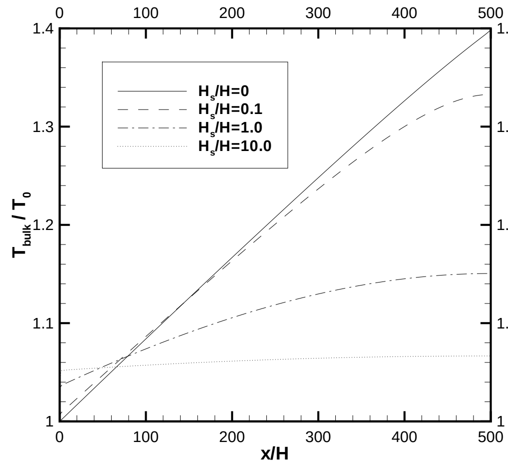

(b)

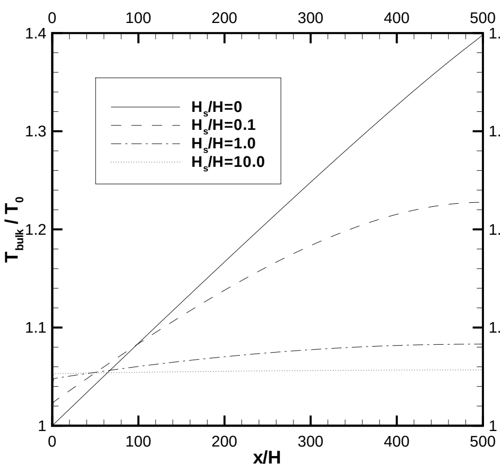

(c)

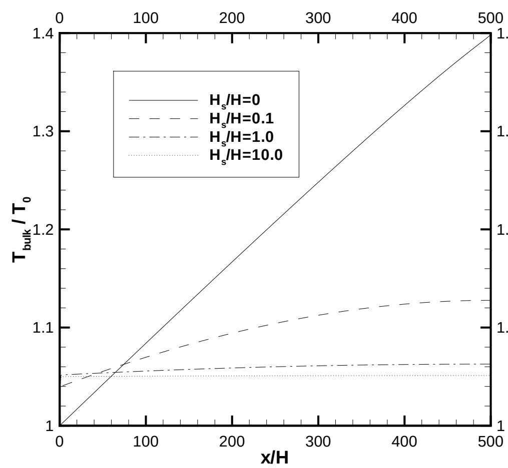

(d)

Figure 6.10: Bulk temperature profiles along the microchannel for the cases with $P_{in}/P_{out} = 2.0$ and $\bar{q}_w = 2 \times 10^{-4}$ but different H_s/H's. The substrate material is (a) Fused silica; (b) Pyroceram; (c) Silicon Nitride; (d) Commercial Bronze.

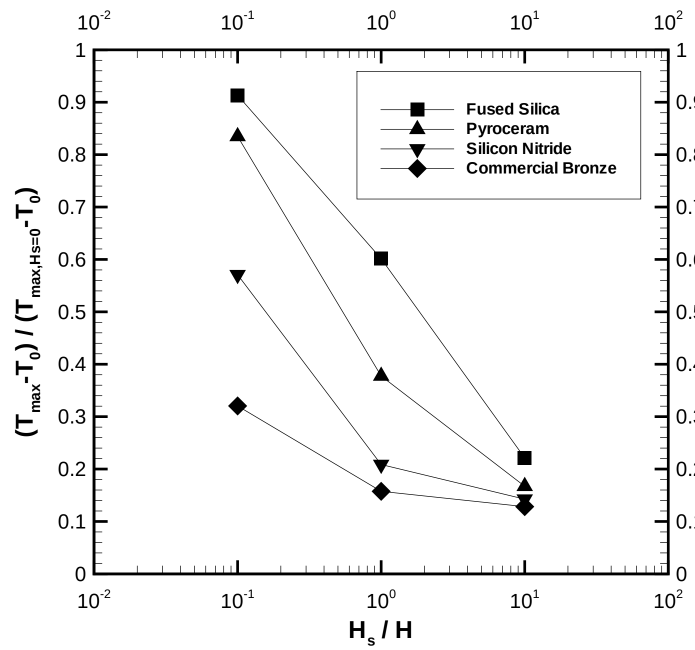

Figure 6.11: The maximum temperatures for the cases with $P_{in}/P_{out} = 2.0$ and $\bar{q}_w = 2 \times 10^{-4}$ but different H_s/H's.

thermal conductivity is almost constant within our interested temperature range; for silicon nitride and pyroceram, thermal conductivity decreases as temperature; for fused silica, thermal conductivity increases as temperature. As shown in section 6.3.1, the axial conduction within substrates could change bulk temperature profile and the maximum temperature dramatically. Fused silica and pyroceram, which represent opposite trends of thermal conductivity with temperature, are selected to study the influence of substrate variable properties. To measure the influence of variable properties, the maximum temperatures are compared between variable and constant property models in Fig. 6.13. Fig. 6.13 (a) shows the results for fused silica substrates with $\bar{q}_w$ ($q_{w,norm}$ in figure) ranging from 1×10^{-4} to 3×10^{-4}, $H_s/H = 1.0$ and $PR = P_{out}/P_{in} = 2.0$. Fig. 6.13 (a) shows that constant property model slightly overestimate the maximum temperatures. This is because of the increased axial conduction due to the increase of thermal conductivity of fused silica with temperature. Fig. 6.13 (b) presents the results for pyroceram substrates with $\bar{q}_w$ ranging from 1×10^{-4} to 3×10^{-4}, $H_s/H = 1.0$ and

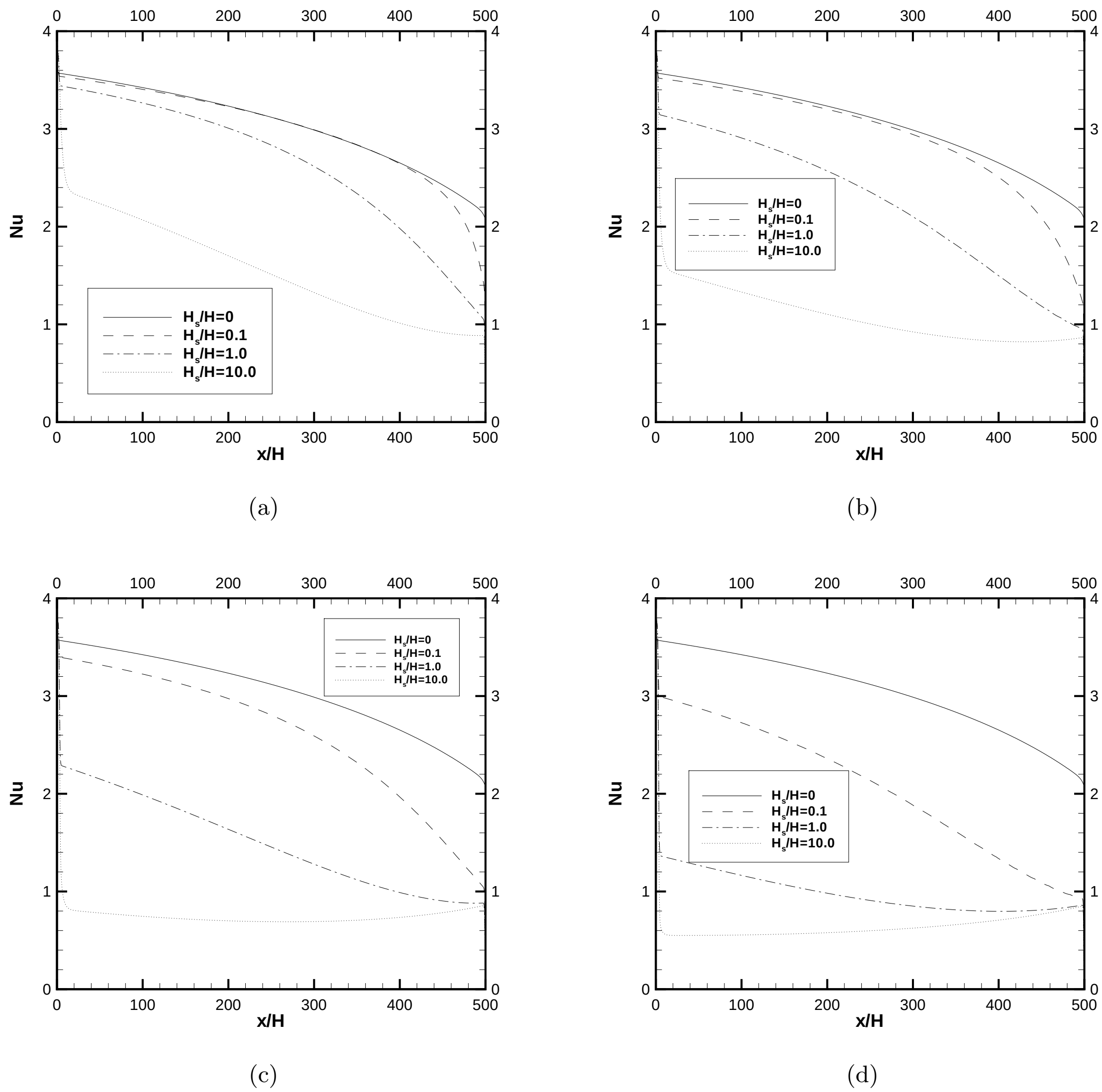

Figure 6.12: Nusselt number profiles along the microchannel for the cases with $P_{in}/P_{out} = 2.0$ and $\bar{q}_w = 2 \times 10^{-4}$ but different H_s/H's. The substrate material is (a) Fused silica; (b) Pyroceram; (c) Silicon Nitride; (d) Commercial Bronze.

$P_{out}/P_{in} = 2.0$. Fig. 6.13 (b) shows that constant property model slightly underestimate the maximum temperatures. This is because of the reduced axial conduction caused by the decrease of thermal conductivity of pyroceram with temperature. In general, for substrate materials, constant property model does not lead to significant deviation compared to variable property model.

6.4 Conclusions

Based on the results and analysis in section 6.3, several conclusions are made below for the conjugate heat transfer associated with microchannel pressure-driven nitrogen slip flow under uniform heat flux wall boundary condition:

- Axial conduction is far from negligible for substrates of finite thickness. Axial conduction leads to flatter bulk temperature profile along the channel, lower maximum temperature, and lower Nusselt number.
- The effects of substrate thickness on conjugate heat transfer is very similar to those of substrate thermal conductivity. That is, in terms of axial thermal resistance, the increase of substrate thickness has the same impact as that caused by the increase of substrate thermal conductivity.
- For the substrate materials, constant property model does not lead to significant deviation from variable property model.

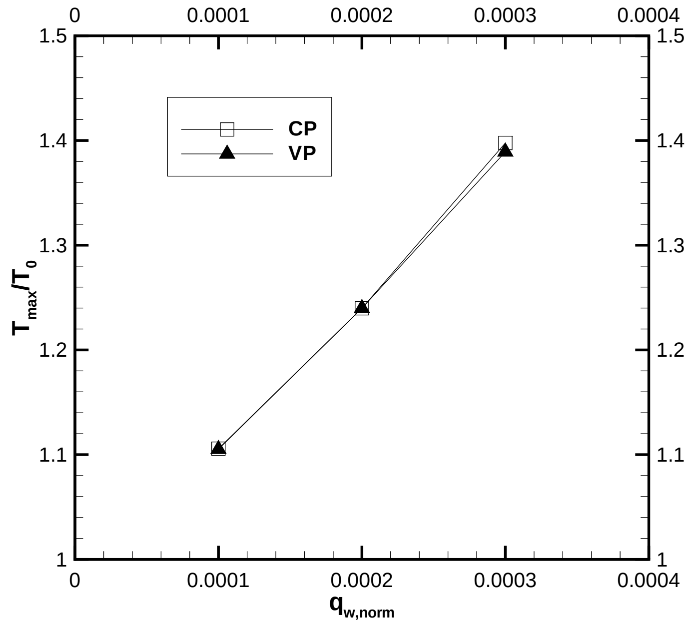

(a)

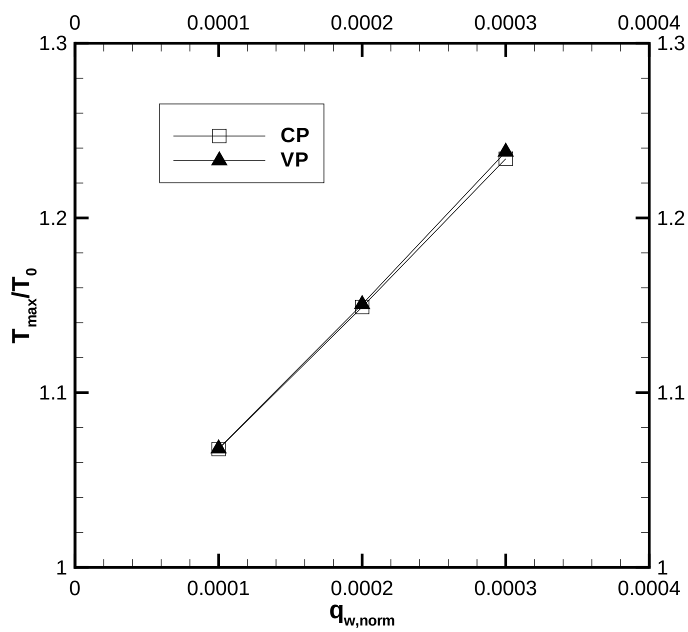

(b)

Figure 6.13: Comparison of the maximum temperatures between variable and constant property models for the cases with $\bar{q}_w$ ($q_{w,norm}$ in figure) ranging from 1×10^{-4} to 3×10^{-4}, $H_s/H = 1.0$ and $PR = P_{out}/P_{in} = 2.0$, where VP denotes variable property model and CP denotes constant property model. (a) Fused silica; (b) Pyroceram.

Chapter 7

Two Dimensional Unsteady Convection for Pressure-Driven Nitrogen Flow in Long Microchannels Under Uniform Heat Flux Wall Boundary Condition

7.1 Introduction

In Chapter 2-6, only steady state solution is obtained for thermal and fluid fields in microchannel flows. Very few studies are reported in the literature on unsteady microflows, especially for slip gas flows. A good review on transient microchannel gas flows can be found in the paper by Colin [43]. Norberg et al. [44] experimentally studied transient flows in microchannels with a mass spectrometric system, but for very short transients (in the order of 10s) and in molecular regime. Bestman et al. [45] considered the Rayleigh problem for slip flows. Arklic and Breuer [46] modeled an unsteady microflow induced by oscillating plates, where the governing equations only represented a balance between the unsteady and viscous forces. In this chapter, two kinds of unsteady convections will be studied for pressure-driven nitrogen slip flows in long microchannels under uniform heat flux wall boundary condition: the first kind is due to a sudden change in wall heat flux, while the second one is caused by inlet pressure jump. Channel #4 in Table 5.1 is chosen to study. The organization of this chapter is as follows: section 7.2 briefs the numerical model; section 7.3 presents the results with comments; finally, conclusions are given in section 7.4.

7.2 Numerical Model Description

The readers can refer to Chapter 2 for mathematical model and numerical procedure. In this chapter, unsteady nitrogen slip flows with uniform heat flux wall boundary condition are investigated. Variable properties, rarefaction (velocity slip, thermal creep and temperature jump), compressibility and viscous dissipation are all included. The employed computational method is based on the SIMPLER algorithm and has both a serial and a parallel version. Only the serial solver is used. The convergence criteria used to check whether steady state has been attained are of the form

$$\varepsilon = \max \left\{ \begin{array}{ll} \text{if } \xi^n \neq 0 & \frac{|\xi^{n+1}-\xi^n|}{|\xi^n|} \\ \text{if } \xi^n = 0 & |\xi^{n+1}| \end{array} \right\} \tag{7.1}$$

where ξ applies to streamwise velocity u as well as temperature T, and the superscripts denote the time step. The convergence criteria for internal iterations, within a single time step, take the same form, where ξ applies to streamwise velocity u, vertical velocity v, pressure p and temperature T, and the superscripts denote the internal iteration step. The internal iteration stops when ε falls below 1×10^{-5}. In this chapter, the channel to be studied is Channel #4 given in Fig. 2.1 and Table 5.1. The same grid size 201×29 (X×Y), as that used in chapter 5, is selected. The time step is chosen to be 10τ, where $\tau = H/a_0 = 1.416 \times 10^{-7} sec$ is the nondimensionalized time unit. The application of a smaller time step has no significant influence on the results. The initial conditions use the steady state results obtained in Chapter 5.

7.3 Results and Discussion

All the cases involved in this study use nitrogen as the working gas. In section 7.3.1, the results of the unsteady convection caused by the step change in wall heat flux are presented and analyzed. Then in section 7.3.2, the results of the unsteady convection due to the step change in inlet pressure are presented and analyzed. Finally, some comments on the characteristic response time are given in section 7.3.3.

7.3.1 Wall Heat Flux Jump

Two working conditions are selected to study the transient features of the unsteady convection due to the heat input jump at the wall. These two working conditions use the same inlet pressure, $P_{in}/P_{out} = 1.001$, but different wall heat fluxes. One working condition uses $\bar{q}_w = \frac{q_w H}{T_0 k_0} = 3 \times 10^{-4}$, while the other uses $\bar{q}_w = 6 \times 10^{-4}$. The steady state conditions of one case are used as the conditions of the initial moment at which wall heat flux jumps to the other working condition.

Fig. 7.1 presents the evolution of bulk temperature profile with time, where Fig. 7.1(a) is for the case with wall heat flux jumping from low to high (QLH) and Fig. 7.1(b) is for that from high to low (QHL). In Fig. 7.1 and the following figures in section 7.3.1, the evolution is merely plotted up to $t = 8 \times 10^4 \tau$ after which time the fluid and thermal fields approach very slowly to steady state. Fig. 7.2 shows the evolution of centerline velocity profile with time, where Fig. 7.2(a) is for case QLH and Fig. 7.2(b) is for QHL. The evolution of centerline pressure profile with time is shown in Fig. 7.3, where Fig. 7.3(a) is for case QLH and Fig. 7.3(b) is for QHL. From Fig. 7.1, it is found that the response time of thermal field increases from upstream to downstream. This is because the thermal filed of downstream region is not only affected by the heat flux from channel wall but also influenced by upstream region mainly through convection. However, this trend is not obvious in Fig. 7.2 and Fig. 7.3, both of which represent fluid field. The evolution of local Nusselt number profile, which is defined by,

$$Nu = \frac{q_w H}{k(T_w - T_{bulk})} \tag{7.2}$$

is plotted in Fig. 7.4, where Fig. 7.4(a) is for case QLH and Fig. 7.4(b) is for QHL. It is found that for case QLH, Nu increases initially due to wall heat flux rise and then decreases; while for case QHL, Nu first decreases due to wall heat flux drop and then increases. In addition, from Fig. 7.4, as also shown in Fig. 5.24, the steady-state values of Nu for the two working conditions do not differ much.

The thermal and fluid parameters at certain points are closely examined in Fig. 7.5-7.7. Specifically, three points on channel centerline are studied, including $x/H = 10$, 20, and 30. Based on Fig. 7.5-7.7, it is clear that thermal field responds faster in upstream region than in downstream region, while fluid field does not have such apparent trend. By comparing Fig. 7.5 (a) to (b), it is found that the thermal response time is slightly shorter for case QHL.

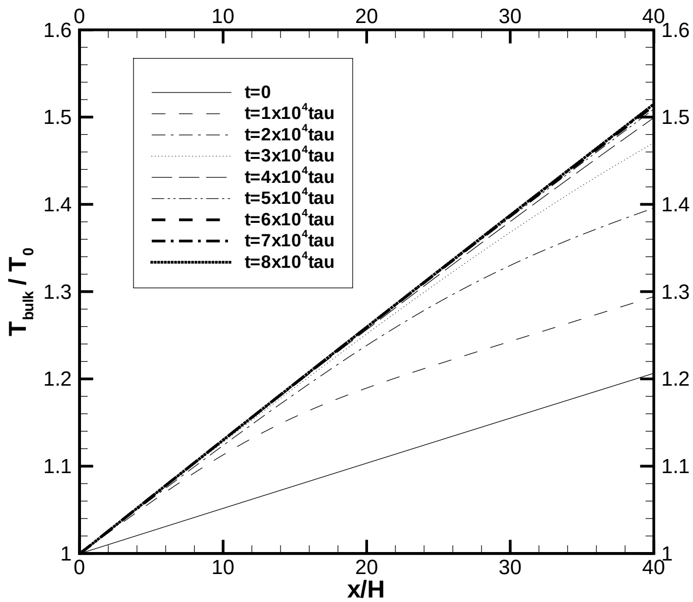

(a)

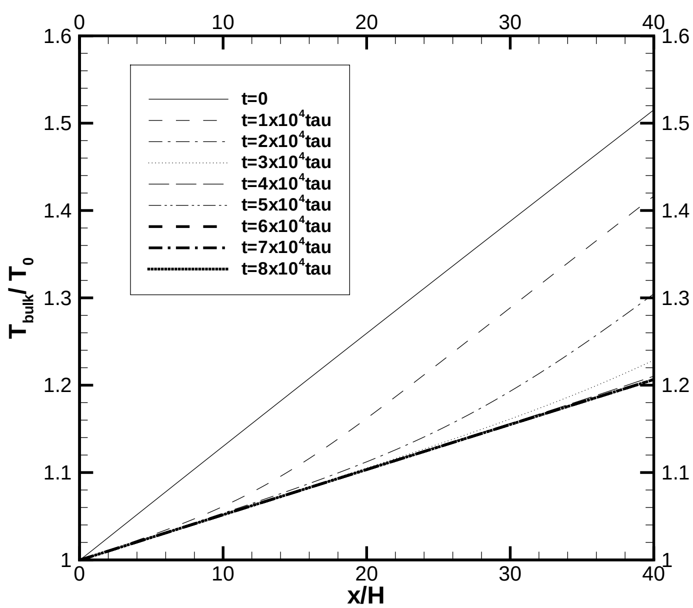

(b)

Figure 7.1: The evolution of bulk temperature profile with time for the unsteady convection due to step change in wall heat flux. (a) Wall heat flux step-changes from low to high; (b) Wall heat flux step-changes from high to low.

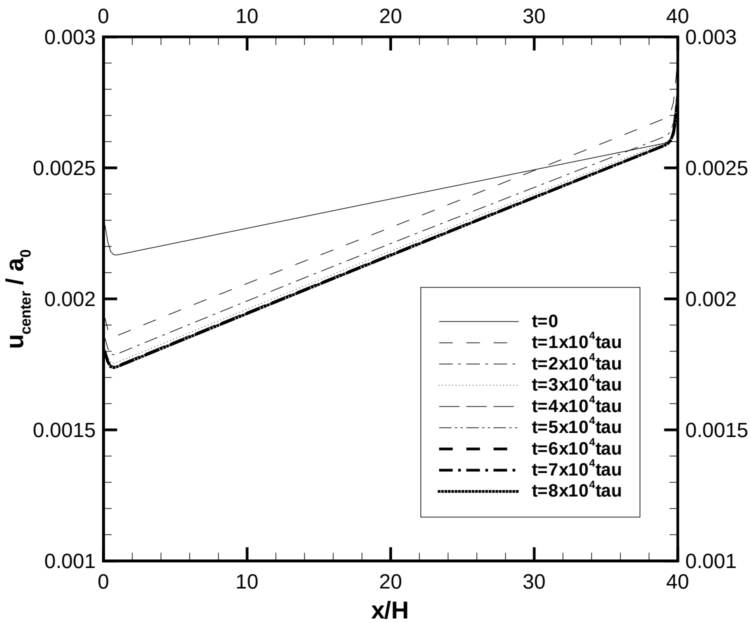

(a)

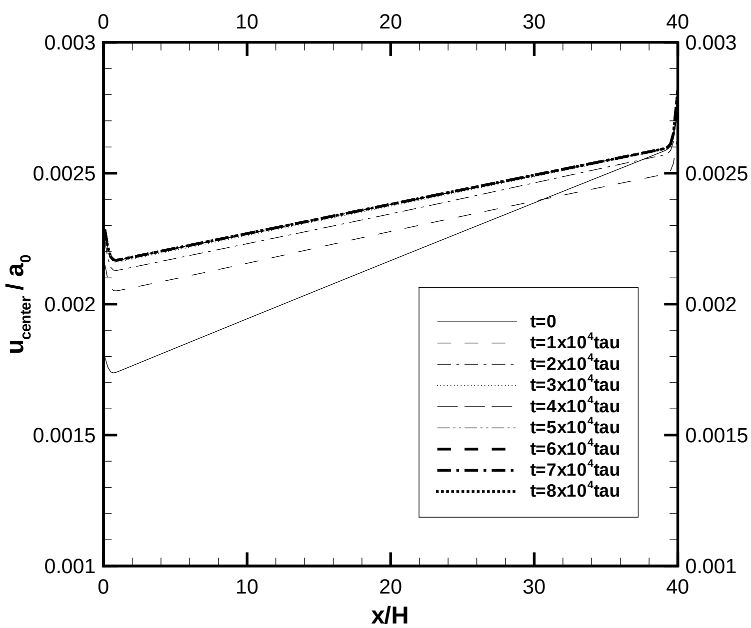

(b)

Figure 7.2: The evolution of centerline velocity profile with time for the unsteady convection due to step change in wall heat flux. (a) Wall heat flux step-changes from low to high; (b) Wall heat flux step-changes from high to low.

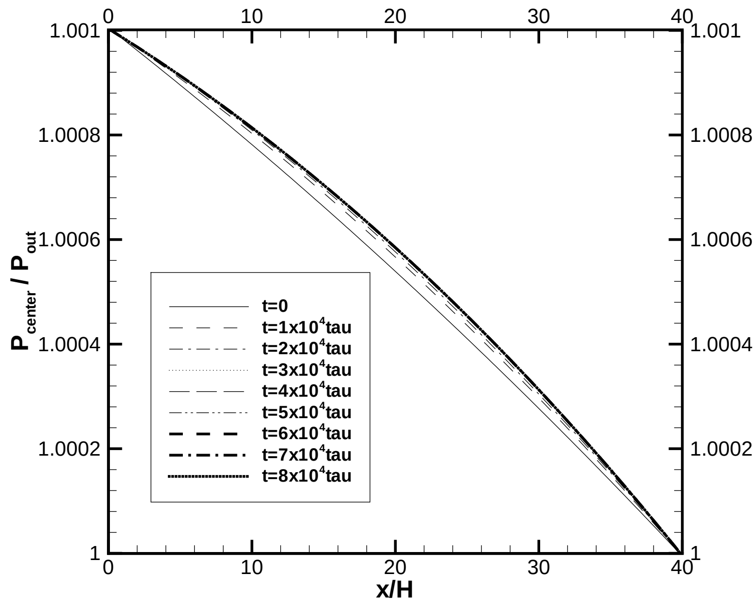

(a)

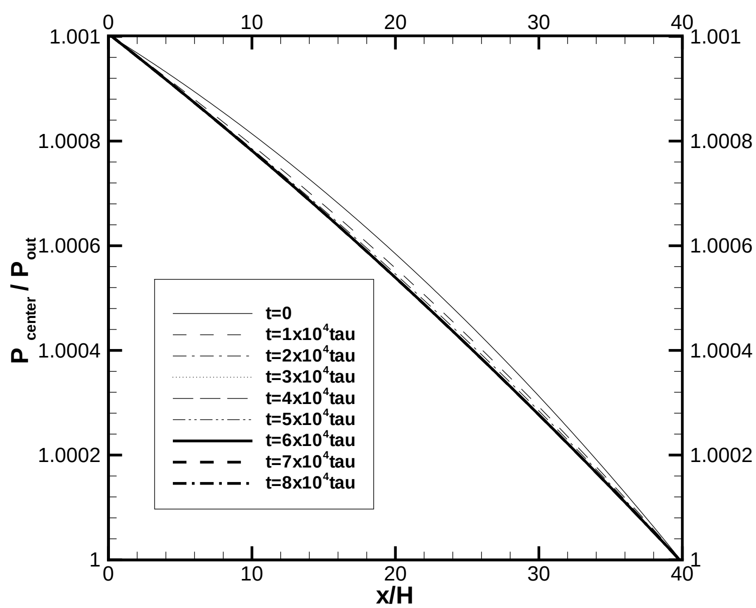

(b)

Figure 7.3: The evolution of centerline pressure profile with time for the unsteady convection due to step change in wall heat flux. (a) Wall heat flux step-changes from low to high; (b) Wall heat flux step-changes from high to low.

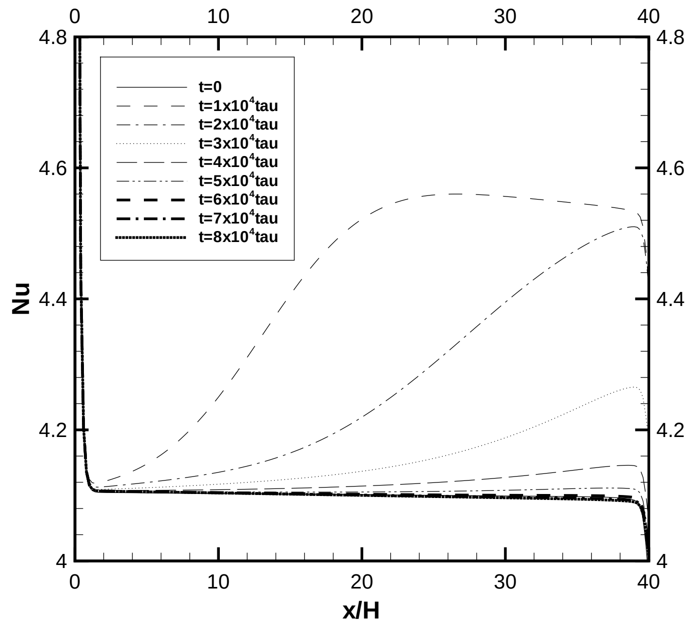

(a)

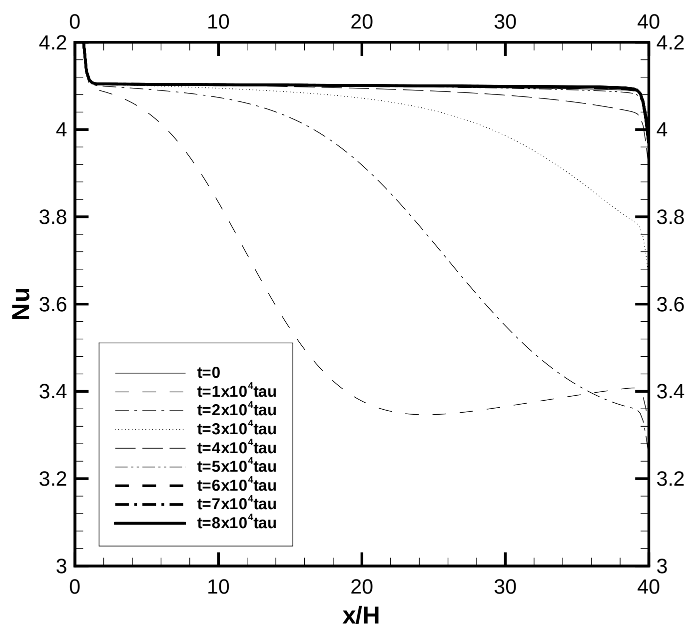

(b)

Figure 7.4: The evolution of local Nusselt number profile with time for the unsteady convection due to step change in wall heat flux. (a) Wall heat flux step-changes from low to high; (b) Wall heat flux step-changes from high to low.

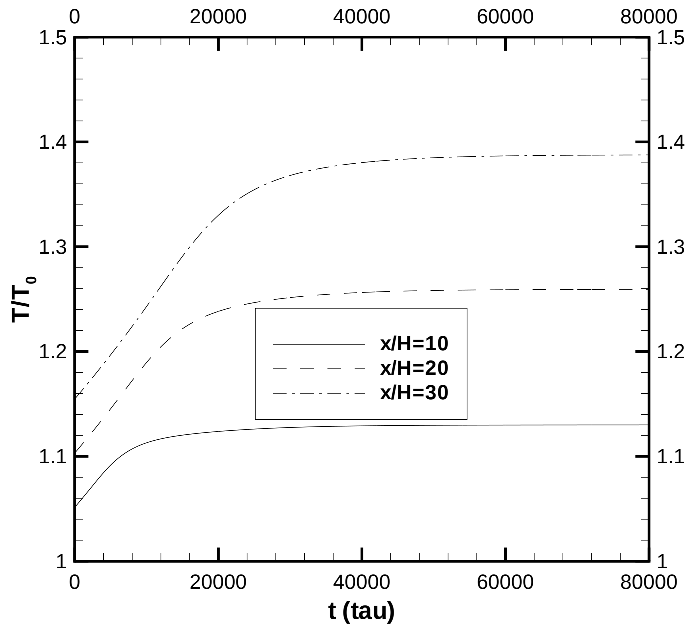

(a)

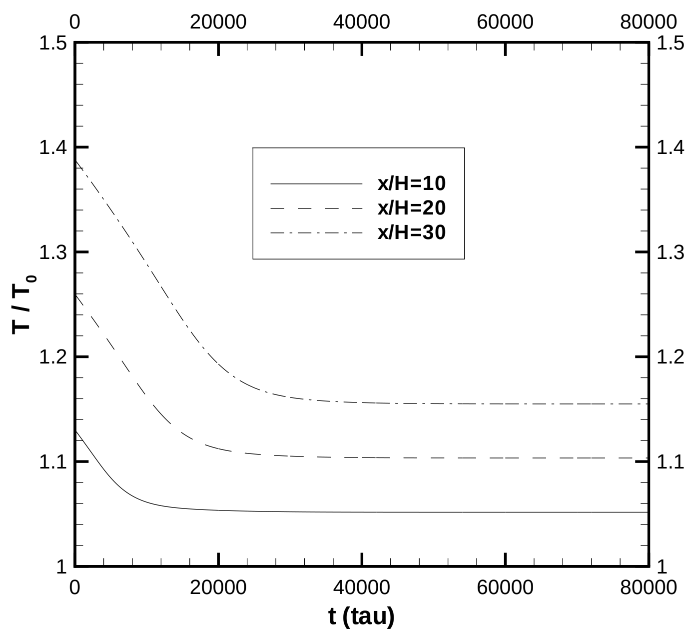

(b)

Figure 7.5: The evolution of temperature at some points on channel centerline with time for the unsteady convection due to step change in wall heat flux. (a) Wall heat flux step-changes from low to high; (b) Wall heat flux step-changes from high to low.

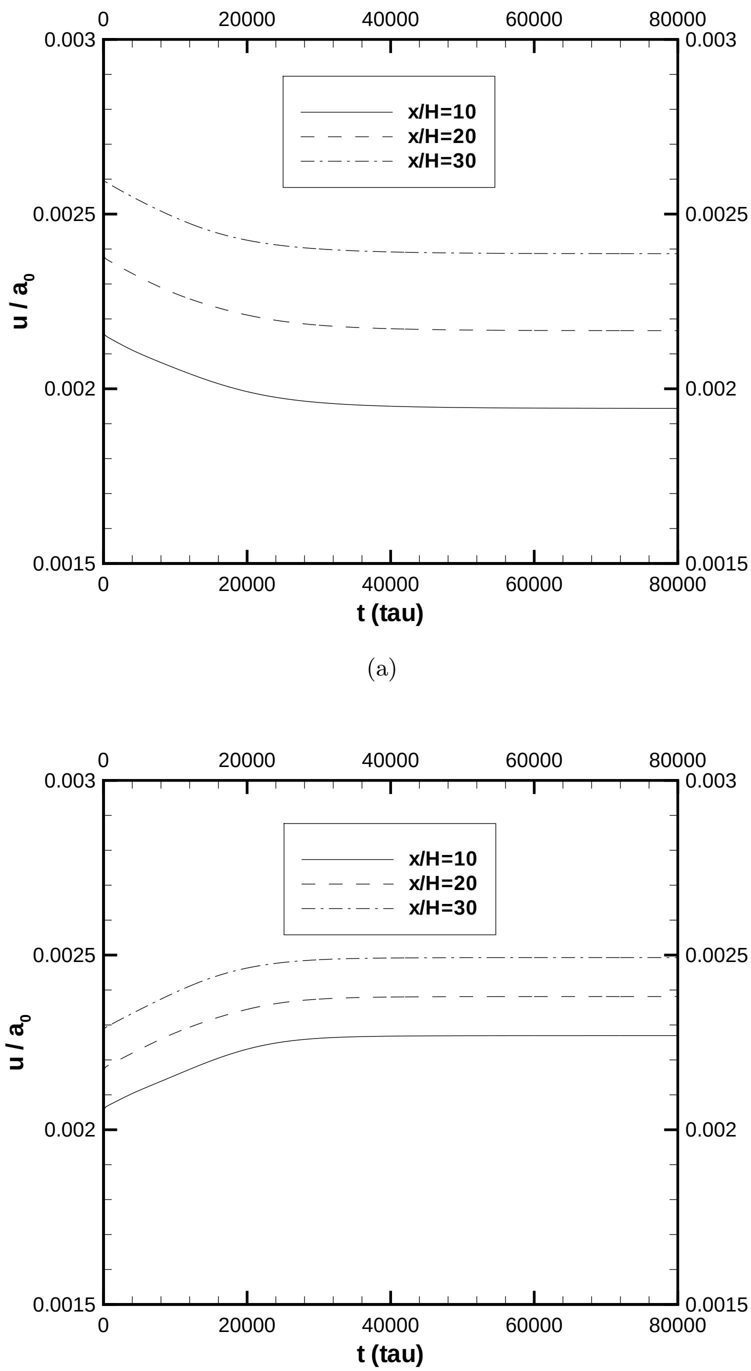

(a)

(b)

Figure 7.6: The evolution of streamwise velocity at some points on channel centerline with time for the unsteady convection due to step change in wall heat flux. (a) Wall heat flux step-changes from low to high; (b) Wall heat flux step-changes from high to low.

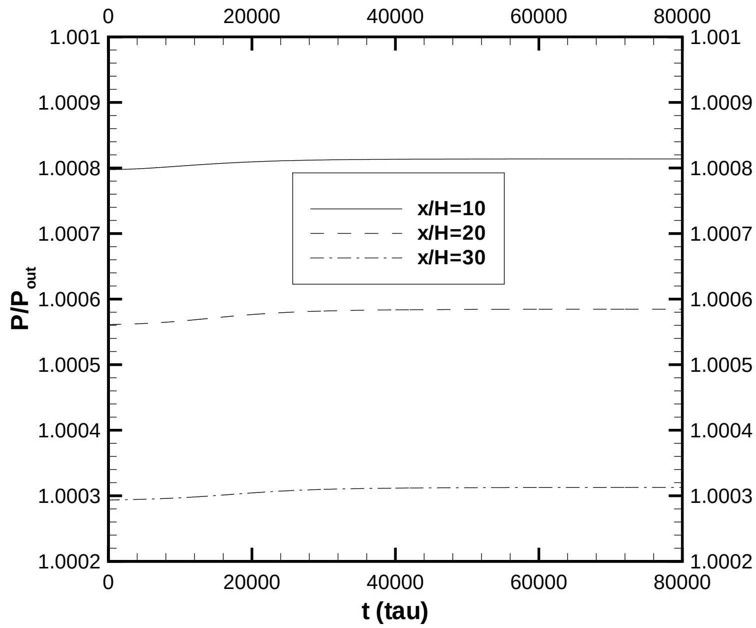

(a)

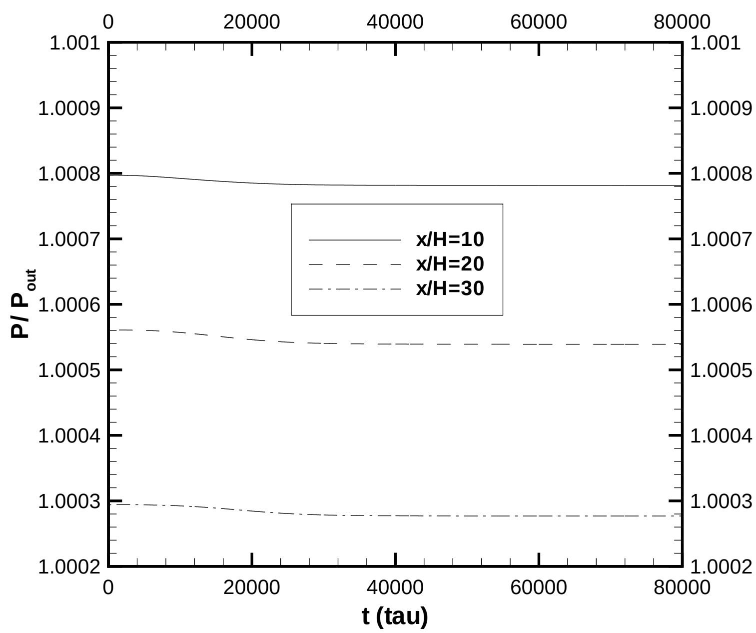

(b)

Figure 7.7: The evolution of pressure at some points on channel centerline with time for the unsteady convection due to step change in wall heat flux. (a) Wall heat flux step-changes from low to high; (b) Wall heat flux step-changes from high to low.

7.3.2 Inlet Pressure Jump

Two working conditions are selected to study the transient features of unsteady convection caused by inlet pressure jump. These two working conditions use the same wall heat flux, $\bar{q}_w = \frac{q_w H}{T_0 k_0} = 6 \times 10^{-4}$, but different inlet pressures. One working condition uses $P_{in}/P_{out} = 1.001$, while the other uses $P_{in}/P_{out} = 1.002$. The steady state condition of one working condition is used as the condition of the initial moment when inlet pressure jumps to the other working condition.

Fig. 7.8 presents the evolution of bulk temperature profile with time, where Fig. 7.8(a) is for the case with inlet pressure jumping from low to high (PLH) and Fig. 7.8(b) is for that from high to low (PHL). In Fig. 7.8 and the following figures of section 7.3.2, the evolution is merely plotted up to $t = 4 \times 10^4 \tau$ for case PLH and up to $t = 8 \times 10^4 \tau$ for case PHL. This is because after these time beings the fluid and thermal fields approaches very slowly to steady state. Fig. 7.9 shows the evolution of centerline velocity profile with time, where Fig. 7.9(a) is for case PLH and Fig. 7.9(b) is for PHL. The evolution of centerline pressure profile with time is shown in Fig. 7.10, where Fig. 7.10(a) is for case PLH and Fig. 7.10(b) is for PHL. From Fig. 7.8, similar to what was seen in section 7.3.1, it is found that the response time of thermal field increases from upstream to downstream. However, as found in section 7.3.1, this trend is not obvious in Fig. 7.9 and Fig. 7.10, both of which represent fluid field. The evolution of local Nusselt number profile with time is plotted in Fig. 7.11, where Fig. 7.11(a) is for case PLH and Fig. 7.11(b) is for PHL. It is found that for case PLH, Nu decreases initially due to the increase of temperature difference between the wall and bulk fluid, which is caused by the increase of mass flow rate, and then increases; while for case PHL, Nu first increases due to the decrease of temperature difference between the wall and bulk fluid, which is caused by the decrease of mass flow rate, and then decreases. In addition, from Fig. 7.11, also as shown in Fig. 5.27, the steady-state values of Nu for the two working conditions do not differ much.

The thermal and fluid parameters at certain points are presented in Fig. 7.12-7.14. Specifically, three points along channel centerline are studied, including $x/H = 10$, 20, and 30. Based on Fig. 7.12-7.14, it is clear that thermal field responds faster in upstream region than in downstream region, while fluid field does not have such apparent trend. By comparing Fig. 7.12 (a) to (b), it is found that the thermal response time is much shorter for case PLH.

7.3.3 Comments on Thermal Response Time

It is not surprising that the thermal response of downstream region is slower than that of upstream region under uniform wall heat input. What is worth noting is that the response times for the two cases, QLH and QHL, differ significantly; the response time for the two cases, PLH and PHL, are very different. Table 7.1 presents the characteristic thermal response time for the point at $x/H = 30$ on channel centerline. The characteristic thermal response time is measured by the formula:

$$\frac{T_{t_c} - T_2}{T_1 - T_2} = \frac{1}{e} \tag{7.3}$$

where T_1 is the temperature of initial steady state, T_2 is the temperature of final steady state, and T_{t_c} is temperature at the characteristic thermal response time t_c. From Table 7.1, it is clear that the characteristic thermal response time for case QHL is shorter than that of case QLH by about 10%, and the characteristic thermal response time for case PLH is much shorter than that of case PHL by more than 50%. If one carefully consider these four cases, it will not be difficult to regroup them by the rise or drop of flow temperature. Specifically, one group includes case QLH and PHL, where flow temperature rises after the sudden change of wall heat flux and inlet pressure, respectively; while the other group consists of case QHL and PLH, in which flow temperature drops after the sudden jump of wall heat flux and inlet pressure, respectively. The information from Fig. 5.22 and 5.26 tells us that pressure work is dominant over viscous dissipation, which means the fluid motion takes up energy from flow. It is then not hard to understand the difference on thermal response time mentioned above. The underlying mechanism is that the fluid motion promotes the drop of flow temperature and thus makes flow temperature rise more difficult than flow temperature drop. This can also explain why the characteristic thermal response time

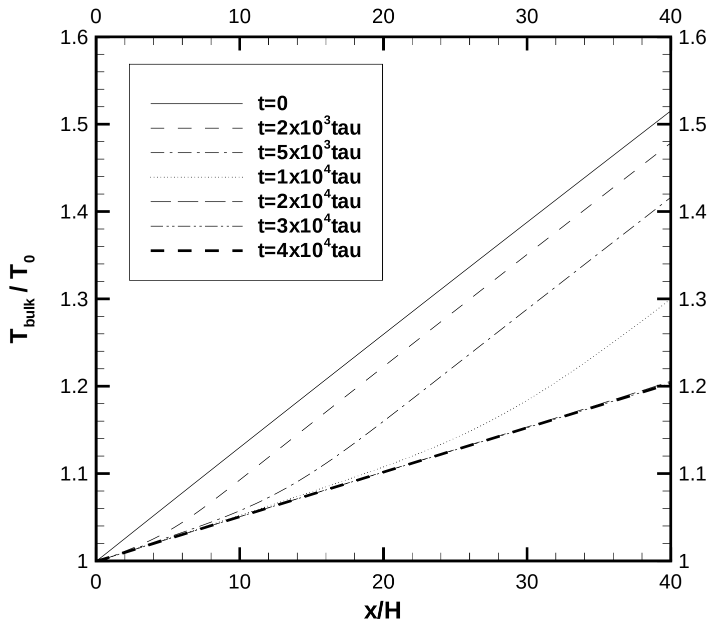

(a)

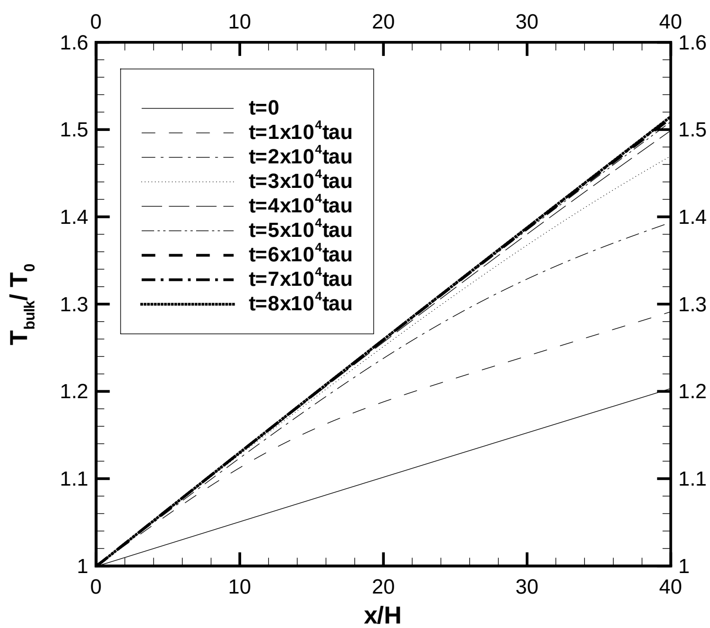

(b)

Figure 7.8: The evolution of bulk temperature profile with time for the unsteady convection due to step change in inlet pressure. (a) Inlet pressure step-changes from low to high; (b) Inlet pressure step-changes from high to low.

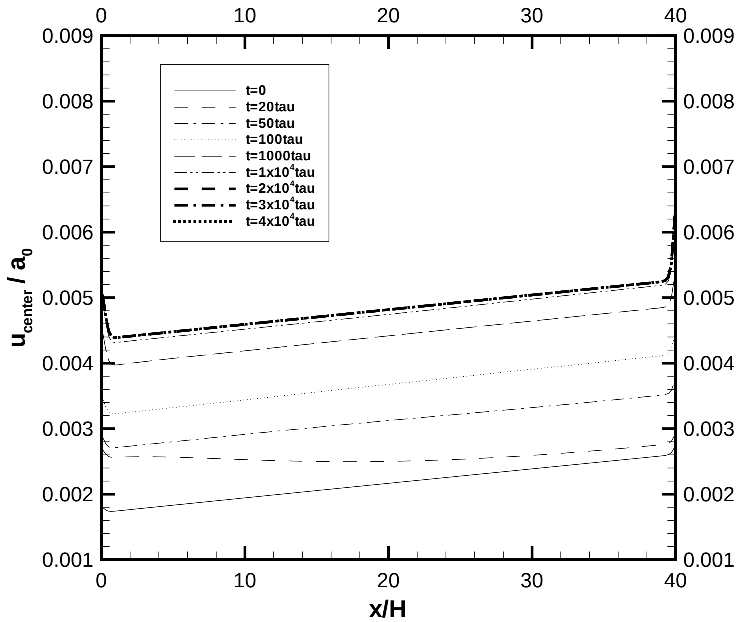

(a)

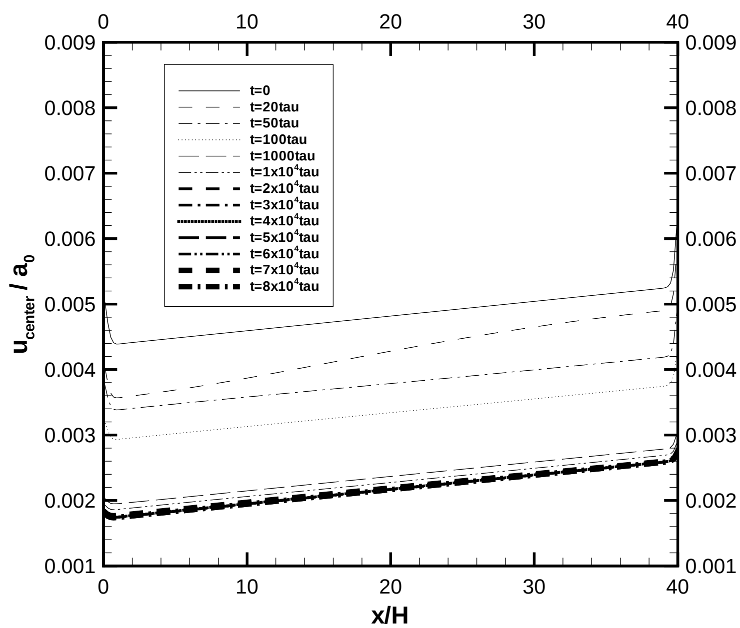

(b)

Figure 7.9: The evolution of centerline velocity profile with time for the unsteady convection due to step change in inlet pressure. (a) Inlet pressure step-changes from low to high; (b) Inlet pressure step-changes from high to low.

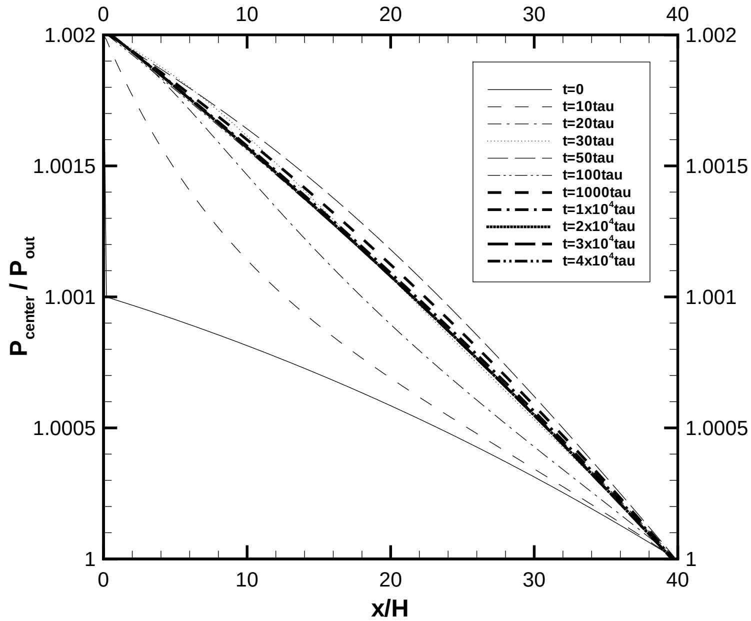

(a)

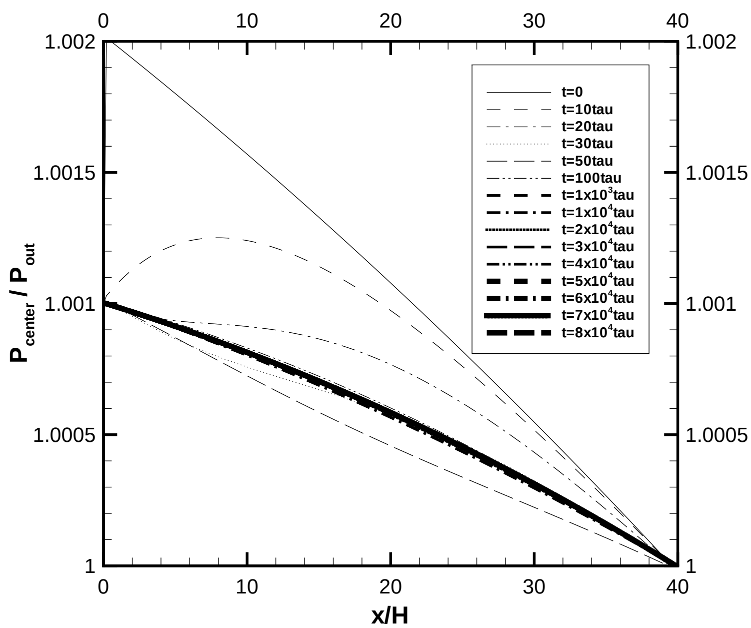

(b)

Figure 7.10: The evolution of centerline pressure profile with time for the unsteady convection due to step change in inlet pressure. (a) Inlet pressure step-changes from low to high; (b) Inlet pressure step-changes from high to low.

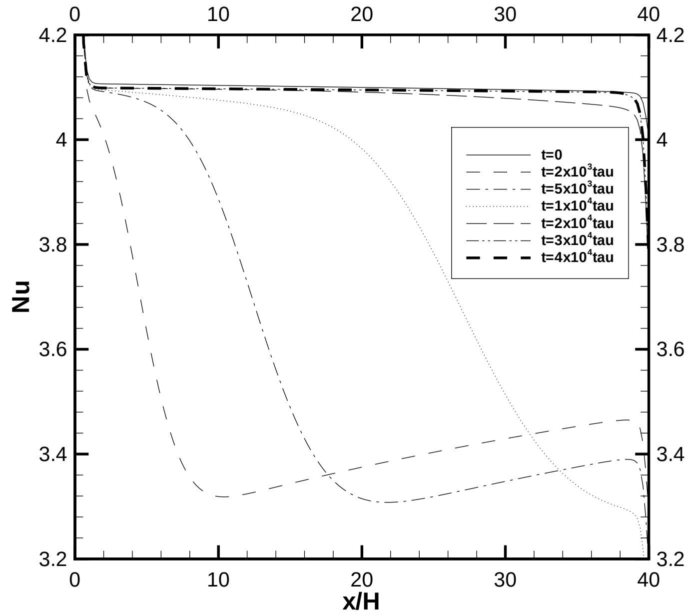

(a)

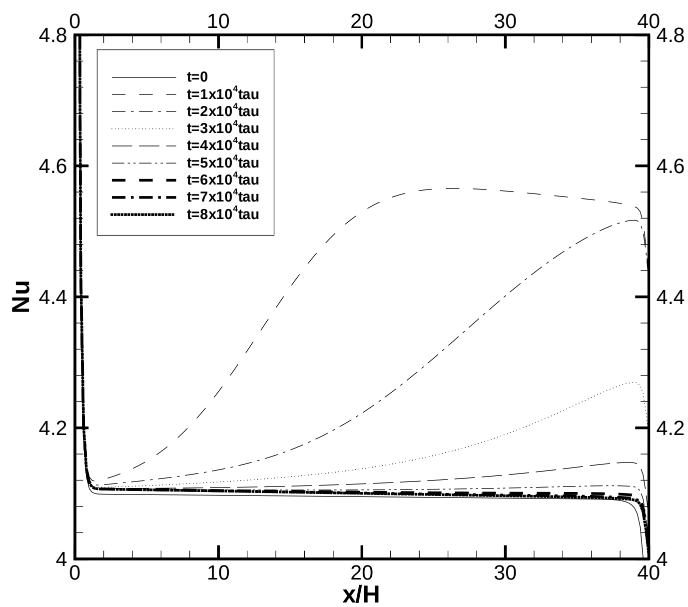

(b)

Figure 7.11: The evolution of local Nusselt number profile with time for the unsteady convection due to step change in inlet pressure. (a) Inlet pressure step-changes from low to high; (b) Inlet pressure step-changes from high to low.

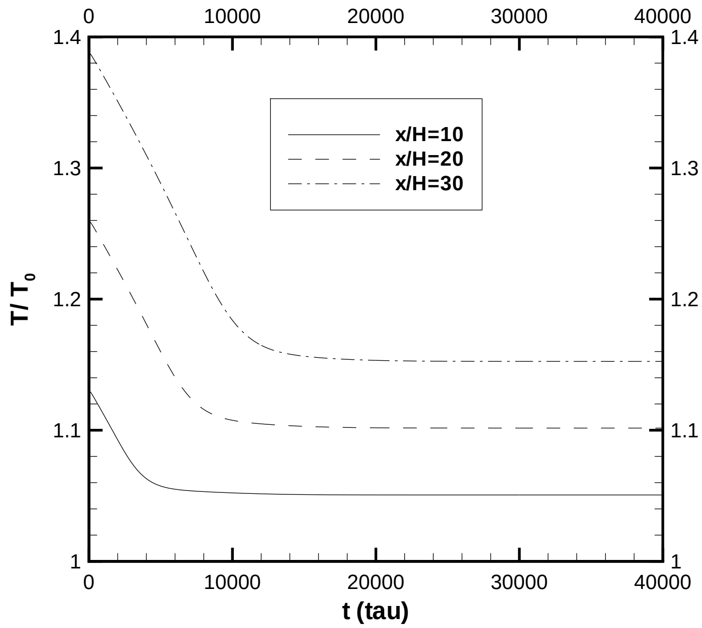

(a)

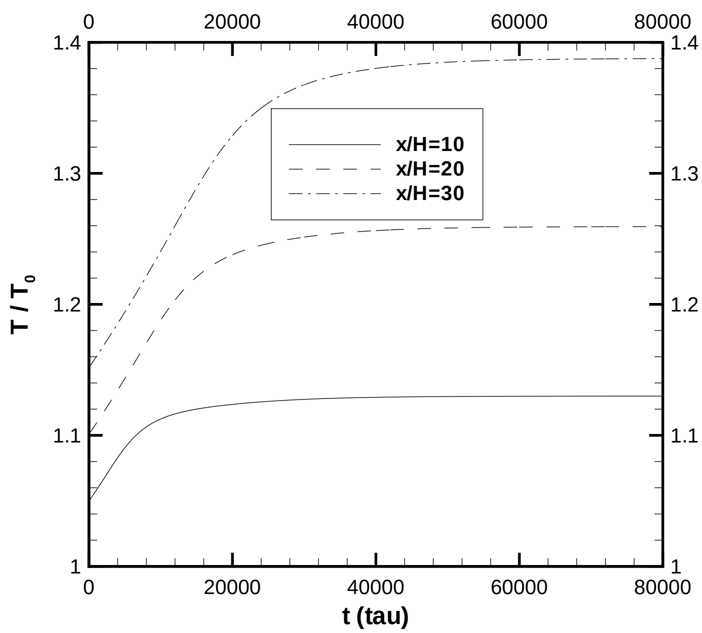

(b)

Figure 7.12: The evolution of temperature at some points on channel centerline with time for the unsteady convection due to step change in inlet pressure. (a) Inlet pressure step-changes from low to high; (b) Inlet pressure step-changes from high to low.

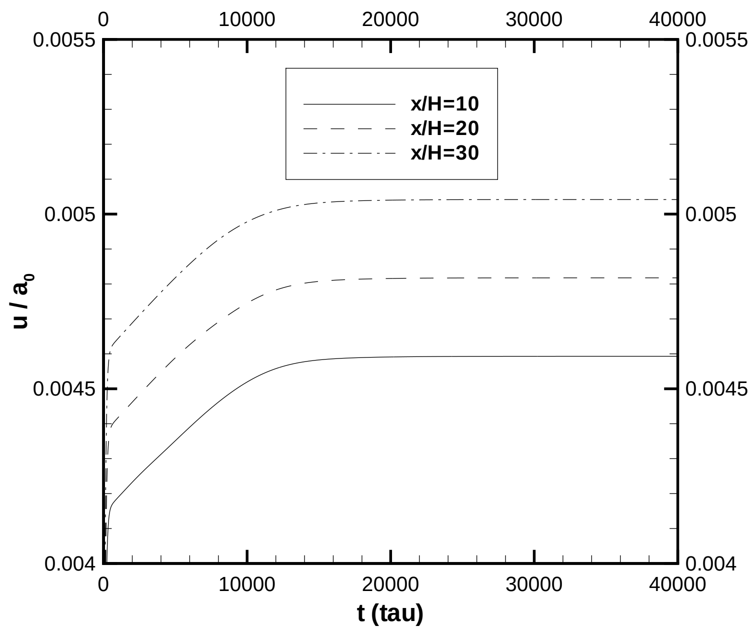

(a)

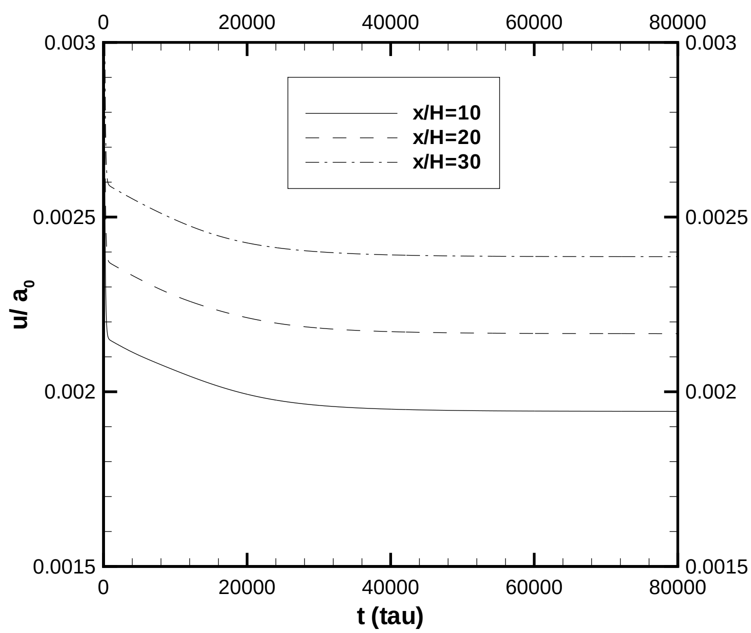

(b)

Figure 7.13: The evolution of streamwise velocity at some points on channel centerline with time for the unsteady convection due to step change in inlet pressure. (a) Inlet pressure step-changes from low to high; (b) Inlet pressure step-changes from high to low.

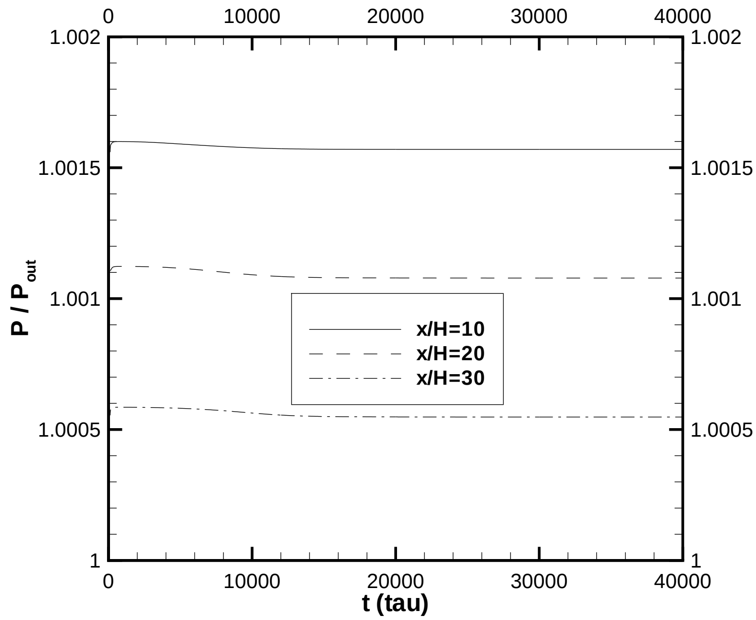

(a)

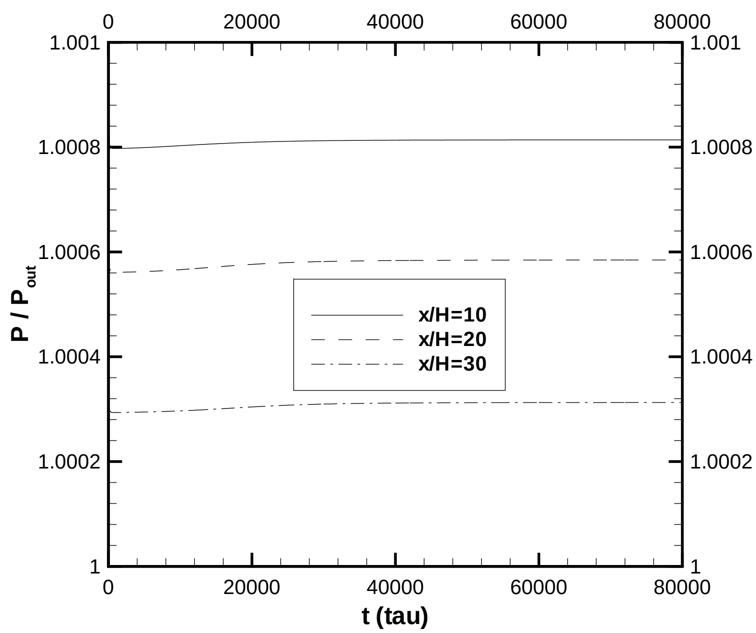

(b)

Figure 7.14: The evolution of pressure at some points on channel centerline with time for the unsteady convection due to step change in inlet pressure. (a) Inlet pressure step-changes from low to high; (b) Inlet pressure step-changes from high to low.

Table 7.1: Characteristic thermal response time for the point at $x/H = 30$ on microchannel centerline.

Case	QLH	QHL	PLH	PHL
Characteristic Response Time t_c (τ)	16270	14480	7190	16370

for case PLH is much shorter than that for case PHL. The reason is, in case PLH, the magnitude of the difference between pressure work and viscous dissipation increases a lot as the doubling of inlet/outlet pressure difference.

7.4 Conclusions

Based on the results presented in section 7.3, some conclusions are made below for the unsteady convection of pressure-driven nitrogen slip flow in long microchannels under uniform heat flux wall boundary condition:

- The characteristic thermal response time required for the case with sudden wall heat input drop could be 10% less than that needed for the case with sudden wall heat input rise.
- The characteristic thermal response time required for the case with sudden inlet pressure drop could be more than double of that needed for the case with sudden inlet pressure rise.
- The difference on the characteristic thermal response time mentioned right above is due to the energy taken up by pressure work.

Chapter 8

Conclusions and Future Work

8.1 Conclusions

The hydraulic and thermal characteristics of microchannel nitrogen slip flows are studied comprehensively within this dissertation. First, numerical modeling issues are solved by developing a parallel solver. For physical modeling issues, it is found that variable properties and the sources terms in energy equation need to be incorporated into the model with rarefaction. Two kinds of thermal wall boundary conditions, isothermal and uniform heat flux, are studied for the long microchannels with length-to-height ratios up to 2500:1. The source terms in energy equation are shown to greatly influence thermal and thus fluid fields. Specifically, the energy taken up by pressure work is dominant over the energy generation by viscous dissipation. Rarefaction effects are showed to be significant for both fluid and thermal fields. It is found that rarefaction influences Nusselt number in two ways: rarefaction reduces Nusselt number through the heat transfer between the wall and bulk fluid, while promotes Nusselt number by affecting the source terms in energy equation. Microchannels of larger dimensions, i.e., with characteristic dimensions between 10 and $100 \mu m$, are also studied. It is found that rarefaction is still far from negligible for these larger-dimension microchannels. Then conjugate heat transfer is studied. It is found that axial conduction gives a great impact for substrates of finite thickness. The effects of substrate thickness are found to be very similar to those of substrate thermal conductivity. For substrate materials, the results of constant property model are shown to be comparable to those of variable property model. Finally, unsteady convection is studied. It is found that the characteristic thermal response time required by the case with sudden wall heat input drop is less than that needed by the case with sudden wall heat input rise; the characteristic response time required by the case with sudden inlet pressure drop is much more than that needed by the case with sudden inlet pressure rise; the difference on the characteristic response time is due to the energy taken up by pressure work.

8.2 Future Work

The three dimensional problems are not done in this dissertation although the computer codes have already been developed. This is due to the demanding computational loads. Therefore, in the future, if the CPU speed allows, the three dimensional problems, including both steady state and transient problems, should be studied especially for long microchannels. Microchanel liquid flows are very interesting and a lot of work needs to be done when the characteristic dimension of the channel shrinks. Future work could also point to the two phase flows. Nowadays microscale boiling is a hot research area. People are trying to replace single-phase cooling with two-phase cooling, which is definitely more efficient and more effective for intense heat removal.

Bibliography

[1] Q. Wang. *Instability and Heat Transfer in Mixed Convection Flow in a Horizontal Duct with Application to Cooling of Electronic Systems.* PhD thesis, Rutgers University, New Brunswick, NJ, 2002.

[2] C.S. Chen, S.M. Lee, and J.D. Sheu. Numerical analysis of gas flow in microchannels. *Numerical Heat Transfer, Part A*, 33:749–762, 1998.

[3] D. B. Tuckermann and R.F. Pease. Optimized convective cooling using micromachined structure. *Journal of Electrochemical Society*, 129:C98, 1982.

[4] M. Gad el Hak. The fluid mechanics of microdevices - the freeman scholar lecture. *Journal of Fluids Engineering*, 121:5–33, 1999.

[5] J.C. Maxwell. On stresses on rarefied gases arising from inequalities of temperature. *Phyilosophical Transactions of the Royal Society of London*, 170:231–256, 1879.

[6] V. M. Smoluchowski. Ueber warmeleitung in verdunnten gasen. *Annalen der Physik und Chemie*, 64:101–130, 1898.

[7] S.B. Choi, R.F. Barron, and R.O. Warrington. Fluid flow and heat transfer in microtubes, micromechanical sensors. In *ASME DSC*, volume 19, pages 149–157, 1991.

[8] J. Pfahler, J Harley, H. Bau, and J. N. Zemel. Gas and liquid flow in small channels, micromechanical sensor. In *ASME DSC*, volume 32, pages 49–60, 1991.

[9] K.-C. Pong, C.-M. Ho, J. Liu, and Y.-C. Tai. Non-linear pressure distribution in uniform microchannels. In *Application of Microfabrication to Fluid Mechanics, ASME FED*, volume 196, pages 51–56, 1994.

[10] J.C. Harley, Y.H. Huang, H. Bau, and J.N. Zemel. Gas flow in microchannels. *Journal of Fluid Mechanics*, 284:257–274, 1995.

[11] D. Yu, R. Warrington, R. Barron, and T. Ameel. An experimental and theoretical investigation of fluid flow and heat transfer in microtubes. In *ASME/JSME Thermal Engineering Conference*, volume 1, pages 523–530, 1995.

[12] E.M. Sparrow and S.H. Lin. Laminar heat transfer in tubes under slip-flow conditions. *Journal of Heat Transfer*, 84:363–369, 1962.

[13] E.B. Arkilic, K.S. Breuer, and M.A. Schmidt. Gaseous slip flow in long microchannels. *Journal of Microelectromechanical Systems*, 6:167–178, 1997.

[14] J.-M. Li, B.-X. Wang, and X.-F. Peng. 'wall-adjacent' layeranalysis for developed-flow laminar heat transfer of gases in microchannels. *International Journal of Heat and Mass Transfer*, 43:839–847, 2000.

[15] S. Yu and T. A. Ameel. Slip-flow heat transfer in rectangular microchannels. *International Journal of Heat and Mass Transfer*, 44:4225–4234, 2001.

[16] S. Yu and T. A. Ameel. Slip flow convection in isoflux rectangular microchannels. *Journal of Heat Transfer*, 124:346–355, 2001.

[17] G. Tunc and Y. Bayazitoglu. Heat transfer in rectangular microchannels. *International Journal of Heat and Mass Transfer*, 45:765–773, 2002.

[18] C. Chen. Slip-flow heat transfer in a microchannel with viscous dissipation. *Heat Mass Transfer*, 42:853–860, 2006.

[19] H. Jeong and J. Jeong. Extended graetz problem including streamwise conduction and viscous dissipation in microchannel. *International Journal of Heat and Mass Transfer*, 49:2151–2157, 2006.

[20] A. Beskok, G. E. Karniadakis, and W. Trimmer. Rarefaction and compressibility effects in gas microflows. *Journal of Fluids Engineering*, 118:448–456, 1996.

[21] Z.Y. Guo and X.B. Wu. Compressibility effect on the gas flow and heat transfer in a microtube. *International Journal of Heat and Mass Transfer*, 40:3251–3254, 1997.

[22] S. Roy, R. Raju, H. F. Chuang, B. A. Cruden, and M. Meyyappan. Modeling gas flow through microchannels and nanopores. *Journal of Applied Physics*, 93:4870–4879, 2003.

[23] R. Raju and S. Roy. Hydrodynamic study of high-speed flow and heat transfer through a microchannel. *Journal of Thermophysics and Heat Transfer*, 19:106–113, 2005.

[24] E.B. Arkilic, K.S. Breuer, and M.A. Schmidt. Gaseous flow in microchannels. In *Application of Microfabrication to Fluid Mechanics, ASME FED*, volume 197, pages 57–66, 1994.

[25] D. I. Fotiadis, M. Boekholt, K. F. Jensen, and W. Richter. Flow and heat transfer in cvd reactors: Comparison of raman temperature measurements and finite element model predictions. *Journal of Crystal Growth*, 100:577–599, 1990.

[26] S. Thakur and W. Shyy. Some implementational issues of convection schemes for finite-volume formulations. *Numerical Heat Transfer, Part B*, 24:31–55, 1993.

[27] S. V. Patankar. *Numerical Heat Transfer and Fluid Flow*, pages 79–119. Hemisphere, Washington DC, 1980.

[28] N.D. Batlas and D.B. Spalding. Mimd phoenics: Porting a computational fluid dynamics application to a distributed memory mimd computer. In Dekker L et al. (eds)., editor, *Massively Parallel Processing Applications and Development*. Elsevier: Amsterdam, 1994.

[29] J.-T. Liu, X.-F. Peng, and W.-M. Yan. Numerical study of fluid flow and heat transfer in microchannel cooling passages. *International Journal of Heat and Mass Transfer*, 50:1855–1864, 2007.

[30] S.P.Mahulikar and H. Herwig. Physical effects in laminar microconvection due to variations in incompressible fluid properties. *Physics of Fluids*, 18:073601, 2006.

[31] C.P. Tso and S.P. Mahulikar. The use of the brinkman number for single phase forced convection heat transfer in microchannels. *International Journal of Heat and Mass Transfer*, 41:1759–1769, 1998.

[32] C.P. Tso and S.P. Mahulikar. The role of the brinkman number in analysing flow transitions in microchannels. *International Journal of Heat and Mass Transfer*, 42:1813–1833, 1999.

[33] C.P. Tso and S.P. Mahulikar. Experimental verification of the role of the brinkman number in microchannels using local parameters. *International Journal of Heat and Mass Transfer*, 43:1837–1849, 2000.

[34] B.X. Wang and X.F. Peng. Experimental investigation on liquid forced-convection heat transfer through microchannels. *International Journal of Heat and Mass Transfer*, 37:73–82, 1994.

[35] X.F. Peng and G.P. Peterson. The effect of thermofluid and geometrical parameters on convection of liquids through rectangular microchannels. *International Journal of Heat and Mass Transfer*, 38:755–758, 1995.

[36] X.F. Peng and G.P. Peterson. Convective heat transfer and flow friction for water flow in microchannel structures. *International Journal of Heat and Mass Transfer*, 39:2599–2608, 1996.

[37] Z.-Y. Guo and Z.-X. Li. Size effect on microscale single-phase flow and heat transfer. *International Journal of Heat and Mass Transfer*, 46:149–159, 2003.

[38] E.Y.K. Ng, C.P. Tso, Z.M. Wen, and K.F. Choo. Numerical simulation of flow and conjugate heat transfer in a microchannel for electronics cooling. *Journal of Electronics Manufacturing*, 9:141–153, 1999.

[39] A.G. Fedorov and R. Viskanta. Three-dimensional conjugate heat transfer in the

microchannel heat sink for electronic packaging. *International Journal of Heat and Mass Transfer*, 43:399–415, 2000.

[40] E.Y.K. Ng and S.T. Poh. Cfd analysis of double-layer microchannel conjugate parallel liquid flows with electronic double-layer effects. *Numerical Heat Transfer, Part A*, 140:735–749, 2001.

[41] G. Maranzana, I. Perry, and D. Maillet. Mini- and micro-channels: Influence of axial conduction in the walls. *International Journal of Heat and Mass Transfer*, 47:3993–4004, 2004.

[42] P. Sharath, C. Rao, M.M. Rahman, and H.M. Soliman. Numerical simulation of steady-state conjugate heat transfer in a circular microtube inside a rectangular substrate. *Numerical Heat Transfer, Part A*, 49:635–654, 2006.

[43] S. Colin. Rarefaction and compressibility effects on steady and transient gas flows in microchannels. *Microfluidics and Nanofluidics*, 1:268–279, 2005.

[44] I. Lundstorm P. Norberg, U. Ackelid and L.G. Peterson. On the transient gas flow through catalytically active micromachined channels. *Journal of Applied Physics*, 81:2094–2100, 1997.

[45] I.O. Ikonwa A.R. Bestman and I.U. Mbelegodu. Transient slip flow. *International Journal of Energy Research*, 19:275–277, 1995.

[46] E.B. Arkilic and K.S. Breuer. Gaseous flow in small channels. *AIAA*, 93-3270:1–7, 1993.

Vita

Zhanyu Sun

Education :

2008 Ph.D. in Mechanical and Aerospace Engineering, Rutgers University, New Brunswick, New Jersey, USA.

2004 M. Eng. in Mechanical Engineering, National University of Singapore, Singapore.

2001 B. Eng. in Mechanical Engineering, Zhejiang University, Hangzhou, China.

1997 Graduated from Qingdao #2 Middle School (Senior High School), Qingdao, China.

1994 Graduated from Qingdao #1 Middle School (Junior High School), Qingdao, China.

1991 Graduated from Qingdao Dingtao Road Primary School, Qingdao, China.

1985 Entered Qingdao Dingtao Road Primary School, Qingdao, China.

Work Experience :

2004-2008 Teaching Assistant, Department of Mechanical and Aerospace Engineering, Rutgers University, New Brunswick, New Jersey, USA.

2007 Instructor for "Engineering Mechanics - Statics" (Summer session B1 and H1), Department of Mechanical and Aerospace Engineering, Rutgers University, New Brunswick, New Jersey, USA.

2002-2004 Research Assistant, Department of Mechanical Engineering, National University of Singapore, Singapore.

Publication :

2006 Norman J. Zabusky, Zhanyu Sun, and Gaozhu Peng, Measures of Chaos and Equipartition in Integrable and Nonintegrable Lattices, *Chaos*, vol. 16, pp. 013130, 2006.

2005 Zhanyu Sun, Kian-Keong Poh, Lieng-Hsi Ling, G.S. Hong, and Chye-Heng Chew, Acoustic Diagnosis of Aortic Stenosis, *Journal of Heart Valve Disease*, vol.14, pp.186-194, 2005.